ENTANGLEMENT SPECTRUM OF GRAPHENE SYSTEMS

DISSERTATION ZUR ERLANGUNG DES DOKTORGRADES DER
NATURWISSENSCHAFTEN (DR. RER. NAT.) DER FAKULTÄT
PHYSIK
DER UNIVERSITÄT REGENSBURG

vorgelegt von Sonja Predin aus Belgrad, Serbien

im Jahr 2017

Promotionsgesuch eingereicht am: 28.10.2016

Die Arbeit wurde angeleitet von: Prof. Dr. John Schliemann

Prüfungsausschuss:
Vorsitz: Prof. Dr. Sergey Ganichev
Erstgutachter: Prof. Dr. John Schliemann
Zweitgutachter: Prof. Dr. Jaroslav Fabian
Weiterer Prüfer: Prof. Dr. Gunnar Bali
Ersatzprüfer: Prof. Dr. Ferdinand Evers

Termin Promotionskolloquium: 25.07.2017

ABSTRACT

In the present thesis, the properties of the entanglement spectra of the ground state of graphene bilayers Bernal-stacked is analytically investigated. In addition, the entanglement spectra of the ground state of the honeycomb lattice in the presence of superconductivity instabilities are analytically studied. We consider not only the eigenvalues of the reduced density matrix that form the entanglement spectrum, but also, its eigenstates. From these eigenstates, we construct topological quantities, such as the Berry phase and the Chern number, in order to investigate the topological properties of the entanglement spectrum.

In the first part of this thesis, we present an analytical study of the graphene bilayers, mainly focusing on the effects of the trigonal warping. When the term causing the trigonal warping is neglected, the entanglement Hamiltonian obtained by tracing out one layer shows a proportionality with the energetic Hamiltonian of the remaining monolayer graphene, in the limit of strongly coupled layers. We demonstrate that this proportionality leads to an agreement of the topological quantities of these Hamiltonians. Moreover, we demonstrate that the entanglement spectrum of graphene bilayers with a trigonal warping spectrum clearly differs in the geometric shape from the energy spectrum of the remaining monolayer graphene. However, there is an agreement of the topological quantities such as Berry phase contributions to Chern numbers.

In the second part of this thesis, we give a detailed study of graphene in the presence of superconductivity instabilities, mainly considering the s-wave and the chiral $d_{x^2-y^2} + id_{xy}$ state. We investigate the relationship between the entanglement and energy spectrum, making use of the concepts of the Chern number constructed from eigenstates of the entanglement Hamiltonian. We demonstrate that the entanglement and remaining subsystem Hamiltonians can have different topologies. These findings are illustrated by considering the entanglement Hamiltonian of the ground state of graphene with $d_{x^2-y^2} + id_{xy}$ superconductivity obtained by tracing out one spin direction.

Our investigations are based on closed analytical expressions for the full eigensystem in the entire Brillouin zone of bilayer graphene with a trigonally warped spectrum and graphene with superconductivity instabilities.

PUBLICATIONS

1. Sonja Predin, Entanglement spectrum of Heisenberg ladders in a time-dependent magnetic field, preprint (submitted to the EuroPhysics Letters), arxiv:1705.08675.
2. Sonja Predin, and John Schliemann, Entanglement spectra of superconductivity ground states on the honeycomb lattice, preprint (submitted to the European Physical Journal B), arxiv:1611.01039.
3. Sonja Predin, Paul Wenk, and John Schliemann, Trigonal Warping in Bilayer Graphene: Energy versus Entanglement Spectrum, Phys. Rev. B **93**, 115106, (2016).
4. M. V. Milovanović, and S. Predin, On the coexistence of antiferromagnetism and d + i d superconducting correlations in the graphene bilayer, Phys. Rev. B **86**, 195113,(2012).

ACKNOWLEDGMENTS

I would like to take this opportunity to thank a number people for their help and support.

- First of all, I would like to express my sincere gratitude to my supervisor, Prof. Dr. John Schliemann for accepting me as a Ph.D. student and giving me the opportunity to work in the exciting field of entanglement. He shared his deep understanding of physical problems with me without limiting my freedom to research and investigate problems I considered interesting. I also thank Prof. Dr. Schliemann for his strong support in scientific matters throughout my Ph.D. studies.
- I would like to thank my diploma thesis advisor Prof. Dr. Milica Milovanović for introducing me to the field of superconductivity instabilities in a honeycomb lattice and for her comments on a draft of article arXiv:1611.01039.
- I appreciate Dr. Paul Wenk for checking my analytical results of the entanglement spectrum of the ground state of graphene bilayers with a trigonal warping and for his discussions and comments.
- I would like to thank Lars Milz for his comments.
- For the pleasant working atmosphere, I would like to thank all the members of Prof. Dr. Milena Grifoni chair, especially our lunch group and my office mates.
- Financial support through the Deutsche Forschungsgemeinschaft via GRK1570 and SFB 631 is gratefully acknowledged.
- I warmly thank my parents Olivera and Saša, and my sister Nina for their endless love and support.

CONTENTS

LIST OF FIGURES

LIST OF TABLES

1

INTRODUCTION

Quantum entanglement is the counterintuitive prediction of quantum mechanics that has no analogous phenomenon in classical physics. The entanglement arises from nonlocal quantum correlations between two or more subsystems of the quantum system. The concept of entanglement was first introduced in 1935 by Einstein, Podolsky, and Rosen in Ref. [Einstein et al., 1935], while the term *entanglement* was first introduced by Schrödinger in Ref. [Schrödinger, 1935]. Two entangled quantum subsystems cannot be described separately. Thus, the wavefunction of the whole system cannot be written as a product of the wavefunctions of the entangled subsystems. A well-known example of an entangled state is the spin singlet state of two spin-1/2 particles $|\psi\rangle = \frac{1}{\sqrt{2}}\left(|\uparrow\rangle\,|\downarrow\rangle - |\downarrow\rangle\,|\uparrow\rangle\right)$. After an interaction in which the spin-singlet state is produced, these two particles are separated in different locations. If one measures the spin of one particle and gets the spin direction $|\uparrow\rangle$, then the spin of the second particle is projected on the state $|\downarrow\rangle$. Thus, the measurement of one particle changes the state of the other particle, although the particles are in different locations and cannot communicate with each other. This was a paradox for Einstein, Podolsky, and Rosen, (EPR paradox) since, according to special relativity, the *locality* condition assumes that nothing can travel faster than the speed of light. If we can predict with *certainty* the result of the measurement of a physical quantity then this quantity is an element of *physical reality.* Furthermore, they concluded that the description of the quantum mechanics of physical reality is not complete and proposed hidden local variables as a solution to this problem. This means that each particle possesses all the necessary information, and no information should be transmitted from one particle to another during the measurement. In 1965, John Bell showed that in local realism, the correlations between distant measurements satisfy inequalities. He mathematically proved that the quantum theory predicts a violation of these inequalities [Bell, 2004]. Bell-inequality violations have been experimentally demonstrated [Freedman and Clauser, 1972, Aspect et al., 1982, Garg and Mermin, 1987, Eberhard, 1993, Weihs et al., 1998, Rowe et al., 2001, Barrett et al., 2002, Matsukevich et al., 2008, Ansmann et al., 2009, Scheidl et al., 2010, Hensen et al., 2015]. Nowadays, we believe that quantum mechanics is an adequate theory for the description of the microscopic world and entanglement can successfully describe nonlocal and nonclassical correlations.

The idea of a quantum computer was proposed by Richard Feynman in 1982. [Feynman, 1982]. A quantum computer based on the quantum mechanical principles of superposition and entanglement would be much more powerful than a classical one. In recent decades, much effort has been invested in experimental and theoretical physics work to develop the quantum computer, owing to its possible uses, mainly in civil, business, and national security applications. The study of the many-body entangled state has recently become a very attractive topic, since it was realized that entanglement could be useful in quantum informatics. In particular, the quantum correlations between entangled states could be a useful resource for communications, because when a system is entangled, measurements of distant subsystems of the system can be much more correlated than is classically allowed [Bell, 2004]. It makes the quantum entanglement an attractive topic of research in various fields of physics.

The entanglement of the bipartite system of the subsystems A and B is defined in terms of the Schmidt decomposition of its ground state because the Hilbert space of the whole system is the direct product of two subsystems: $\mathcal{H} = \mathcal{H_A} \otimes \mathcal{H_B}$. The reduced density matrix for the subsystem A $\rho_A = \mathrm{tr}_B \rho$ is obtained by tracing out all degrees of freedom of the subsystem B. One of the most popular measurements of entanglement is entanglement entropy. The entanglement entropy of the subsystem A can be defined as:

$$S_A = -\mathrm{tr}_B \left(\rho_A \ln \rho_A \right). \tag{1.1}$$

Although first considered a source of quantum corrections to the entropy of black holes [Bombelli et al., 1986], entanglement entropy, in particular, the von Neumann entropy, evolved into a tool in the field of many-body systems. This heralded connections between seemingly unrelated research areas. In condensed matter, entanglement entropy serves, for example, as a geometrical interpretation for the boundary between local quantum many-body systems. This connection has its origin in the *area laws* [Eisert et al., 2010].

Another common tool for the measurement of entanglement is the entanglement spectrum. Since the reduced density matrix does not have negative eigenvalues, it can be always reformulated:

$$\rho_A = \frac{1}{Z} e^{-\mathcal{H}_\mathcal{A}} \tag{1.2}$$

with the entanglement Hamiltonian $\mathcal{H}_\mathcal{A}$ and the partition function $Z = \mathrm{tr}\left(e^{-\mathcal{H}_\mathcal{A}}\right)$. The spectrum of the entanglement Hamiltonian is the entanglement spectrum.

In condensed matter physics, the study of phases of matter and phase transitions is one of the most important topics of research. The phase and phase transitions are usually distinguished by Landau's theory of phase transitions, which involves the existence of a local order parameter, as opposed to the topological phases and topological phase transitions, which cannot be distinguished by a local order parameter. The latter phases possess so-called topological order [Wen, 1990, Wen, 1991]; their ground states might be degenerate and no local measurement can distinguish these degenerate ground states. The significance of the topological phase was underlined in 2016, when the Nobel Prize for Physics was awarded to David J. Thouless, F. Duncan M. Haldane, and J. Michael Kosterlitz "for theoretical discoveries of topological phase transitions and topological phases of matter". The entanglement spectrum is constructed from the ground state, which consists all the correlations that give rise to the various phases of matter. Li and Haldane found that one signature of the Fractional Quantum Hall effect, the low-energy excitations, can be related to the entanglement spectrum and suggested that the entanglement spectrum has information about a given phase [Li and Haldane, 2008]. Further, they concluded that the entanglement spectrum is beyond entanglement entropy, which extracts all the information from the reduced density matrix and proposed it as a new order parameter for distinguishing topological phases. Nowadays, the framework of the entanglement spectrum in condensed matter physics is very broad and is applied to many condensed matter systems, such as Quantum Hall liquids [Regnault et al., 2009, Zozulya et al., 2009, Läuchli et al., 2010, Thomale et al., 2010b, Ardonne and Regnault, 2011, Chandran et al., 2011, Hermanns et al., 2011, Schliemann, 2011, Sterdyniak et al., 2011, Thomale et al., 2011, Alba et al., 2012, Dubail et al., 2012, Liu et al., 2012, Rodriguez et al., 2012, Sterdyniak et al., 2012], topological insulators and superconductors [Fidkowski, 2010, Turner et al., 2010, Bray-Ali et al., 2009, Prodan et al., 2010, Borchmann et al., 2014, Kim, 2014], the fractional Chern insulator [Regnault and Bernevig, 2011], superfluids [Dubail and Read, 2011], spin systems [Nienhuis et al., 2009, Poilblanc, 2010, Pollmann and Moore, 2010, Pollmann et al., 2010, Yao and Qi, 2010, Cirac et al., 2011, Huang and Lin, 2011, Lou et al., 2011, Peschel and Chung, 2011, Thomale et al., 2010a, De Chiara et al., 2012, Läuchli and Schliemann, 2012, Lundgren et al., 2012, Schliemann and Läuchli, 2012, Tanaka et al., 2012, Chen and Fradkin, 2013, Lundgren et al., 2013, Lundgren et al., 2014, Lundgren, 2016, Predin, 2017], and Hofstadter bilayers [Schliemann, 2013]; for recent reviews, see Ref. [Regnault, 2015, Laflorencie, 2016]. As a result of this study, the entanglement spectrum possesses universal information about a phase and this is reflected to an exact equivalence between the low-lying entanglement spectrum and edge energy spectrum.

The statement that the entanglement spectrum has fundamental and universal information about the phase was criticized in Ref. [Chandran et al., 2014]. These authors have indicated that topological phase transitions can occur in the entanglement Hamiltonian, even though a physical system remains in the same state. The physical reason for this is that they have defined the entanglement Hamiltonian as $\mathcal{H}_{ent} = -\ln(\rho_{red})$, implying $Z \equiv 1$ at a finite effective temperature $T_E = 1/\beta \equiv 1$, with β is a inverse effective temperature. This makes the entanglement thermodynamics an important task of research.

A particular situation arises if the edge comprises the entire remaining subsystem. A typical observation in such a scenario is the proportionality between the entanglement spectrum, given by a traced out subsystem, and the energy spectrum of a remaining subsystem in the limit of strongly coupled subsystems. These findings are illustrated by many important examples, including spin systems [Poilblanc, 2010, Cirac et al., 2011, Peschel and Chung, 2011, Läuchli and Schliemann, 2012, Schliemann and Läuchli, 2012, Tanaka et al., 2012, Lundgren et al., 2013, Chen and Fradkin, 2013, Lundgren, 2016, Predin, 2017], and bilayer systems [Schliemann, 2011, Schliemann, 2013, Schliemann, 2014]. This proportionality can be illustrated by

$$\mathcal{H}_{ent} \sim \lambda \mathcal{H}_A / t \tag{1.3}$$

where λ is inverse proportional to the coupling between subsystems and t has the dimensions of energy. We note that the entanglement Hamiltonian entering the reduced density matrix Eq.(1.2) is only determined up to multiples of the unit operator, which has consequences regarding the thermodynamic relations between the entanglement entropy and the subsystem energy [Schliemann, 2011, Schliemann, 2013, Schliemann, 2014].

On the other hand, such a close relationship between the energy and entanglement Hamiltonian is not truly general, as shown in Ref. [Lundgren et al., 2012], in which a spin ladder of clearly nonidentical legs was studied.

In the present thesis, we will represent a detailed analytical study of the entanglement spectra of the ground states of graphene systems. This includes considerations of graphene bilayers focusing on trigonal warping [McCann and Koshino, 2013, Rozhkov et al., 2016], and as well graphene in the presence of superconducting instabilities [Black-Schaffer and Doniach, 2007]. Our analytical approach of the entanglement includes the eigenvalues of the reduced density matrix (giving rise to the entanglement spectrum) as well as its eigenvectors. From these eigenvectors, we construct topological quantities, the Berry phase, and the Chern number, in order to study the topological properties of the entanglement Hamiltonian. This ensures that our consideration of the relationship between the energy Hamiltonian of the remaining subsystem and the appropriately defined entanglement Hamiltonian includes not only their geometric but also topological properties. We will show that although the geometric shapes of the entanglement spectrum of an undoped graphene bilayer with a trigonal warped spectrum clearly differ from the energy spectrum of the remaining monolayer, their topological quantities such as the Berry phase contribution to the Chern number agree. On the other hand, the entanglement Hamiltonian of the $d_{x^2-y^2} + id_{xy}$ superconductivity ground states on the honeycomb lattice obtained by tracing out one spin direction and the Hamiltonian of the remaining subsystem have completely different topologies.

Our investigations are based on closed analytical expressions for the full eigensystem in the entire Brillouin zone of bilayer graphene with a trigonally warped spectrum and of graphene in the presence of superconductivity instabilities.

In the following, we give an outline of this thesis:

In Chapter 2, the lattice structure, tight-binding model, and energy description around the Dirac points in graphene are addressed. Here, we derive the tight-binding models assuming that electrons can hop to a nearest-neighbor atom. The topological properties of graphene are also discussed, and the density of states is presented.

Chapter 3 is dedicated to an investigation of Bernal-stacked graphene bilayers, taking into account only the nearest-neighbor hopping parameter and the hoping parameter between the atoms on opposite sites which are on top of each other. First, we recapitulate the tight-binding model of graphene bilayers. Here, as well as in Chapter 4, the entanglement Hamiltonian of the noninteracting free fermionic system on the graphene bilayers is analytically calculated as a single particle operator [Schliemann, 2013, Peschel, 2003, Cheong and Henley, 2004]. We demonstrate that upon tracing out one layer, in the limit of strongly coupled layers the proportionality between the entanglement Hamiltonian and the energy Hamiltonian of the graphene monolayer leads to the equivalence of their topological and thermodynamic properties. Here, the entanglement spectrum given by tracing out another two of four sublattices is considered, as well as the influence of the bias voltage or the mass term.

In Chapter 4, we analytically study the entanglement and the energy spectrum of the graphene bilayers in a Bernal stacking arrangement when the trigonal warping is present in the energy spectrum. In contrast with all earlier works, our analytical investigations of the energy spectrum of graphene bilayers with the presence of trigonal warping cover the entire Brillouin zone and avoid the Dirac cone approximation and the low-energy description of graphene bilayers. We demonstrate that the entanglement spectrum obtained by tracing out one layer vanishes between points where the energy spectrum possesses three additional Dirac cones caused by the trigonal warping. The topological properties of the entanglement spectrum of graphene bilayers, described by the Berry phase contributions to the Chern number, agree with the topological properties of graphene monolayers. Furthermore, we verify that the entanglement spectrum can be a discontinuous function of the momentum as a consequence of the fact that the trigonal warping produces discontinuities in the eigenvectors of the energetic Hamiltonian from which the entanglement spectrum is constructed. These discontinuities play an important role in both the geometric and topological properties of the entanglement spectrum. When an identical mass term in both layers or bias voltage is introduced, these discontinuities vanish and an entanglement gap opens. We also discuss the geometric and topological properties of the entanglement spectra given by tracing out other two of four sublattices. Technical details of the calculations of the full eigensystem of the Hamiltonian of graphene bilayers are presented in Appendix A. Furthermore, analytical derivations of the entanglement spectra are given in Appendix B.

Chapter 5 is dedicated to the entanglement spectra resulting from the superconductivity ground states on the honeycomb lattice tracing out one spin direction, mainly focusing on the s-wave and $d_{x^2-y^2} + id_{xy}$ -wave superconductivity states. Here, in order to analytically study the entanglement spectrum, we modify the method for analytical calculations of a free fermionic system to a system with superconductivity instabilities. We demonstrate that the topology of the entanglement Hamiltonian can differ from that of the subsystem Hamiltonian. In particular, the topological properties of the entanglement Hamiltonian of the chiral $d_{x^2-y^2} + id_{xy}$ superconductivity state obtained by tracing out one spin direction clearly differ from those of the time-reversal-invariant Hamiltonian of noninteracting fermions on the honeycomb lattice. Some technical details on the analytical derivation of the full eigenstates of the noninteracting fermionic system on the honeycomb lattice in the presence of superconductivity instabilities, as well as the correlation matrix calculations, are presented in Appendices C and D.

2

GRAPHENE: NEW PHYSICS IN TWO-DIMENSION

Graphene is an allotrope of carbon, a nonmetal that is a cornerstone of all organic compounds and thus of life on Earth. Since graphene is one atom thick, it can be considered as a two-dimensional object. Graphite, a three-dimensional crystal, is built of layers of graphene bonding via weak van der Walls bonds and is a well-known material since the 16th century, used in the cores of pencils. Graphene can be wrapped up as zero-dimensional fullerenes and rolled out as one-dimensional carbon nanotubes. The first molecules of fullerenes were fabricated in 1985 by Richard Smalley, Robert Curl, James Heath, Sean O'Brien, and Harold Kroto, while carbon nanotubes were discovered in 1991 by Sumio Iijima. A theoretical description of the band structure of graphene was written down by Wallace in 1947 as an important step in the research of graphite [Wallace, 1947]. Notwithstanding, it was believed that graphene could not exist as a free and stable two-dimensional crystal. Pierls and Landau indicated that two-dimensional crystals are thermodynamically unstable and cannot exist [Peirls, 1934, Landau and Lifshitz, 1980]. Mermin and Wagner amplified their contention, and it was illustrated with many experiments [Mermin and Wagner, 1966, Mermin, 1968]. Meanwhile, it was noticed that two-dimensional crystal structures can be stabilized by three-dimensional structures. Geim and Novoselov developed the method for isolation graphene by using Scotch tape in 2004 [Novoselov et al., 2004]. They were rewarded by the Nobel prize for this simple, groundbreaking, and inspiring discovery in 2010.

Since it was isolated, it has been one of the most intensively studied materials. Graphene is a light, strong, flexible, and conductive two-dimensional material with remarkable optical and electrical properties. This extraordinary combination of properties makes graphene a promising material for a new generation of devices, such as transistors, sensors, solar cells, and smartphones. Apart from the huge interest in investigations of graphene due to its potential applications in various devices, there is an enormous interest in fundamental research. The low-energy excitations in graphene are massless Dirac fermions, which were believed to be realizable in accelerators. The half-integer Quantum Hall effect and Berry's phase of π are consequences of the existence of the massless Dirac fermions in graphene [Zhang et al., 2005]. The existence of massless Dirac fermions enables measurements of high-energy phenomena, such as the Klein paradox [Katsnelson et al., 2006] and Zitterbewegung [Rusin and Zawadzki, 2008]. Thus, graphene has become a noteworthy bridge between condensed matter and high-energy physics, as quantum entanglement is a bridge between condensed matter physics and quantum informatics.

The electronic structure of graphene rapidly changes with the number of layers and ten layers can already be considered as graphite. Strictly speaking, only graphene and its bilayer have a simple electronic structure: both are either zero-gap semiconductors or zero-overlap semimetals. Furthermore, graphene possesses massless chiral quasiparticles as opposed to the massive ones in its bilayers. In the case of multilayer graphene, which consists of three to ten layers, the valence and conduction bands overlap and there are a few kinds of charge carriers. Monolayer, bilayer, and multilayer graphene can be realized as three different structures.

Carbon belongs to group IV of the periodic system. One carbon atom contains six electrons with the electronic structure $1s_2 2s_2 2p_2$. Two atoms are in the inner shell $1s$ and are more or less inert, while four valence electrons are described by $2s$, $2p_x$, $2p_y$ and $2p_z$, since one electron from the $2s$ orbital excites to the $2p_z$ orbital, in order to build covalent bonds. Three valence electrons in $2s$, $2p_x$ and $2p_y$ hybridize in planar sp^2 bonds, σ bonds. The three sp^2 orbitals lie in the x-y plane with an angle $120°$ between them. σ bonds are the strongest type of covalent bonds, because of the direct overlap between the orbitals. These bonds are responsible for the robustness of the honeycomb lattice of graphene [Castro Neto et al., 2009]. The remaining delocalized $2p_z$ orbitals are perpendicular to the plane. They are responsible for forming half-filled π-bonds by covalent bonding. The π electrons are responsible for the low-energy excitations, while σ electrons form energy bands far away from the Fermi energy. p_z orbitals allow hopping between carbon atoms and thus can be described by the tight-binding model. Considering p_z orbitals of graphene, Wallace derived the tight-binding model of graphene for the first time in 1947 [Wallace, 1947].

This chapter is organized as follows: The lattice structure of graphene is briefly described in the first section 2.1. In Section

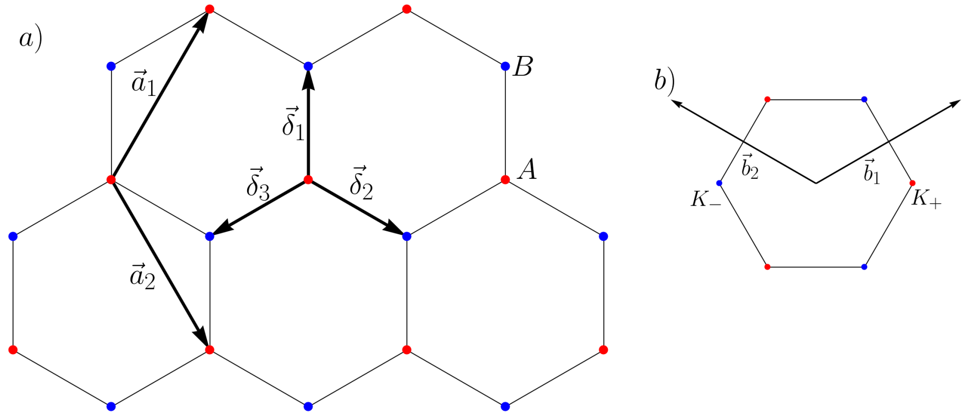

Figure 2.1: a) Lattice of graphene with $\vec{a}_1$ and $\vec{a}_2$ denoting lattice vectors, and $\vec{\delta}_1$, $\vec{\delta}_2$, and $\vec{\delta}_3$ the nearest-neighbor vectors b) first Brillouin zone of graphene with the reciprocal-lattice vectors $\vec{b}_1$ and $\vec{b}_2$ and the Dirac points K_+ and K_-.

2.2, we derive the tight-binding approximation of the valence and conduction band of graphene considering the nearest-neighbor interactions and overlap interactions. The topological properties of graphene are addressed in Section 2.3. Numerical calculations of the density of states are given in Section 2.4.

2.1 LATTICE STRUCTURE

Graphene consists of carbon atoms arranged in honeycomb lattice, as shown in Fig.(2.1). The honeycomb lattice is not a Bravais lattice and can be considered as two triangular Bravais lattices with the basis formed by two atoms, sites A and B.

The span of the triangular Bravais lattice is defined by two lattice vectors $\vec{a}_i$

$$\vec{a}_1 = \frac{a}{2}\left(1, \sqrt{3}\right) \qquad \vec{a}_2 = \frac{a}{2}\left(-1, \sqrt{3}\right) \tag{2.1}$$

where $a = \sqrt{3}a_{C-C}$ with $a_{C-C} \approx 0.142$ nm is the distance between two nearest carbon atoms. Using a Fourier transform of the Brillouin zone Fig.(2.1), the primitive cell in the momentum space is defined by the reciprocal lattice vectors

$$\vec{b}_1 = \frac{2\pi}{\sqrt{3}a}(\sqrt{3}, 1), \qquad \vec{b}_2 = \frac{2\pi}{\sqrt{3}a}(-\sqrt{3}, 1) \tag{2.2}$$

as

$$\vec{a}_i\vec{b}_j = 2\pi\delta_{ij} \tag{2.3}$$

where δ_{ij} denotes the Kronecker delta. The corners of the Brillouin zone are called Dirac points and only two of them are not equivalent

$$K_{\pm} = \pm\frac{4\pi}{3a}\,(1,0)\,. \tag{2.4}$$

Every A atom is connected with three nearest B atoms with nearest–nearest vectors

$$\vec{\delta}_1 = a(0,\frac{1}{\sqrt{3}}), \qquad \vec{\delta}_2 = \frac{a}{2}(1,-\frac{1}{\sqrt{3}}), \qquad \vec{\delta}_3 = \frac{a}{2}(-1,-\frac{1}{\sqrt{3}}). \tag{2.5}$$

2.2 ELECTRONIC STRUCTURE OF GRAPHENE

The tight-binding model is a simple and effective tool to describe the energy bands of a crystal structure. In this model, it is assumed that in the vicinity of every lattice point, the crystal Hamiltonian can be approximated by the Hamiltonian of a single atom $\mathcal{H}_{at}$ [Ashcroft and Mermin, 1976]

$$\mathcal{H}_{at}\psi_n(\vec{r}) = E_j\psi_n(\vec{r}). \tag{2.6}$$

A further assumption is that the bound levels of the Hamiltonian $\mathcal{H}_{at}$ are well localized, i.e. the $\psi_n(\vec{r})$ are very small when $\vec{r}$ is larger than the distance of the lattice spacing. The entire crystal is described by the Hamiltonian

$$\mathcal{H} = \mathcal{H}_{at} + U(\vec{r}) \tag{2.7}$$

which includes the spatially periodic lattice potential $U(\vec{r})$. Because the honeycomb lattice of graphene has two atoms per unit cell, the eigenstates of the Hamiltonian Eq.(2.7) are given as a linear combination of two Bloch functions $\psi^{A}_{\vec{k}}(\vec{r})$ and $\psi^{B}_{\vec{k}}(\vec{r})$

$$\begin{aligned}\psi_{\vec{k}}(\vec{r}) =& c_A\psi^{A}_{\vec{k}}(\vec{r}) + c_B\psi^{B}_{\vec{k}}(\vec{r})\\ =& \frac{1}{\sqrt{N}}\sum_j e^{i\vec{k}\vec{R}_j}\left(c_A(\vec{k})\phi(\vec{r}-\vec{R}^{A}_{j}) + c_B(\vec{k})\phi(\vec{r}-\vec{R}^{B}_{j})\right)\end{aligned} \tag{2.8}$$

where N is the number of elementary cells, and $c_A(\vec{k})$ and $c_B(\vec{k})$ are complex functions of the momentum $\vec{k}$. The $\phi(\vec{r}-\vec{R}^{A}_{j})(\phi(\vec{r}-\vec{R}^{B}_{j}))$ are atomic wavefunctions around the positions of the A (B) atoms at the lattice site, respectively

$$R^{A}_{j} = n_1\vec{a}_1 + n_2\vec{a}_2$$

$$R_j^B = R_j^A + \vec{\delta}_1. \tag{2.9}$$

where n_1 and n_2 are integers. By multiplication of the Schrödinger equation $\mathcal{H}\psi_{\vec{k}}(\vec{r}) = \epsilon_{\vec{k}}\psi_{\vec{k}}(\vec{r})$ with $\psi_{\vec{k}}(\vec{r})$, one can obtain

$$(c_A^*(\vec{k}), c_B^*(\vec{k}))\mathcal{H}_{\vec{k}} \begin{pmatrix} c_A(\vec{k}) \\ c_B(\vec{k}) \end{pmatrix} = \epsilon_{\vec{k}}(c_A^*(\vec{k}), c_B^*(\vec{k}))\mathcal{S}_{\vec{k}} \begin{pmatrix} c_A(\vec{k}) \\ c_B(\vec{k}) \end{pmatrix} \tag{2.10}$$

where the $\epsilon_{\vec{k}}$ are the energy bands. Considering only the hopping of the electrons between nearest– sites, the transfer matrix $\mathcal{H}_{\vec{k}}$ and the overlap map $\mathcal{S}_{\vec{k}}$ become

$$\mathcal{H}_{\vec{k}} = \begin{pmatrix} \epsilon_A & -t\gamma(\vec{k}) \\ -t\gamma^*(\vec{k}) & \epsilon_B \end{pmatrix}, \qquad \mathcal{S}_{\vec{k}} = \begin{pmatrix} 1 & s_0\gamma(\vec{k}) \\ s_0\gamma^*(\vec{k}) & 1 \end{pmatrix} \tag{2.11}$$

where t is the nearest– neighbor hopping energy, s_0 is the on-site energy and ϵ_A (ϵ_B) are on-site energies of the A(B) lattice sites, respectively; the function $\gamma(\vec{k}) = \sum_{\vec{\delta}_i} e^{i\vec{k}\vec{\delta}_i}$ is the geometric structural factor and depends up to a phase factor of the choice of the nearest-neighbor vectors $\vec{\delta}_i$. For details of the calculations of the elements of $\mathcal{H}_{\vec{k}}$ and $\mathcal{S}_{\vec{k}}$ we refer the reader to the recent reviews Refs. [McCann and Koshino, 2013,Goerbig, 2011]. Solving the secular equation of the Eq.(2.10), we find the energies for intrinsic graphene when $\epsilon_A = \epsilon_B = 0$

$$E_\pm = \frac{\pm t|\gamma(\vec{k})|}{1 \mp s_0|\gamma(\vec{k})|}. \tag{2.12}$$

The tight-binding parameter values are $t \approx 3.033$eV and $s_0 \approx 0.129$eV [Saito et al., 1998]. The energy description of graphene is visualized over the entire Brillouin zone in Fig.(2.2).

The valence band is completely filled and touches the completely empty conduction band at the Dirac points. Furthermore, $\gamma(\vec{k})$ can be approximated around Dirac points up to linear order of the momentum as

$$\gamma(K_\nu + \vec{k}) \approx \frac{\sqrt{3}a}{2}(-\nu k_x + ik_y) \tag{2.13}$$

where $\nu = \pm 1$ detonates the valley degeneracy. Neglecting the s_0, of which the effects are small and irrelevant at low energies around the Dirac points, see Fig.(2.3), the low-energy excitations have linear dispersion

$$\epsilon(K_\nu + \vec{k}) \approx \nu v_F|k| \tag{2.14}$$

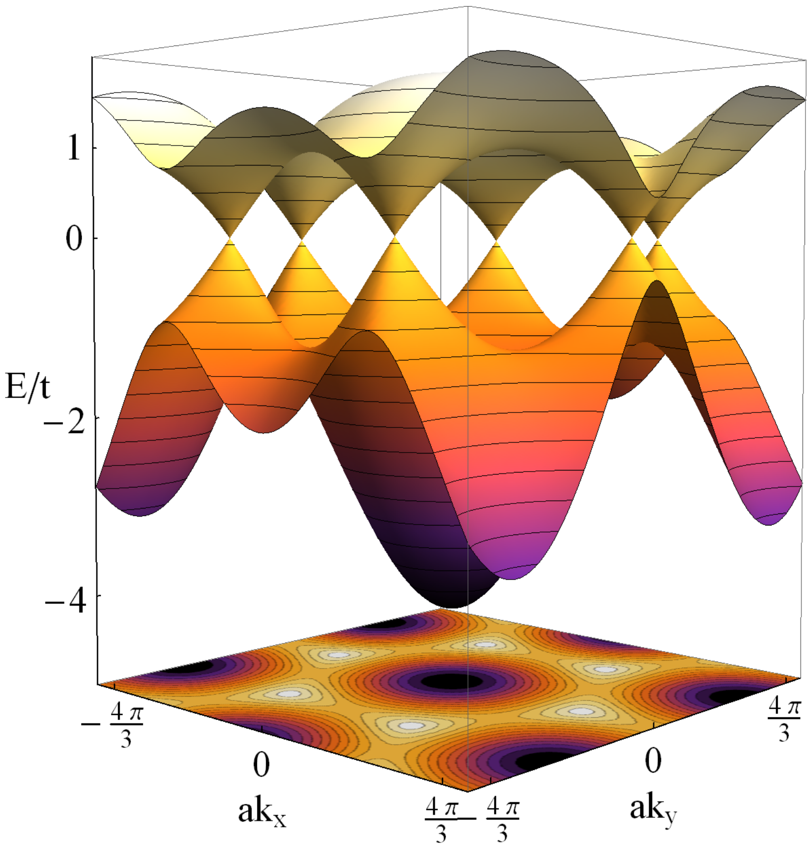

Figure 2.2: Energy description of graphene within the entire Brillioun zone for $t = 3.033$ eV, and $s_0 = 0.129$eV. The dispersions show a linear dispersion relation around every Dirac cone.

and propagate with the Fermi–Dirac velocity $v_F = \sqrt{3}at/2$, which is independent of their momentum $p = \hbar k$ (as photons with the speed of light "v_F"). These kinds of excitations are protected by the symmetry of the honeycomb lattice of graphene and described by the Hamiltonian

$$\mathcal{H}(K_\nu + \vec{k}) = v_F \vec{\sigma}_\nu \vec{k} \tag{2.15}$$

which has essentially the form of the Dirac equation which describes relativistic massless fermions (with velocity v_E). Here, $\vec{\sigma}_\nu = (\nu\sigma_x, \sigma_y)$ are Pauli Matrices, which represent the sublattice pseudospin with valley degeneracy. To summarize, the low-energy excitations are massless chiral Dirac fermions with a linear dispersion relation.

2.3 TOPOLOGICAL INVARIANTS

Among other interesting and fascinating properties, graphene possesses nontrivial topological properties.

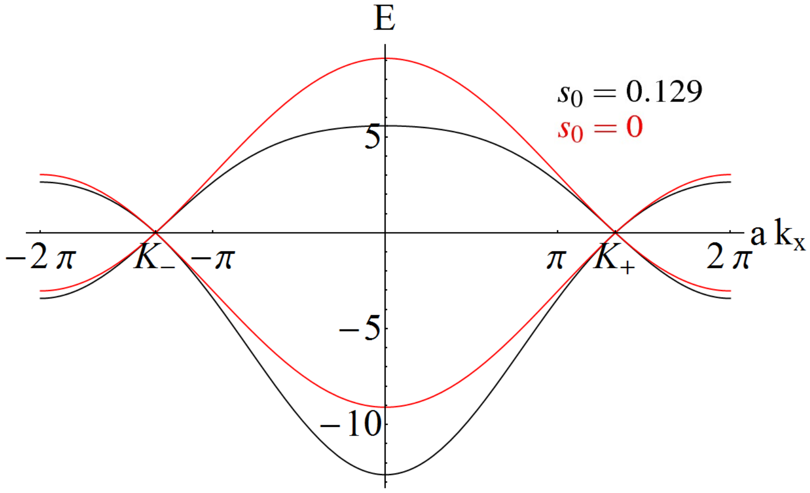

Figure 2.3: Energy bands of graphene plotted along the k_x axis. The effects of the parameter s_0 are small and irrelevant at low energies around the Dirac points.

The space inversion and time-reversal symmetry have essential roles in the topological properties of graphene. The space inversion is defined as

$$I: \quad \mathcal{H}(\vec{k}) = \sigma_x \mathcal{H}(-\vec{k}) \sigma_x. \tag{2.16}$$

Whereas, the time-reversal symmetry is defined as

$$T: \quad \mathcal{H}(\vec{k}) = \mathcal{H}^*(-\vec{k}). \tag{2.17}$$

In the context of graphene, the Berry phase is the phase that an eigenstate acquires after the electron wavevector in graphene completes a full cycle at constant energy around a Dirac point. The eigenstates of graphene read

$$\chi_\pm(\vec{k}) = \frac{1}{\sqrt{2}} \begin{pmatrix} 1 \\ \mp e^{i\phi(\vec{k})} \end{pmatrix} \tag{2.18}$$

where the phase $\phi(\vec{k})$ is $\phi(\vec{k}) = \gamma(\vec{k})/|\gamma(\vec{k})|$. The eigenstates are smooth and well-defined functions of the wavevector, except for at the locations of Dirac cones.

The degeneracy points of the eigenstates act as sources of the Berry curvature, defined as

$$F(\vec{k}) = \frac{\partial A_y}{\partial k_x} - \frac{\partial A_x}{\partial k_y} \tag{2.19}$$

where the Berry connection

$$\vec{A}(\vec{k}) = i \langle \chi_\pm(\vec{k}) | \frac{\partial}{\partial \vec{k}} | \chi_\pm(\vec{k}) \rangle. \tag{2.20}$$

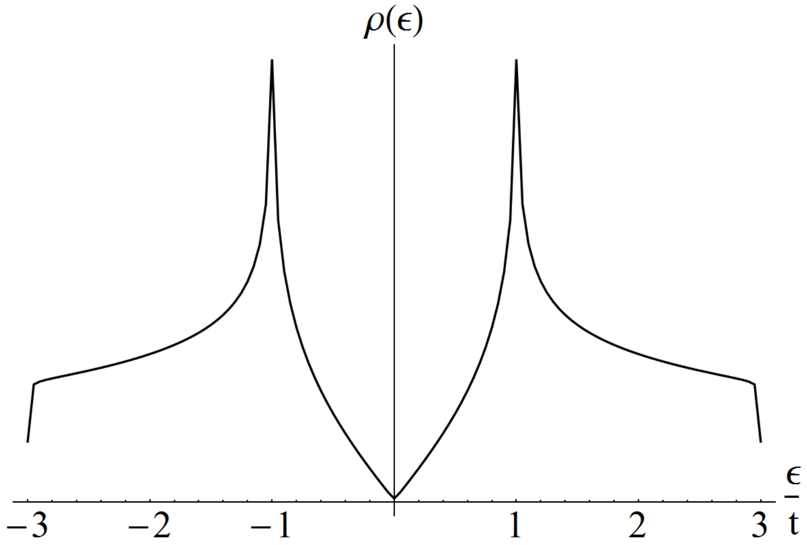

Figure 2.4: Single particle density of states of graphene as a function of energy ϵ in units of t. The van-Hove singularity points occur at $\epsilon/t = \pm 1$.

In graphene, the Berry curvature due to the time-reversal and space inversion symmetry vanishes everywhere outside the Dirac cones where quantized "monopole" sources of the δ-function type exist.

The Berry is defined as an integral over a closed path in $\vec{k}$ space [Xiao et al., 2010]. Thus, integrating over a closed path around one Dirac cone $K_\pm$ yields the Berry phase $\pm\pi$. The nontrivial topological quantity, the Berry phase, implies that the Dirac cones are topologically protected.

2.4 DENSITY OF STATES

Fig.(2.4) shows the single particle density of states, obtained by numerically integrating the spectral function [Bena and Kivelson, 2005]

$$\rho(\epsilon) = \int \frac{dk^2}{4\pi^2} A(\vec{k}, \epsilon) \tag{2.21}$$

over first Brillioun zone, where

$$A(\vec{k}, \epsilon) = -2\mathrm{Im}\left(\left(\epsilon - t|\gamma(\vec{k})| + i\eta\right)^{-1} + \left(\epsilon + t|\gamma(\vec{k})| + i\eta\right)^{-1}\right). \tag{2.22}$$

We perform the numerical calculations for a finite inverse lifetime of the quasiparticle $\eta = 0.005$ t. The van-Hove singularity points are points where the density of states possesses singularities. As can be seen from Fig.(2.4), the van-Hove singularity points occur at $\epsilon/t = \pm 1$. Furthermore, at low energies $|\epsilon|/t < 1$ the density of states has a v-shape, while at energies $|\epsilon|/t > 3$ the density of states goes to zero.

The finite value of the inverse lifetime η, which goes to zero, has two consequences:

1. the density of states at $\epsilon = 0$ has a very small value and goes to zero as $\rho(0) \approx \eta \ln(1/\eta)$,
2. the divergence of the density of states at van-Hove singularity points as $\rho(\pm t) \approx \ln(1/\eta)$.

3

GRAPHENE BILAYERS: ENERGY VERSUS ENTANGLEMENT

Graphene bilayers were isolated soon after the graphene monolayer. The low-energy excitations are massive chiral fermions, which do not exist in high-energy physics. The main consequences of this are the integer Quantum Hall effect without plateau at zero and the non-trivial Berry's phase of 2π [Novoselov et al., 2006].

Quantum entanglement, primarily a source of quantum information, has developed into one of the most studied subfields of many-body physics. In the last decade, quantum entanglement has mainly been used to study phase structure in condensed matter physics [Amico et al., 2008]. The entanglement spectrum of a bipartite system of subsystems A and B is defined in terms of the Schmidt decomposition of its ground state $|\psi\rangle$ as

$$|\psi\rangle = \sum_{n} e^{-\frac{\xi_n}{2}} |\psi_n^A\rangle |\psi_n^B\rangle \tag{3.1}$$

where the states $|\psi_n^A\rangle$ ($|\psi_n^B\rangle$) are orthonormal states of the subsystem A (B), respectively, and the non-negative quantities ξ_n represent the levels of the entanglement spectrum. In many previous studies, the proportionality between the energetic Hamiltonian of the subsystem A $\mathcal{H}_A$ and the entanglement Hamiltonian $\mathcal{H}_{ent}$ in the strong coupling regime between rungs [Poilblanc, 2010, Cirac et al., 2011, Schliemann, 2011, Peschel and Chung, 2011, Läuchli and Schliemann, 2012, Schliemann and Läuchli, 2012, Schliemann, 2013, Predin, 2017] has been observed.

The starting point of this chapter is to recapture the energy description of graphene bilayers considering only the hopping parameter between nearest neighbors on honeycomb lattice and the hopping parameter between neighbor sites that are on top of each other. The effects of the term that causes the trigonal warping [McCann and Koshino, 2013, Rozhkov et al., 2016] in graphene bilayers will be a central point of Chapter 4. Furthermore, we will neglect the term breaking the particle–hole symmetry. In this chapter, we analytically consider the entanglement spectrum of the free fermionic system on a graphene bilayers in a Bernal stacking arrangement. In the limit of strongly coupled layers, there is a proportionality between the entanglement Hamiltonian of graphene bilayers obtained by tracing out one layer, and the energetic Hamiltonian of the graphene monolayer. Then, we place a special focus on the effects of this proportionality on thermodynamic and topological properties of the entanglement Hamiltonian. We also study the entanglement spectrum of graphene bilayers in the presence of the bias voltage and the mass term.

The tight-binding description of graphene bilayers is studied in Section 3.1. In Section 3.2, we start with a brief review of the method for analytical derivation of the entanglement spectrum of the free fermionic system given in Refs. [Peschel, 2003, Cheong and Henley, 2004, Schliemann, 2013]. Then, we analyze the entanglement spectrum of graphene bilayers obtained by tracing out one layer and applied the concept of the entanglement thermodynamics. Furthermore, we also stress here an agreement in the topology of the entanglement Hamiltonian of graphene bilayers and the energy Hamiltonian of a graphene monolayer, due to the proportionality between these Hamiltonians. Then, we study the entanglement spectrum of graphene bilayers obtained by tracing out other two of possible four sublattices. In Section 3.3, we give an explicit equation for entanglement levels when the bias voltage or mass term are included. Finally, we close this chapter with a brief conclusion and an outlook in Section 3.4.

3.1 ELECTRONIC STRUCTURE OF GRAPHENE BILAYERS

Graphene bilayers consist of two coupled layers via Van der Walls forces. The unit cell of graphene bilayers has four carbon atoms, A1, B1 on the lower layer and A2, B2 on the upper layer. The layers are arranged in the Bernal stacking [McCann and Koshino, 2013, Rozhkov et al., 2016], where one atom at the B1 site is directly below an atom at the A2 site Fig.(3.1).

Then, the integral matrix of the graphene bilayers has the following form [McCann and Koshino, 2013]

$$\mathcal{H}_{\vec{k}} = \begin{pmatrix} \epsilon_{A1} & -t\gamma(\vec{k}) & t_4\gamma(\vec{k}) & -t_3\gamma^*(\vec{k}) \\ -t\gamma^*(\vec{k}) & \epsilon_{B1} & t_\perp & t_4\gamma(\vec{k}) \\ t_4\gamma^*(\vec{k}) & t_\perp & \epsilon_{A2} & -t\gamma(\vec{k}) \\ -t_3\gamma(\vec{k}) & t_4\gamma^*(\vec{k}) & -t\gamma^*(\vec{k}) & \epsilon_{B2} \end{pmatrix} \tag{3.2}$$

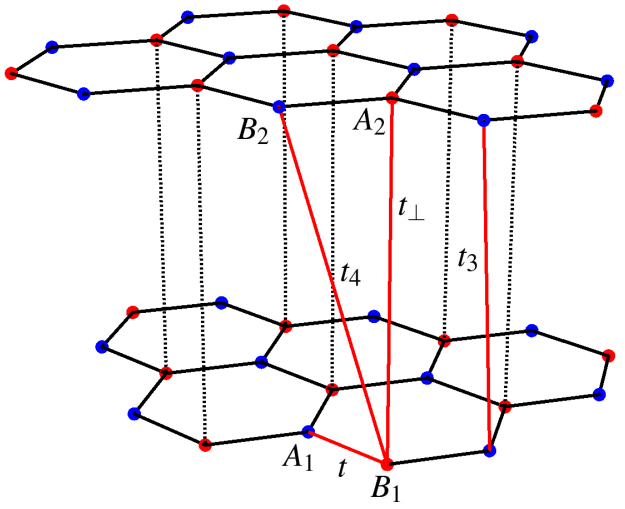

Figure 3.1: Schematic representation of Bernal-stacked bilayer graphene. Two sublattices of each layer are represented by red and blue spheres. The intralayer hopping parameter t between nearest electrons and also interlayer hopping parameters t, t_3, and t_4 are represented by red lines.

in the basis $\left(a^\dagger_{1\vec{k}}, b^\dagger_{1\vec{k}}, a^\dagger_{2\vec{k}}, b^\dagger_{2\vec{k}}\right)|0\rangle$ where $a^\dagger_{i\vec{k}}$ $(a_{i\vec{k}})$ and $b^\dagger_{i\vec{k}}$ $(b_{i\vec{k}})$ create (annihilate) electrons layers $i = 1, 2$ on sublattice A and B, respectively.. Here, $\gamma(\vec{k}) = \sum_{\vec{\delta}} \exp(i\vec{k} \cdot \vec{\delta})$ with $\vec{\delta}$ being nearest–neighbor vectors on a graphene monolayer, defined by Eq.(2.5). ϵ_{A1}, ϵ_{B1}, ϵ_{A2} and ϵ_{B2} are on-site energies. The parameter t is the hopping parameter between nearest-neighbor atoms within each layer, while $t_\perp$ describes coupling between atoms at the sites B1 and A2. The parameter t_3 is the interlayer hopping parameter between atoms A1 and B2 and causes trigonal warping. Whereas the parameter t_4 is the interlayer hoping parameter between A1 and A2 and B1 and B2 and leads to the electron–hole asymmetry. Hopping parameters are represented in Fig.(3.1). Effects of the parameters t_3 on the energy, and as well entanglement spectrum will be discussed in Chapter 4. Since, the eigenvalues and eigenstates of the Hamiltonian Eq.(3.2) cannot be obtained in closed analytical form when the hopping parameter t_4 is included, we will neglect it in this thesis. The experimentally established values [Kuzmenko et al., 2009] for these parameters are $t = 3.16$eV, $t_\perp = 0.381$eV, $t_3 = 0.38$eV, and $t_4 = 0.14$eV.

Furthermore, we will neglect the overlap matrix, since it has only a small and irrelevant influence around the Dirac cones. For

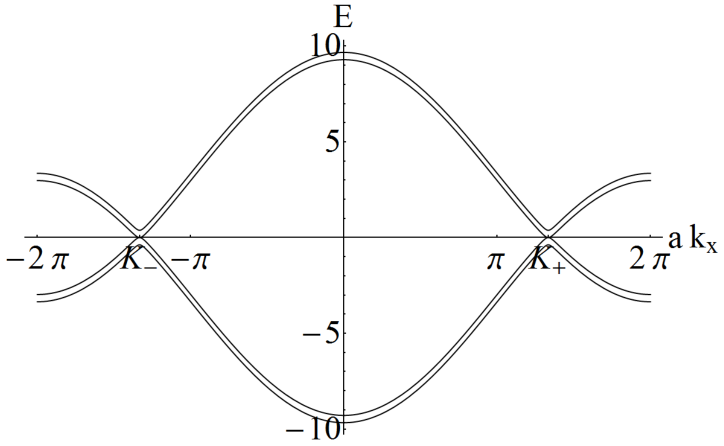

Figure 3.2: The energy bands of graphene bilayers plotted along the k_x axis for $t = 3.16$eV, and $t_\perp = 0.381$eV. The dispersions show a quadratic dispersion relation around every Dirac cone.

intrinsic graphene bilayers when $\epsilon_{A1} = \epsilon_{A2} = \epsilon_{B1} = \epsilon_{B2} = 0$ solving the eigenproblem of the Hamiltonian Eq.(3.2) we obtain the symmetric energy spectrum with four bands $\pm E_1(\vec{k})$ and $\pm E_2(\vec{k})$

$$E_{1,2}(\vec{k}) = \pm\frac{1}{2}t_\perp + \sqrt{\frac{t_\perp^2}{4} + t^2|\gamma(\vec{k})|^2}, \tag{3.3}$$

a pair of conduction bands and a pair of the valence bands. The energy bands structure of graphene bilayers is plotted along the k_x axis in the momentum space in Fig.(3.2).

The Hamiltonian that describes the properties of electrons in the vicinity of the Dirac points $\vec{k} + K_\nu$ ($\nu = \pm 1$ detonates the valley degeneracy) can be approximated within the Dirac cone approximation

$$\mathcal{H}_{\vec{k}+K_\nu} = \begin{pmatrix} 0 & v_F\pi^\dagger & 0 & 0 \\ v_F\pi & 0 & t_\perp & 0 \\ 0 & t_\perp & 0 & v_F\pi^\dagger \\ 0 & 0 & v_F\pi & 0 \end{pmatrix} \tag{3.4}$$

where v_F is the Fermi-Dirac velocity, and $\pi = \nu p_x + ip_y$ and $\pi^\dagger = \nu p_x - ip_y$. Energy bands Eq.(3.3) can be approximated around Dirac points

$$E_{1,2} = \nu m^* v_F^2 + \sqrt{(m^* v_F^2)^2 + p^2 v_F^2} \tag{3.5}$$

where m^* is the effective mass of the quasiparticles $m^* = \frac{t_\perp}{2v_F^2}$ and it is directly proportional to the hopping parameter $t_\perp$. Thus, the mass of the quasiparticles directly arises from the interaction between the layers. Even more, at small momentum, the energy band Eq.(3.3)

$$E_1 = \frac{p^2}{2m^*} \tag{3.6}$$

shows the quadratic dispersion. However, these excitations are not classical massive quasiparticles, which are the most common in the condensed matter physics. Similar to the case of graphene, we will prove the chirality of the quasiparticle in graphene bilayers by showing that they can be described by the generalized Dirac Hamiltonian with elements $\frac{p^2}{2m^*}$. In this sense, it is necessary to rewrite the Hamiltonian Eq.(3.4), which possesses information about the high-energy bands $\pm E_1$ as the low-energy effective Hamiltonian which possesses the information only about the low-energy bands $\pm E_2$ [McCann and Fal'ko, 2006]. Keeping only terms up to linear in $t_\perp$ we find

$$\mathcal{H}_{\vec{k}}^{(eff)} = -\begin{pmatrix} 0 & \frac{t^2}{t_\perp}\left(\gamma^*(\vec{k})\right)^2 \\ \frac{t^2}{t_\perp}\left(\gamma(\vec{k})\right)^2 & 0 \end{pmatrix} \tag{3.7}$$

in the basis $\left(b^\dagger_{2\vec{k}}, a^\dagger_{1\vec{k}}\right)|0\rangle$ and it is good approximation in the energy range $|E_2| < \frac{1}{4}t_\perp$. It the vicinity of the Dirac point K_ν the effective Hamiltonian Eq.(3.7) can be approximated by the Dirac cone approximation to

$$\mathcal{H}_{\vec{k}+K_\nu}^{(eff)} = -\nu\frac{\hbar^2 v_F^2}{t_\perp}\begin{pmatrix} 0 & (\pi^\dagger)^2 \\ \pi^2 & 0 \end{pmatrix} \tag{3.8}$$

It is more convenient to write this Hamiltonian in the following form

$$\mathcal{H}_{\vec{k}+K_\nu}^{(eff)} = -\nu\frac{\hbar^2 k^2}{2m^*}\vec{\sigma}\vec{n} \tag{3.9}$$

where $\vec{k} = (k\cos(\phi_{\vec{k}}), k\sin(\phi_{\vec{k}}))$ and $\vec{n} = (n\cos(2\phi_{\vec{k}}), n\sin(2\phi_{\vec{k}}))$. $\vec{\sigma}$ denote Pauli matrices. To conclude, the low-energy excitations are massive chiral particles with the quadratic dispersion. In quantum electrodynamics, only massless particles are chiral and thus graphene bilayers become an exciting playground for studying properties of massive chiral quasiparticles that do not exist in quantum electrodynamics.

3.1.1 *Topological invariants*

The Hamiltonian Eq.(3.2) of intrinsic graphene fulfills the time-reversal symmetry

$$\mathcal{H}^*(\vec{k}) = \mathcal{H}(-\vec{k}) \tag{3.10}$$

and the space inversion symmetry

$$(\sigma_x \otimes \sigma_x)\,\mathcal{H}(\vec{k})\,(\sigma_x \otimes \sigma_x) = \mathcal{H}(-\vec{k}). \tag{3.11}$$

The eigenstates of the effective Hamiltonian Eq.(3.7)

$$|\chi_\pm\rangle = \frac{1}{\sqrt{2}} \begin{pmatrix} 1 \\ \mp \mathrm{e}^{2i\phi(\vec{k})} \end{pmatrix} \tag{3.12}$$

with $\phi(\vec{k}) = \gamma(\vec{k})/|\gamma(\vec{k})|$. The singularities of these eigenstates at the Dirac points act as the sources of the Berry curvature flux

$$F(\vec{k}) = \frac{\partial A_y}{\partial k_x} - \frac{\partial A_x}{\partial k_y} \tag{3.13}$$

where the Berry connection

$$\vec{A}(\vec{k}) = i\langle\chi_\pm(\vec{k})|\frac{\partial}{\partial \vec{k}}|\chi_\pm(\vec{k})\rangle. \tag{3.14}$$

Integrating the Berry connection $\vec{A}$ over a closed path, it is found that the Dirac cone $K_\pm$ contributes $\pm 2\pi$ to the Berry phase.

3.2 ENTANGLEMENT SPECTRUM

3.2.1 *Method*

For systems of free fermions as studied here, the entanglement Hamiltonian can be formulated as a single-particle operator [Peschel, 2003, Cheong and Henley, 2004, Schliemann, 2013].

Consider first a system of free fermions described by Hamiltonian

$$\mathcal{H} = \sum_{i,j} t_{ij} c_i^\dagger c_j \tag{3.15}$$

where t_{ij}-hopping parameter, and $c_i^\dagger$ (c_i) creates (annihilates) an electron on the i-th site.

The one-particle function determined by the ground state $|\psi\rangle$ of the previous Hamiltonian Eq. (3.15) reads

$$C_{ij} = \langle\psi|c_i^\dagger c_j|\psi\rangle = \mathrm{tr}\left(\rho c_i^\dagger c_j\right) \tag{3.16}$$

where ρ is the density matrix.

In this thesis, we restrict our considerations to a bipartite system, which consists of two subsystems A and B. Since the reduced density ρ_A, obtained by tracing out subsystem B, does not have any negative eigenvalues, it can be always reformulated as

$$\rho_A = \frac{1}{Z} e^{-\mathcal{H}_A} \tag{3.17}$$

with the entanglement spectrum $\mathcal{H}_A$ and the partition function $Z = \mathrm{tr}\left(e^{-\mathcal{H}_A}\right)$.

Now, we will consider only the subsystem A, which has L sides. It is clear that the correlation matrix in this subsystem has the following form

$$C_{\alpha\beta} = \mathrm{tr}_A(\rho_A c_\alpha^\dagger c_\beta) = \langle\psi|c_\alpha^\dagger c_\beta|\psi\rangle \tag{3.18}$$

where $|\psi\rangle$ is the ground state of the composite system, and single-particle operators c_α, c_β act on its remaining part after tracing out a subsystem.

In order to represent all correlation functions in the free fermion subsystem A, the entanglement Hamiltonian $\mathcal{H}_A$ of the non-interacting system must have the following form

$$\mathcal{H}_A = \sum_{\alpha,\beta\in A} \mathcal{H}_{\alpha\beta} c_\alpha^\dagger c_\beta. \tag{3.19}$$

Furthermore, every Hamiltonian of free fermions Eq. (3.15) can be diagonalized using the unitary matrix U as

$$\mathcal{H} = UDU^\dagger \tag{3.20}$$

where $D = \mathrm{diag}\,(E_1, E_2, ..., E_{N/2}, -E_1, -E_2, ..., -E_{N/2})$, with E_i are eigenenergies. We use a new kind fermion operations a_α

$$a_\alpha = \sum_\beta U_{\beta\alpha} c_\beta \tag{3.21}$$

to calculate the correlation function in the set $\{|\lambda\rangle\}$ of many-body eigenstates of $\mathcal{H}_A$

$$C_{\alpha\beta} = \langle c_\alpha^\dagger c_\beta\rangle_A$$

$$\begin{aligned}&=\frac{\sum_\lambda\langle\lambda|c_\alpha^\dagger c_\beta e^{-\mathcal{H}_A}|\lambda\rangle}{\sum_{\lambda'}\langle\lambda'|e^{-\mathcal{H}_A}|\lambda'\rangle}\\&=\frac{\sum_\lambda\langle\lambda|\sum_{mn}a_m^\dagger U_{\alpha m}U_{\beta n}a_n e^{-\mathcal{H}_A}|\lambda\rangle}{\sum_{\lambda'}\langle\lambda'|e^{-\mathcal{H}_A}|\lambda'\rangle}.\end{aligned}\tag{3.22}$$

where

$$\sum_{\lambda'}\langle\lambda'|e^{-\mathcal{H}_A}|\lambda'\rangle=\sum_{\{n_\alpha\}}\langle\{n_\alpha\}|e^{-\sum_\alpha\xi_\alpha n_\alpha}|\{n_\alpha\}\rangle=\prod_\alpha\sum_{n_\alpha=\{0,1\}}e^{-\xi_\alpha n_\alpha}$$

and

$$\begin{aligned}&\sum_\lambda\langle\lambda|\sum_{mn}a_m^\dagger U_{\alpha m}U_{\beta n}a_n e^{-\mathcal{H}_A}|\lambda\rangle=\sum_{mn}U_{\alpha m}U_{\beta n}\sum_\lambda\langle\lambda|a_m^\dagger a_n e^{-\mathcal{H}_A}|\lambda\rangle\\&=\sum_l U_{\alpha l}U_{\beta l}\sum_\lambda\langle\lambda|n_l e^{-\mathcal{H}_A}|\lambda\rangle\\&=\sum_l U_{\alpha l}U_{\beta l}\sum_{\{n_\alpha\}}\langle\{n_\alpha\}|n_l e^{-\sum_\alpha\xi_\alpha n_\alpha}|\{n_\alpha\}\rangle\\&=\sum_l U_{\alpha l}U_{\beta l}\left(\prod_{\alpha\neq l}\sum_{n_\alpha=\{0,1\}}e^{-\xi_\alpha n_\alpha}\right)\sum_{n_l=\{0,1\}}e^{-\xi_l n_l}n_l\\&=\sum_l U_{\alpha l}U_{\beta l}\left(\prod_\alpha\left(1+e^{-\xi_\alpha n_\alpha}\right)\right)\frac{e^{-\xi_l}}{1+e^{-\xi_l}}.\end{aligned}$$

Finally, we get

$$C_{\alpha\beta}=\sum_l U_{\alpha l}U_{\beta l}\frac{e^{-\xi_l}}{1+e^{-\xi_l}}\tag{3.23}$$

where we sum only over states with negative energies, because only these states are occupied. The eigenvalues ξ_α of the entanglement Hamiltonian, known as entanglement levels. The entanglement Hamiltonian then can be reformulated as a single particle operator

$$\mathcal{H}_A=\sum_{\alpha=1}^{L}\xi_\alpha a_\alpha^\dagger a_\alpha.\tag{3.24}$$

The eigenvalues ξ_α are related to the eigenvalues η_α of the correlation matrix via

$$\xi_\alpha=\ln\left(\frac{1-\eta_\alpha}{\eta_\alpha}\right)=2\text{artanh}\left(1-2\eta_\alpha\right).\tag{3.25}$$

The entanglement levels form the entanglement spectrum. In particular, the entanglement Hamiltonian and the correlation matrix share the same system of eigenvectors.

Here, the only condition is that the eigenvalues of the correlation matrix lie between 0 and 1, which is always the case because they can be written in the form $\langle a_\alpha^\dagger a_\alpha\rangle$.

3.2.2 *Tracing out one layer*

Here, we will analytically obtain the entanglement spectrum by tracing out layer 1 from the ground state of the undoped graphene bilayers where all states with negative energies $(-E_1(\vec{k}))$, $(-E_2(\vec{k}))$ are occupied, while all others are empty. Then, the correlation matrix has the following form

$$\begin{aligned} C(\vec{k}) &= \begin{pmatrix} \langle a^\dagger_{2\vec{k}} a_{2\vec{k}} \rangle & \langle a^\dagger_{2\vec{k}} b_{2\vec{k}} \rangle \\ \langle b^\dagger_{2\vec{k}} a_{2\vec{k}} \rangle & \langle b^\dagger_{2\vec{k}} b_{2\vec{k}} \rangle \end{pmatrix} \\ &= \begin{pmatrix} \frac{1}{2} & u(\vec{k}) \\ u^*(\vec{k}) & \frac{1}{2} \end{pmatrix} \end{aligned} \tag{3.26}$$

where $u(\vec{k}) = \frac{1}{2} \mathrm{e}^{i\phi(\vec{k})} \frac{t|\gamma(\vec{k})|}{\sqrt{t^2|\gamma(\vec{k})|^2 + \frac{1}{4}t_\perp^2}}$.

The eigenvalues of the correlation matrix

$$\eta_\pm(\vec{k}) = \frac{1}{2}\left(1 \mp \frac{t|\gamma(\vec{k})|}{\sqrt{t^2|\gamma(\vec{k})|^2 + \frac{1}{4}t_\perp^2}}\right) \tag{3.27}$$

lead to the entanglement levels

$$\xi_\pm(\vec{k}) = \pm 2 \mathrm{arcsinh}\left(\frac{2t|\gamma(\vec{k})|}{t_\perp}\right). \tag{3.28}$$

These entanglement levels get into the entanglement Hamiltonian as

$$\mathcal{H}_{ent} = \sum_{n=\pm} \xi_n c^\dagger_{\vec{k}n} c_{\vec{k}n}. \tag{3.29}$$

Here, the operators $c_{\vec{k}n}$ diagonalize the energetic Hamiltonian.

The entanglement levels $\xi_\pm$ are represented in Fig. (3.3) in the entire Brilloun zone. At every Dirac point, two layers are maximally entangled $(1/t_\perp = 0)$ and the entanglement spectrum vanishes $\xi_\pm = 0$.

One can notice that the entanglement spectrum Eq. (3.28) for a given energy spectrum of a graphene monolayer depends only on the coupling parameter $t_\perp$. Furthermore, the entanglement spectrum $\xi_\pm$ in the limit of strongly coupled layers $t_\perp >> t|\gamma(\vec{k})|$ can be approximated as

$$\xi_\pm \approx \pm \frac{4t|\gamma(\vec{k})|}{t_\perp} \mp \frac{8t^3|\gamma(\vec{k})|^3}{3t_\perp^3} + \mathcal{O}\left(\frac{1}{t_\perp^5}\right). \tag{3.30}$$

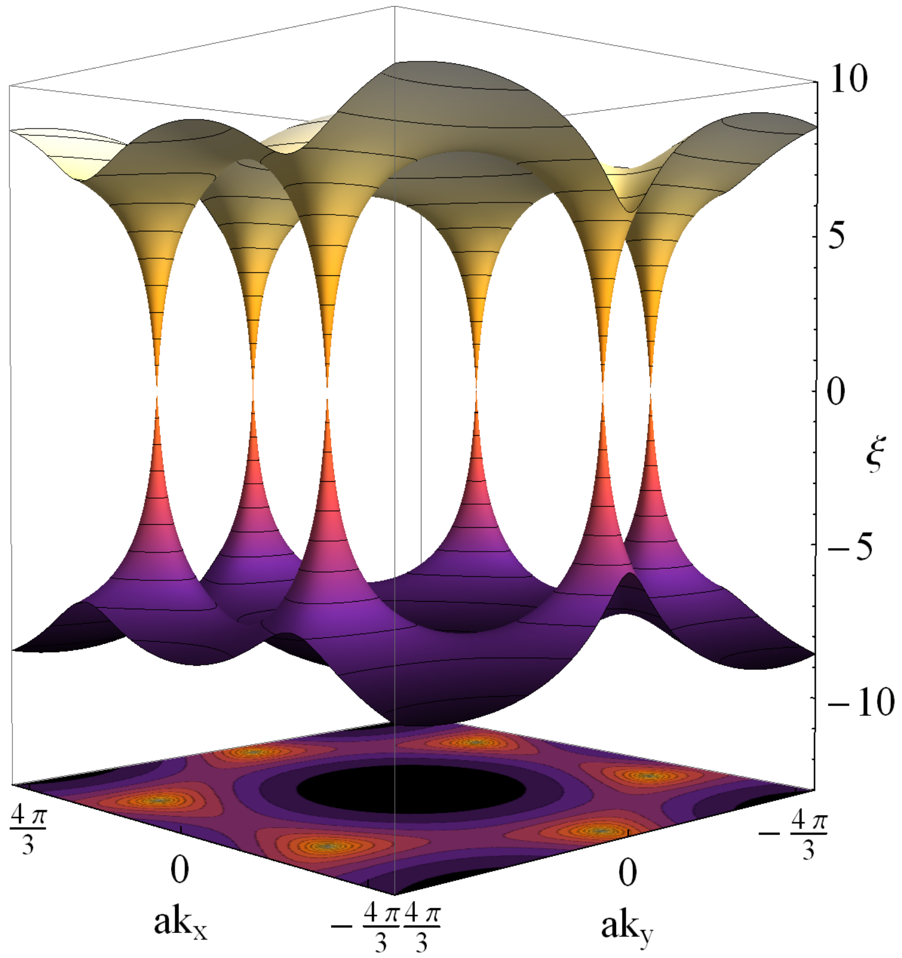

Figure 3.3: The entanglement spectrum $\xi_{\pm}(\vec{k})$ plotted for $t = 3.16$eV, $t_{\perp} = 0.381$eV over entire Brillouin zone. The contour plot represents the lower entanglement level ξ_{-}.

This implies the direct proportionality, in the limit of the strong coupling layers, between the entanglement spectrum $\xi_{\pm}$ of graphene bilayers and the energy spectrum $t|\gamma(\vec{k})|$ of a graphene monolayer

$$\xi_{\pm} \approx \frac{4}{t_{\perp}} t|\gamma(\vec{k})| \tag{3.31}$$

with the proportionality factor $\lambda = 4/t_{\perp}$, which is indeed the phenomenological inverse temperature [Schliemann, 2014]. As we shall see in the following, this proportionality has crucial consequences on the topological quantities of the entanglement Hamiltonian [Predin et al., 2016] and the entanglement thermodynamics [Schliemann, 2011, Schliemann, 2013, Schliemann, 2014].

Topological invariants

The entanglement Hamiltonian and the correlation matrix share the same eigenstates. Integrating the Berry connection constructed from the eigenstates of the correlation matrix over a closed path around the Dirac cone $K_\pm$, we find a Berry phase of $\pm\pi$. This result agrees with the Berry phase around the Dirac cones in monolayer graphene.

Entanglement thermodynamics

The entanglement entropy and entanglement energy are defined as functions of the reduced density matrix [Schliemann, 2011, Schliemann, 2013, Schliemann, 2014]

$$S = \langle -\ln \rho_{red} \rangle \tag{3.32}$$
$$\overline{E} = \langle \mathcal{H}_{ent} \rangle \tag{3.33}$$

where $\langle \cdot \rangle = \mathrm{tr}\left(\rho_{red} \cdot\right)$. Since the reduced density matrix can be rewritten as

$$\rho_{red}(\lambda) = \frac{\mathrm{e}^{-\mathcal{H}_{ent}(\lambda)}}{Z(\lambda)} = \sum_n \frac{\mathrm{e}^{-\xi_n(\lambda) c_n^\dagger c_n}}{1 + \mathrm{e}^{-\xi_n(\lambda)}}. \tag{3.34}$$

the entanglement entropy and energy have the following forms

$$\begin{aligned} S(\lambda) =& \sum_n \left(\frac{\ln\left(1 + \mathrm{e}^{-\xi_n(\lambda)}\right)}{1 + \mathrm{e}^{-\xi_n(\lambda)}} + \frac{\ln\left(1 + \mathrm{e}^{\xi_n(\lambda)}\right)}{1 + \mathrm{e}^{\xi_n(\lambda)}} \right) \\ =& \sum_n \left(\ln\left(1 + \mathrm{e}^{-\xi_n(\lambda)}\right) + \frac{\xi_n(\lambda)}{1 + \mathrm{e}^{\xi_n(\lambda)}} \right) \end{aligned} \tag{3.35}$$

$$\overline{E}(\lambda) = \sum_n \frac{\xi_n(\lambda)}{1 + \mathrm{e}^{\xi_n(\lambda)}}, \tag{3.36}$$

respectively. This leads to the expression for the entanglement free energy defined as

$$\overline{F} = \overline{E} - S. \tag{3.37}$$

Here, the thermodynamic relation

$$\frac{\partial S}{\partial E} = \frac{\partial S}{\partial \lambda} \frac{\partial \lambda}{\partial E} = \beta(\lambda) \tag{3.38}$$

holds, where $\beta(\lambda)$ is the inverse thermodynamic temperature. Furthermore, the connection between the entanglement Hamiltonian and canonical entanglement Hamiltonian $\mathcal{H}_{can}$ is

$$\mathcal{H}_{ent} = \beta(\lambda) \mathcal{H}_{can} \tag{3.39}$$

and allows us to define the entanglement inner energy as

$$E(\lambda) = \langle \mathcal{H}_{can} \rangle \tag{3.40}$$

and the free energy as

$$F(\lambda) = E(\lambda) - S(\lambda)/\beta(\lambda). \tag{3.41}$$

It is easy to obtain from Eq.(3.38)

$$\beta \frac{\partial \overline{F}}{\partial \beta} = \overline{E}. \tag{3.42}$$

Thus, the connection between the inverse thermodynamic temperature $\beta(\lambda)$ and the phenomenological inverse temperature λ is given by

$$\frac{\partial \beta(\lambda)}{\partial \lambda} = \frac{1}{\overline{E}} \frac{\partial \overline{F}}{\partial \lambda} = \frac{1}{\overline{E}} \frac{\partial \left(\overline{E} - S\right)}{\partial \lambda}. \tag{3.43}$$

Here, the entanglement entropy and entanglement energy is

$$\begin{aligned} S(\lambda) &= 2\ln\left(1 + \lambda t|\gamma(\vec{k})|\right) - \lambda t|\gamma(\vec{k})| \left(1 + \tanh\left(\frac{1}{2}\lambda t|\gamma(\vec{k})|\right)\right), \\ \overline{E}(\lambda) &= -\lambda t|\gamma(\vec{k})| \tanh\left(\frac{1}{2}\lambda t|\gamma(\vec{k})|\right), \end{aligned} \tag{3.44}$$

respectively. This leads to

$$\frac{\partial \left(\overline{E} - S\right)}{\partial \lambda} = -t|\gamma(\vec{k})| \tanh\left(\frac{1}{2}\lambda t|\gamma(\vec{k})|\right) \tag{3.45}$$

and further to

$$\frac{\partial \beta(\lambda)}{\partial \lambda} = \frac{1}{\lambda}. \tag{3.46}$$

The inverse thermodynamic temperature is proportional the phenomenological inverse temperature

$$\beta(\lambda) = k_E \lambda \tag{3.47}$$

where k_E is a constant. Finally, the canonical entanglement Hamiltonian is independent of the inverse temperature $\beta = 4k_E/t_\perp$, such that

$$\mathcal{H}_{can} = \frac{1}{k_E} \left(c^\dagger_{\vec{k},+} c_{\vec{k},+} - c^\dagger_{\vec{k},-} c_{\vec{k},-}\right). \tag{3.48}$$

3.2.3 *Tracing out A1 and B2 (or A2 and B1) sublattices*

The correlation matrix obtained by tracing out sublattices A1 and B2 lying in opposite layers has the following form

$$\begin{aligned} C(\vec{k}) &= \begin{pmatrix} \langle a^{\dagger}_{2\vec{k}} a_{2\vec{k}} \rangle & \langle a^{\dagger}_{2\vec{k}} b_{1\vec{k}} \rangle \\ \langle b^{\dagger}_{1\vec{k}} a_{2\vec{k}} \rangle & \langle b^{\dagger}_{1\vec{k}} b_{1\vec{k}} \rangle \end{pmatrix} \\ &= \begin{pmatrix} \frac{1}{2} & -v(\vec{k}) \\ -v(\vec{k}) & \frac{1}{2} \end{pmatrix} \end{aligned} \tag{3.49}$$

where $v(\vec{k}) = \frac{1}{4} \frac{t_\perp}{\sqrt{t^2 |\gamma(\vec{k})|^2 + \frac{1}{4} t_\perp^2}}$.

One can notice that the off-diagonal terms of the correlation matrix Eq.(3.26) and the correlation matrix Eq.(3.49) satisfy the relation

$$|u(\vec{k})|^2 + |v(\vec{k})|^2 = \frac{1}{4}. \tag{3.50}$$

The eigenvalues $\eta_\pm$ of this correlation matrix

$$\eta_\pm = \frac{1}{2} \left(1 \pm \frac{\frac{1}{2} t_\perp}{\sqrt{t^2 |\gamma(\vec{k})|^2 + \frac{1}{4} t_\perp^2}} \right) \tag{3.51}$$

escort the entanglement levels

$$\xi_\pm = \pm 2 \operatorname{arsinh} \left(\frac{t_\perp}{2t |\gamma(\vec{k})|} \right). \tag{3.52}$$

In Fig.(3.4) we visualize the eigenvalue η_- of the correlation matrix around a given K-point.

In the Dirac points, the eigenvalues of the correlation matrix become $\eta_+ = 1$ and $\eta_- = 0$ and thus, the remaining subsystem is not entangled with the subsystem which is traced out.

Topological invariant

The entanglement gap is always opened, because the off-diagonal elements $v(\vec{k})$ of the correlation matrix do not vanish anywhere. This implies that the Berry curvature and all Berry phases are zero in entire Brillouin zone.

3.2.4 *Tracing out A1 and A2 (or B1 and B2) sublattices*

The correlation matrix given by tracing out A1 and A2 sublatties

$$C(\vec{k}) = \begin{pmatrix} \langle b^{\dagger}_{1\vec{k}} b_{1\vec{k}} \rangle & \langle b^{\dagger}_{1\vec{k}} b_{2\vec{k}} \rangle \\ \langle b^{\dagger}_{2\vec{k}} b_{1\vec{k}} \rangle & \langle b^{\dagger}_{2\vec{k}} b_{2\vec{k}} \rangle \end{pmatrix}$$

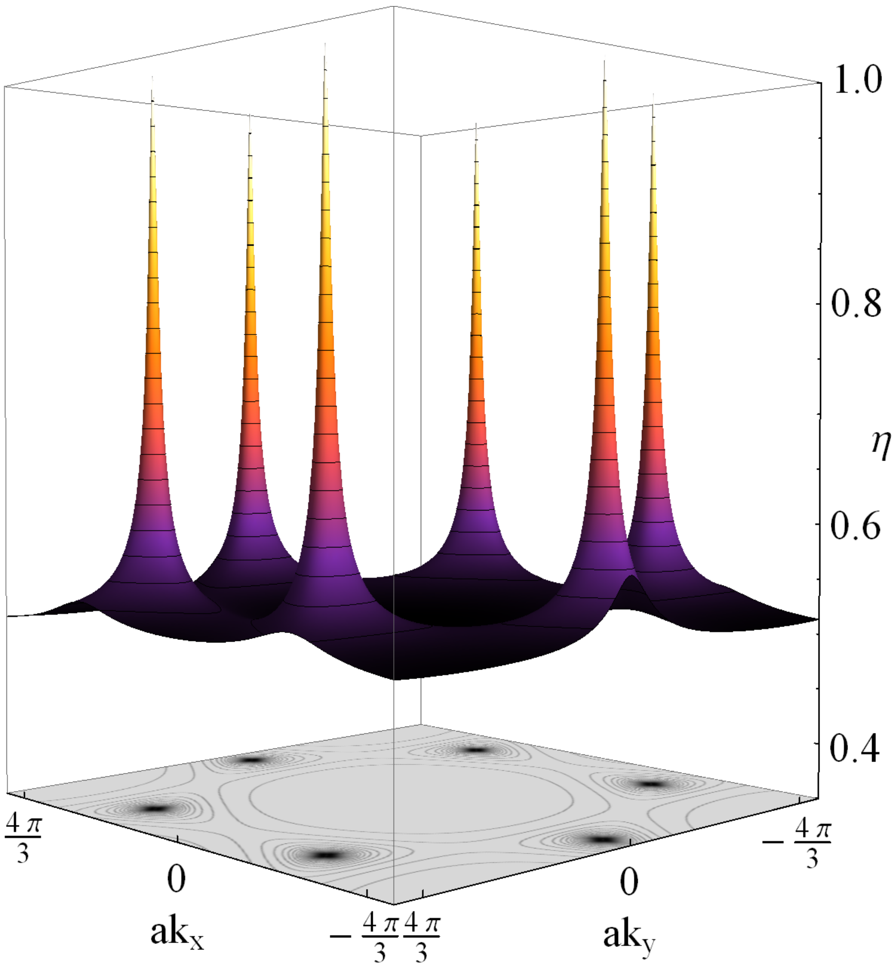

Figure 3.4: The eigenvalue $\eta_- = 1/2 + |v(\vec{k})|$ of the correlation matrix plotted over entire Brillouin zone for the same value of parameters as Fig.(3.2).

$$= \begin{pmatrix} \frac{1}{2} & 0 \\ 0 & \frac{1}{2} \end{pmatrix} \tag{3.53}$$

is proportional to the unit matrix. Thus, the remaining subsystem is maximally entangled with the traced out subsystem.

3.3 EFFECTS OF BIAS VOLTAGE AND MASS TERM

3.3.1 *Energy spectrum*

Bias voltage

Applying the bias voltage makes the difference of on-site energies Λ of different layers, thus the lower layer 1 of graphene bilayers is on the energy $\epsilon_{A1} = \epsilon_{B1} = -\frac{\Lambda}{2}$ and the upper layer 2 is on the energy $\epsilon_{A2} = \epsilon_{B2} = \frac{\Lambda}{2}$. Then the Hamiltonian Eq.(3.2) becomes

$$\mathcal{H}_{\vec{k}} = \begin{pmatrix} -\frac{\Lambda}{2} & -t\gamma(\vec{k}) & 0 & 0 \\ -t\gamma^*(\vec{k}) & -\frac{\Lambda}{2} & t_\perp & 0 \\ 0 & t_\perp & \frac{\Lambda}{2} & -t\gamma(\vec{k}) \\ 0 & 0 & -t\gamma^*(\vec{k}) & \frac{\Lambda}{2} \end{pmatrix}. \qquad (3.54)$$

The energy bands of this Hamiltonian are given by $\pm\varepsilon_{1,2}$ where

$$\varepsilon_{1,2} = \sqrt{t^2|\gamma(\vec{k})|^2 + \frac{t_\perp^2}{2} + \left(\frac{\Lambda}{2}\right)^2 \pm 2\sqrt{t^2|\gamma(\vec{k})|^2\left(\Lambda^2 + t_\perp^2\right) + \left(\frac{t_\perp}{2}\right)^4}}. \qquad (3.55)$$

Thus, the changing of the bias voltage opens the band gap Λ between central energy bands ($\pm E_2$). The energy bands are plotted over entire Brillouin zone for $t = t_\perp$ and $\Lambda = 0.2t_\perp$ in Fig. 3.5.

Mass term

The mass term m makes the difference between the A and B sublattices. The Hamiltonian reads

$$\mathcal{H}_{\vec{k}} = \begin{pmatrix} m & -t\gamma(\vec{k}) & 0 & 0 \\ -t\gamma^*(\vec{k}) & -m & t_\perp & 0 \\ 0 & t_\perp & m & -t\gamma(\vec{k}) \\ 0 & 0 & -t\gamma^*(\vec{k}) & -m \end{pmatrix}. \qquad (3.56)$$

The eigenenergies of the Hamiltonian Eq.(3.56) are given by $\pm\bar{\varepsilon}_{1,2}$ where

$$\bar{\varepsilon}_{1,2} = \sqrt{\left(\frac{1}{2}t_\perp \pm \sqrt{t^2|\gamma(\vec{k})|^2 + \frac{1}{4}t_\perp^2}\right)^2 + m^2}. \qquad (3.57)$$

. The energy difference between two central bands ($\pm\bar{\varepsilon}_2$) is $2m$.

In Fig.(3.6), we plot these eigenergies throughout Brillouin zone for $t = t_\perp$ and $m = 0.1t_\perp$.

3.3.2 *Entanglement spectrum*

Bias voltage

Tracing out one layer 1 of ground state of bilayer graphene in the presence of the bias voltage leads to the correlation matrix

$$C(\vec{k}) = \begin{pmatrix} C_{11} & C_{12} \\ C_{12}^* & C_{22} \end{pmatrix} \qquad (3.58)$$

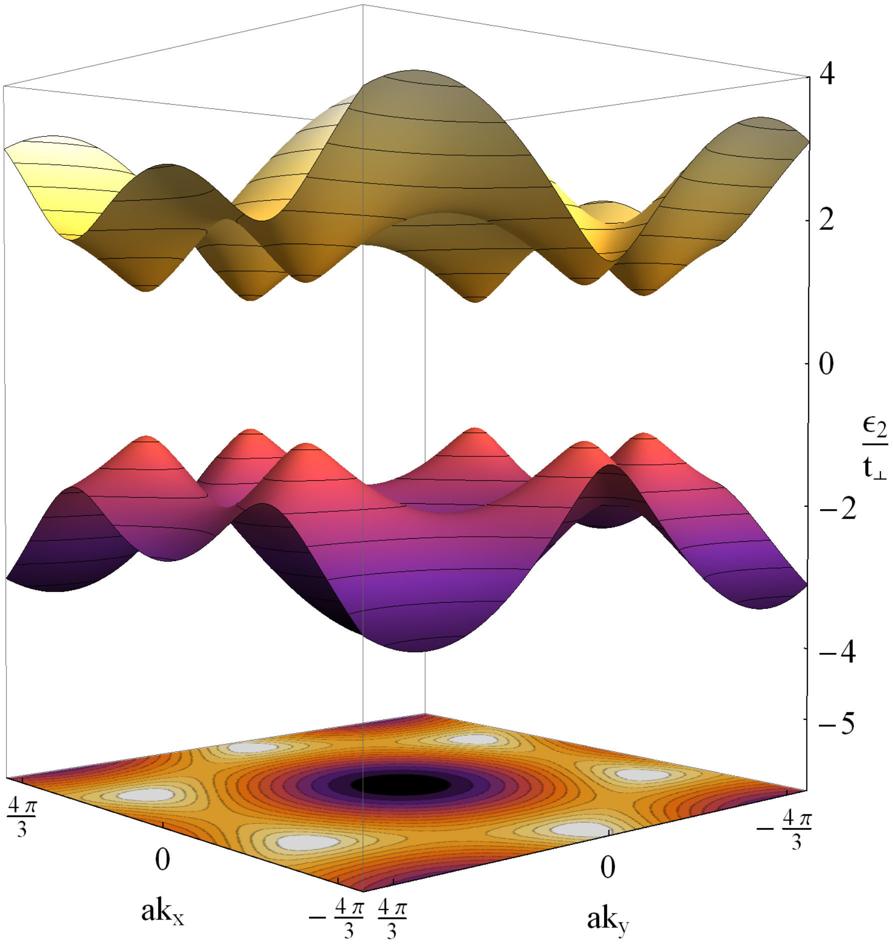

Figure 3.5: The central energy bands $\pm\varepsilon_2$ plotted over entire Brillouin zone for $t = t_\perp$ and $\Lambda = 0.2t_\perp$. The contour plot represents the energy band (ε_2).

where

$$C_{11}(\vec{k}) = \langle a^\dagger_{2\vec{k}} a_{2\vec{k}} \rangle$$

$$= \frac{1}{2} - \frac{1}{4}\left(1 - \frac{\frac{1}{2}t_\perp^2}{\sqrt{t^2|\gamma(\vec{k})|^2(t_\perp^2 + \Lambda^2) + \frac{1}{4}t_\perp^4}}\right)\frac{\Lambda}{\sqrt{\Lambda^2 + t_\perp^2}}\frac{1}{\varepsilon_2}\left(e_2 - \frac{t_1^2}{\sqrt{\Lambda^2 + t_\perp^2}}\right)$$

$$+ \frac{1}{4}\left(1 + \frac{\frac{1}{2}t_\perp^2}{\sqrt{t^2|\gamma(\vec{k})|^2(t_\perp^2 + \Lambda^2) + \frac{1}{4}t_\perp^4}}\right)\frac{\Lambda}{\sqrt{\Lambda^2 + t_\perp^2}}\frac{1}{\varepsilon_1}\left(e_1 - \frac{t_1^2}{\sqrt{\Lambda^2 + t_\perp^2}}\right)$$

$$C_{22} = \langle b^\dagger_{2\vec{k}} b_{2\vec{k}} \rangle$$

$$= \frac{1}{2} - \frac{1}{4}\left(1 + \frac{\frac{1}{2}t_\perp^2}{\sqrt{t^2|\gamma(\vec{k})|^2(t_\perp^2 + \Lambda^2) + \frac{1}{4}t_\perp^4}}\right)\frac{\Lambda}{\sqrt{\Lambda^2 + t_\perp^2}}\frac{1}{\varepsilon_2}\left(e_2 + \frac{t_1^2}{\sqrt{\Lambda^2 + t_\perp^2}}\right)$$

$$+ \frac{1}{4}\left(1 - \frac{\frac{1}{2}t_\perp^2}{\sqrt{t^2|\gamma(\vec{k})|^2(t_\perp^2 + \Lambda^2) + \frac{1}{4}t_\perp^4}}\right)\frac{\Lambda}{\sqrt{\Lambda^2 + t_\perp^2}}\frac{1}{\varepsilon_1}\left(e_1 + \frac{t_1^2}{\sqrt{\Lambda^2 + t_\perp^2}}\right)$$

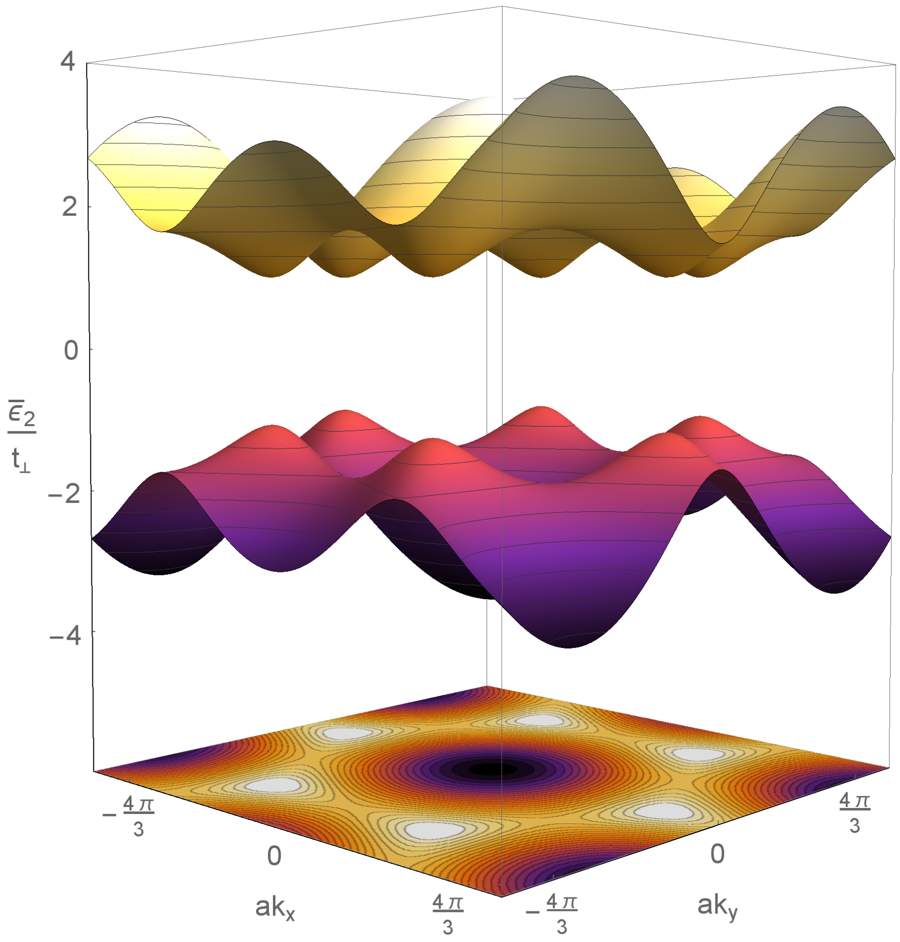

Figure 3.6: The central energy bands $\pm\bar{\varepsilon}_2$ plotted over entire Brillouin zone for $t = t_\perp$ and $m = 0.1t_\perp$. The contour plot represents the energy band $(\bar{\varepsilon}_2)$.

$$
\begin{aligned}
C_{12} &= \langle a^\dagger_{2\vec{k}} b_{2\vec{k}} \rangle \\
&= \frac{1}{2} \mathrm{e}^{i\phi(\vec{k})} \frac{t|\gamma(\vec{k})|}{\sqrt{t^2|\gamma(\vec{k})|^2 + \frac{1}{4}\frac{t_\perp^4}{t_\perp^2+\Lambda^2}}} \left(\frac{e_1}{\varepsilon_1} - \frac{e_2}{\varepsilon_2} \right)
\end{aligned}
\tag{3.59}
$$

with

$$
e_{1,2} = \frac{1}{2}\left(\sqrt{\Lambda^2 + t_\perp^2} \pm \sqrt{4t^2|\gamma(\vec{k})|^2 + \frac{t_\perp^4}{t_\perp^2 + \Lambda^2}} \right) \tag{3.60}
$$

The entanglement levels analytically obtained from this correlation matrix will be discussed later in 3.3.2.

Mass term

The correlation matrix of ground state of graphene bilayers in the presence of the mass term m given by tracing out one layer 1 reads

$$C(\vec{k}) = \begin{pmatrix} C_{11} & C_{12} \\ C_{12}^{*} & C_{22} \end{pmatrix} \tag{3.61}$$

where

$$\begin{aligned} C_{11}(\vec{k}) &= \langle a^{\dagger}_{2\vec{k}} a_{2\vec{k}} \rangle \\ &= \frac{1}{2} - \frac{1}{4}\left(1 - \frac{\frac{1}{2}t_{\perp}}{\sqrt{t^2|\gamma(\vec{k})|^2 + \frac{1}{4}t_{\perp}^2}}\right)\frac{m}{\overline{\varepsilon}_2} + \left(1 + \frac{\frac{1}{2}t_{\perp}}{\sqrt{t^2|\gamma(\vec{k})|^2 + \frac{1}{4}t_{\perp}^2}}\right)\frac{m}{\overline{\varepsilon}_1} \\ C_{22}(\vec{k}) &= \langle b^{\dagger}_{2\vec{k}} b_{2\vec{k}} \rangle \\ &= \frac{1}{2} + \frac{1}{4}\left(1 + \frac{\frac{1}{2}t_{\perp}}{\sqrt{t^2|\gamma(\vec{k})|^2 + \frac{1}{4}t_{\perp}^2}}\right)\frac{m}{\overline{\varepsilon}_2} + \left(1 - \frac{\frac{1}{2}t_{\perp}}{\sqrt{t^2|\gamma(\vec{k})|^2 + \frac{1}{4}t_{\perp}^2}}\right)\frac{m}{\overline{\varepsilon}_1} \\ C_{12}(\vec{k}) &= \langle a^{\dagger}_{2\vec{k}} b_{2\vec{k}} \rangle \\ &= \frac{1}{2}\mathrm{e}^{i\phi(\vec{k})}\frac{t|\gamma(\vec{k})|}{\sqrt{t^2|\gamma(\vec{k})|^2 + \frac{1}{4}t_{\perp}^2}}\left(\frac{\overline{e}_1}{\overline{\varepsilon}_1} - \frac{\overline{e}_2}{\overline{\varepsilon}_2}\right) \end{aligned} \tag{3.62}$$

with

$$\overline{e}_{1,2} = \frac{1}{2}t_{\perp} \pm \sqrt{t^2|\gamma(\vec{k})|^2 + \frac{1}{4}t_{\perp}^2}. \tag{3.63}$$

Analytical results

The entanglement levels obtained from the correlation matrices Eq.(3.58) and Eq.(3.61) have the following form

$$\xi_{\pm} = -2\mathrm{arctanh}\left(C_{11} + C_{22} - 1 \pm \sqrt{(C_{11} - C_{22})^2 + |C_{12}|^2}\right). \tag{3.64}$$

Our analytically obtained entanglement levels Eq.(3.64) are visualized in the Fig.(3.7) of graphene bilayers in the presence of the bias voltage along the axis k_x for $t/t_{\perp} = 1$ and $U/t_{\perp} = 0.2$. Meanwhile, the entanglement levels of graphene bilayers in the presence of mass term are represented in Fig. (3.8) along the axis k_x.

When the bias voltage or mass term are included, the average occupancy number at site A, $C_{11}(\vec{k})$, and the average occupancy number at site B, $C_{22}(\vec{k})$ are not equal and differ from the 1/2. This leads to the remaining layer 2 not being half-filled obtained

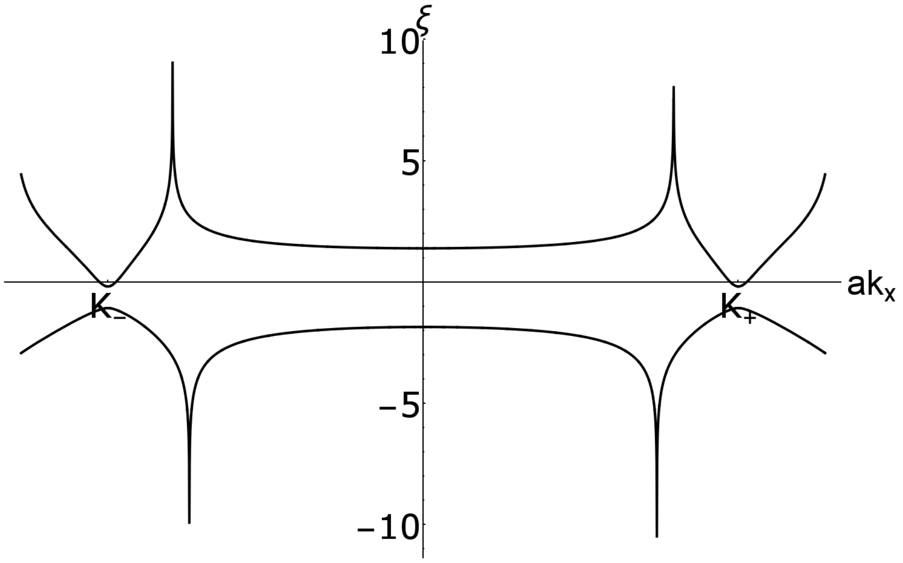

Figure 3.7: The central energy bands $\pm\varepsilon_2$ plotted over entire Brillouin zone along the k_x axis for $t = t_\perp$ and $\Lambda = 0.2t_\perp$.

from ground state of half-filed graphene bilayers, and the entanglement gap between entanglement levels is opened. In this context, there is no the relation of the entanglement spectrum of undoped graphene bilayers and the energy of doped graphene monolayer. All this is just a consequence of the hopping parameter $t_\perp$ couples A1 and B2 sites which have different sign.

3.4 CONCLUSION AND OUTLOOK

We have analytically derived the entanglement Hamiltonian of ground state of Bernal stacked graphene bilayers. When the entanglement Hamiltonian is obtained by tracing out one layer, there is a proportionality between it and the energetic Hamiltonian of the remaining monolayer of graphene in the limit of strong coupling layers. The proportionality factor represents the phenomenological inverse temperature, and there is an exact relation between this phenomenological scale and the inverse temperature. Furthermore, this relation leads to that the canonical Hamiltonian being independent of temperature.

The proportionality between the entanglement Hamiltonian of graphene bilayers and the energetic Hamiltonian of monolayer graphene also leads to the equivalence of their topological quantities. In this case, this is the Berry phase contribution to the Chern number.

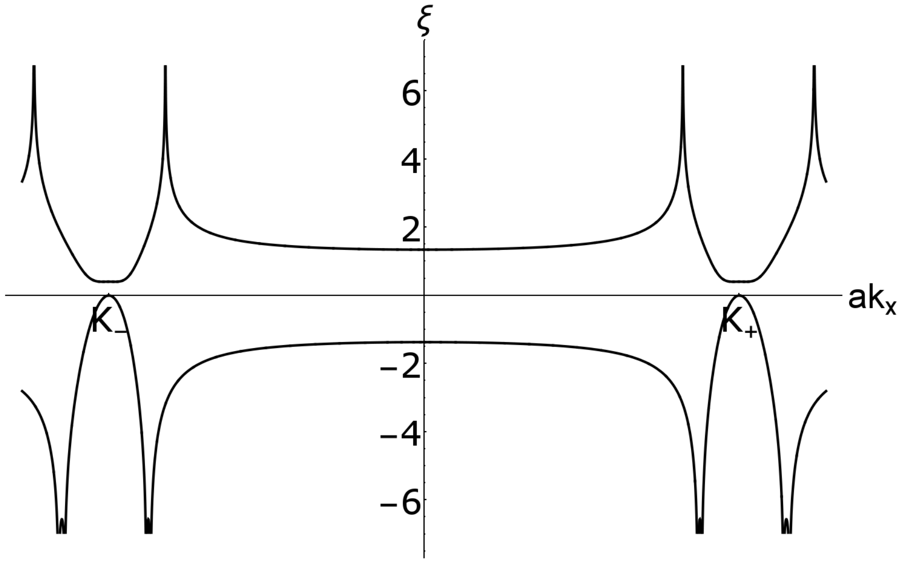

Figure 3.8: The entanglement spectrum of graphene bilayers in the presence the mass term plotted along the k_x axis for $t/t_\perp = 1$ and $m/t_\perp = 0.1$.

In the presence of the on-site energy or the mass term, the remaining layer is doped which is obtained by tracing other layer from ground state of undoped graphene bilayers. In such a way, there is no relation between the entanglement Hamiltonian of graphene bilayers and the energetic Hamiltonian of graphene monolayer.

The relation between the phenomenological inverse temperature and the inverse thermodynamic temperature given by Eq.(3.43), depends on the lattice geometry, Ref. [Schliemann, 2013]. Thus, one possible extension of this is to consider other lattice geometry.

4

TRIGONAL WARPING IN BILAYER GRAPHENE: ENERGY VERSUS ENTANGLEMENT SPECTRUM

Most of the work presented in this chapter has been published to the Physical Review Journal B.
Sonja Predin, Paul Wenk and John Schliemann, Trigonal Warping in Bilayer Graphene: Energy versus Entanglement Spectrum, Phys. Rev. B ***93****, 115106, (2016).* [Predin et al., 2016]

In the previous Chapter 3, we have shown that upon tracing out one layer, the entanglement Hamiltonian of ground state of free fermions in graphene bilayers arranged in Bernal stacking is proportional to the energetic Hamiltonian of graphene monolayer in the strong coupling limit. However, this does not hold in general even in the strong coupling limit what is illustrated by counterexamples in Ref. [Lundgren et al., 2012] where a spin ladders of clearly nonidentical legs were considered and in Ref. [Schliemann and Läuchli, 2012] where the anisotropic spin ladders of the arbitrary spin length were considered, while then even the unperturbed non-degenerate ground state has a nontrivial entanglement spectrum. In this Chapter we provide another counter example given by graphene bilayers in the presence of trigonal warping [McCann and Koshino, 2013,Rozhkov et al., 2016]. As we shall see in the following, the geometric properties of the entanglement spectrum of an undoped graphene bilayer and the energy spectrum of a monolayer clearly differ qualitatively. However, certain topological quantities such as Berry phase type contributions to Chern numbers agree. After we had made our work available as an arXiv preprint and submitted to the journal, we became aware of a little bit earlier study Ref. [Fukui and Hatsugai, 2014], where also Chern numbers calculated from the eigenstates of entanglement Hamiltonians are studied.

This Chapter is organized as follows. In Section 4.1 we discuss the full eigensystem of the tight-binding model of bilayer graphene in the presence of trigonal warping. To enable analytical progress we neglect here terms breaking particle-hole symmetry. On the other hand, our calculation considers the entire first Brillouin zone and avoids the Dirac cone approximation usually employed in studies of trigonal warping in graphene bilayers [McCann and Fal'ko, 2006, Nilsson et al., 2006, Koshino and Ando, 2006, Kechedzhi et al., 2007, Manes et al., 2007, Cserti et al., 2007, Mikitik and Sharlai, 2008, Mariani et al., 2012, Cosma and Fal'ko, 2015]. We compare our results for the full four-band model with an effective Hamiltonian acting on the two central bands [McCann and Fal'ko, 2006, Mariani et al., 2012, Cosma and Fal'ko, 2015]. The entanglement spectrum obtained from the ground state of undoped graphene bilayers is analyzed in Section 4.2. We discuss the case of one layer being traced out as well as the situation where the trace is performed over two other out of four sublattices. In Section 4.3 we will show that discontinuities of wave vector in eigenvectors of the Hamiltonian are reflected on the entanglement Hamiltonian and have a large influence on the geometric and topological properties of the entanglement Hamiltonian. We close with a conclusion and an outlook in Section 4.4.

4.1 ENERGY SPECTRUM OF GRAPHENE BILAYERS: TRIGONAL WARPING AND TOPOLOGICAL INVARIANTS

The standard tight-binding Hamiltonian for graphene bilayers in Bernal stacking can be formulated as [McCann and Koshino, 2013, Rozhkov et al., 2016]

$$\begin{aligned} H = & -t\sum_{\vec{k}}\left(\gamma(\vec{k})a^{\dagger}_{1\vec{k}}b_{1\vec{k}}+\gamma(\vec{k})a^{\dagger}_{2\vec{k}}b_{2\vec{k}}+\mathrm{h.}c.\right) \\ & +t_{\perp}\sum_{\vec{k}}\left(b^{\dagger}_{1\vec{k}}a_{2\vec{k}}+a^{\dagger}_{2\vec{k}}b_{1\vec{k}}\right) \\ & -t_3\sum_{\vec{k}}\left(\gamma(\vec{k})b^{\dagger}_{2\vec{k}}a_{1\vec{k}}+\gamma^{*}(\vec{k})a^{\dagger}_{1\vec{k}}b_{2\vec{k}}\right) \\ & +t_4\sum_{\vec{k}}\left(\gamma(\vec{k})\left(a^{\dagger}_{1\vec{k}}a_{2\vec{k}}+b^{\dagger}_{1\vec{k}}b_{2\vec{k}}\right)+\mathrm{h.}c.\right)\,, \end{aligned} \tag{4.1}$$

where $a^{\dagger}_{i\vec{k}}$ $(a_{i\vec{k}})$ and $b^{\dagger}_{i\vec{k}}$ $(b_{i\vec{k}})$ create (annihilate) electrons with wave vector $\vec{k}$ in layers $i = 1, 2$ on sublattice A and B, respectively. Moreover, $\gamma(\vec{k}) = \sum_{l=1}^{3}\exp(i\vec{k}\cdot\vec{\delta}_l)$ where the $\vec{\delta}_l$ are the vectors connecting a given carbon atom with its nearest neighbors on the

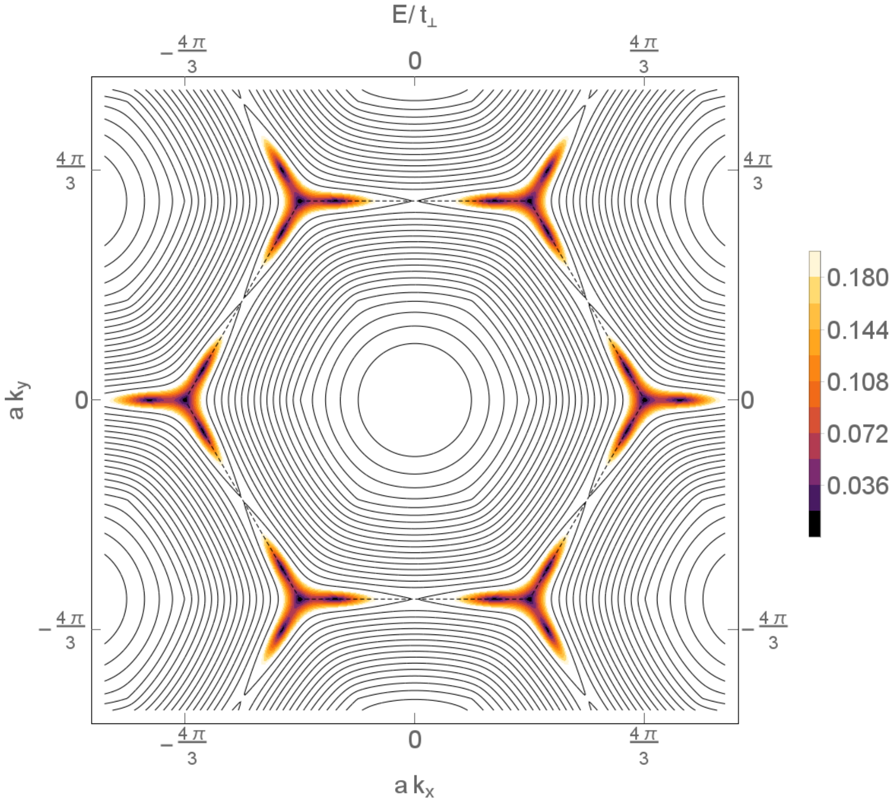

Figure 4.1: Contour plot of the energy band $(+E_2(\vec{k}))$ plotted for $t_\perp = t$, $t_3 = 0.5t$. The contour of the colored region indicates $E = 0.2/t_\perp$. The edge of the first Brillouin zone is marked by dashed lines.

other sublattice in a graphene monolayer defined by Eq(2.5). The hopping parameters $t, t_\perp, t_3, t_4$ are plotted at Fig(3.1).

The presence of all four couplings in the Hamiltonian Eq. (4.1) makes its explicit diagonalization in terms of analytical expressions a particularly cumbersome task. As the present study chiefly relies on analytical calculations rather than resorts to numerics, we will drop the contributions proportional to the smallest parameter t_4 in order to achieve an analytically manageable situation.

Putting $t_4 = 0$ the full eigensystem of the Hamiltonian (4.1) can be obtained in a closed analytical fashion as detailed in appendix A. The four dispersion branches $(\pm E_1(\vec{k}))$, $(\pm E_2(\vec{k}))$ form a symmetric spectrum with

$$E_{1/2}(\vec{k}) = \left[\frac{1}{2}\left(t_\perp^2 + t_3^2|\gamma(\vec{k})|^2 + 2t^2|\gamma(\vec{k})|^2\right)\right.$$
$$\left.\pm\frac{1}{2}\sqrt{4t^2|\gamma(\vec{k})|^2\left(t_\perp^2 + t_3^2|\gamma(\vec{k})|^2 - 2t_\perp t_3|\gamma(\vec{k})|\cos\left(3\phi_{\vec{k}}\right)\right) + \left(t_\perp^2 - t_3^2|\gamma(\vec{k})|^2\right)^2}\right]^{1/2} \tag{4.2}$$

and $\gamma(\vec{k}) = |\gamma(\vec{k})|e^{i\phi_{\vec{k}}}$. The two outer branches ($\pm E_1(\vec{k})$) are separated from the inner ones ($\pm E_2(\vec{k})$) by gaps determined essentially by the hopping parameter $t_\perp$. The result Eq. (4.2) generalizes the energy spectrum given in Ref. [McCann and Fal'ko, 2006] within the Dirac cone approximation to the full Brillouin zone. Moreover, in appendix A we also give the complete data of the corresponding eigenvectors. Fig. 4.2 concentrates on the vicinity of a given K-point using realistic parameters.

The inner branches ($\pm E_2(\vec{k})$) dominate the low-energy physics of the system near half filling and meet at zero energy for

$$\gamma(\vec{k}) = 0 \tag{4.3}$$

corresponding to the two inequivalent corners $K_\pm$ of the first Brillouin zone, and for

$$\cos\left(3\phi_{\vec{k}}\right) = -1 \quad \wedge \quad |\gamma(\vec{k})| = \frac{t_\perp t_3}{t^2}\,. \tag{4.4}$$

The latter condition defines three additional satellite Dirac cones around each K-point two of which lying on the edges (faces) of the Brillouin zone connecting $K_\pm$. The third satellite Dirac cone lies formally outside the Brillouin zone but is equivalent to a satellite cone on the edge around an equivalent K-point. Indeed, the quantity $\gamma(\vec{k})$ has a constant phase $\phi_{\vec{k}} \in \{-\pi/3, \pi/3, \pi\}$ on each face: As an example, consider the edge connecting the two inequivalent K-points given by $\vec{K}_\pm = \frac{2\pi}{\sqrt{3}a}\left(\pm\frac{1}{\sqrt{3}}, 1\right)$ where one finds

$$\gamma\left(k_x, \frac{2\pi}{\sqrt{3}a}\right) = e^{-i\pi/3}\left(2\cos\left(\frac{a}{2}k_x\right) - 1\right) \tag{4.5}$$

with the parenthesis being nonnegative for k_x ranging between $(\pm 2\pi/(3a))$. Thus, solving for k_x the satellite Dirac cones on that edge lie at

$$\vec{k} = \left(\pm\frac{2}{a}\arccos\left(\frac{1}{2}\left(1 + \frac{t_\perp t_3}{t^2}\right)\right), \frac{2\pi}{\sqrt{3}a}\right), \tag{4.6}$$

and the other satellite cones are located at positions being equivalent under reciprocal lattice translation and/or hexagonal rotation. Note that for $t_\perp t_3/t^2 = 1$ the satellite cones merge in the M-points (centers of the faces) and they vanish for even larger values of that ratio. In Fig. 4.1 we give a sketch of the situation in the entire Brillouin zone for moderate values of $t_\perp$ and t_3. As

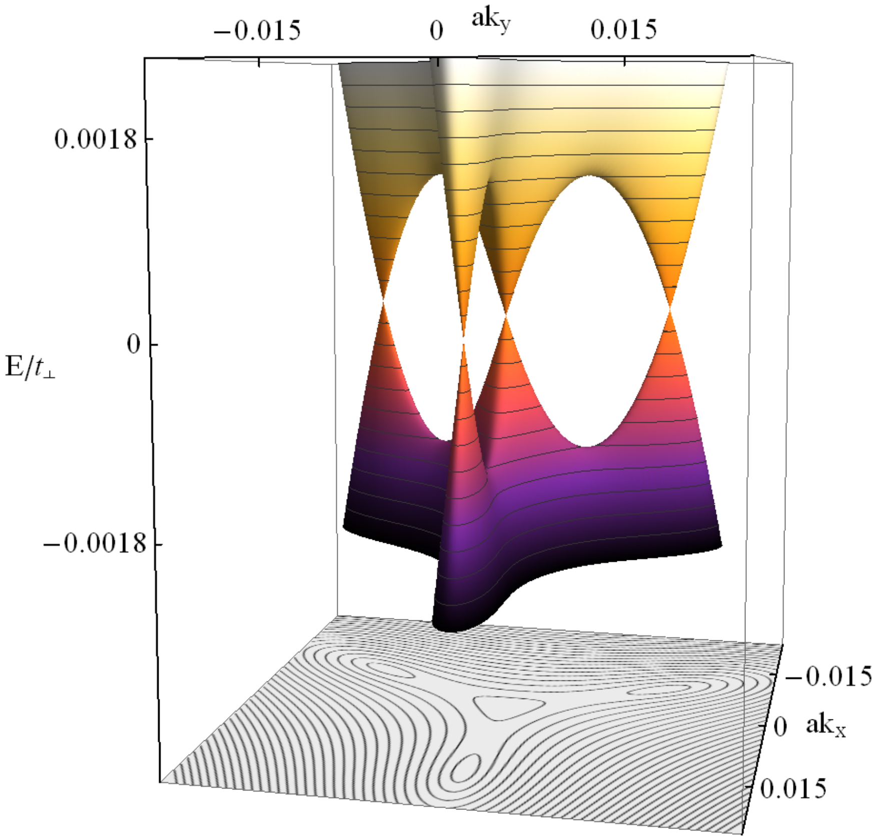

Figure 4.2: The central energy bands ($\pm E_2(\vec{k})$) plotted around a given K-point for $t_\perp = 0.1t$, $t_3 = 0.15t$. The dispersions show a central Dirac cone accompanied by three satellites. The components of the wave vector are measured relatively to the K-point.

we have already seen in Chapter 3, for $t_3 = 0$ the two energy bands ($\pm E_2(\vec{k})$) touch only at the K-points where they have a quadratic dispersion. Finite $t_3 \neq 0$ causes a splitting into in total four Dirac cones with linear dispersion, an effect known as trigonal warping [McCann and Koshino, 2013,Mariani et al., 2012].

As a further important property, the eigenvectors corresponding to ($\pm E_2(\vec{k})$) are discontinuous as a function of wave vector at the degeneracy points defined by Eq. (4.4); for more technical details we refer to chapter 4.3. As a simplistic toy model mimicking such an effect one can consider the Hamiltonian $H = -k\sigma^z$ with a one-dimensional wave number k and the Pauli matrix σ^z describing some internal degree of freedom: In the many-body ground state of zero Fermi energy all occupied states with $k > 0$ have spin up while for all states with $k < 0$ the spin points downwards, resulting in a discontinuity of the occupied eigenvectors at $k = 0$. As we shall see below, in the present case of graphene bilayers this discontinuity is also reflected in the entanglement spectrum.

An effective Hamiltonian in the presence of the trigonal warping providing an approximate description of the central bands $(\pm E_2(\vec{k}))$ can be given following Ref. [McCann and Fal'ko, 2006]. In up to linear order in $1/t_\perp$ one finds

$$H = -\begin{pmatrix} 0 & \frac{t^2}{t_\perp}\left(\gamma^*(\vec{k})\right)^2 + t_3\gamma(\vec{k}) \\ \frac{t^2}{t_\perp}\left(\gamma(\vec{k})\right)^2 + t_3\gamma^*(\vec{k}) & 0 \end{pmatrix} \tag{4.7}$$

with respect to the basis $\left(b^\dagger_{2\vec{k}}, a^\dagger_{1\vec{k}}\right)|0\rangle$. The eigenstates read

$$|\chi_\pm\rangle = \frac{1}{\sqrt{2}}\begin{pmatrix} 1 \\ \mp e^{i\psi_{\vec{k}}} \end{pmatrix} \tag{4.8}$$

with

$$e^{i\psi_{\vec{k}}} = \frac{\frac{t^2}{t_\perp}\left(\gamma(\vec{k})\right)^2 + t_3\gamma^*(\vec{k})}{\left|\frac{t^2}{t_\perp}\left(\gamma(\vec{k})\right)^2 + t_3\gamma^*(\vec{k})\right|}\,. \tag{4.9}$$

Note that the Hamiltonian (4.7) vanishes if and only if the conditions (4.3) or (4.4) are fulfilled implying that the positions of the central and satellite Dirac cones are the same as for the full Hamiltonian (4.1). Moreover , $\psi_{\vec{k}}$ is a smooth and well-defined function of the wave vector except for the locations of Dirac cones. Accordingly, the Berry curvature

$$F(\vec{k}) = \frac{\partial A_y}{\partial k_x} - \frac{\partial A_x}{\partial k_y} \tag{4.10}$$

arising from the Berry connection

$$\vec{A}(\vec{k}) = i\langle\chi_\pm(\vec{k})|\frac{\partial}{\partial\vec{k}}|\chi_\pm(\vec{k})\rangle = -\frac{1}{2}\frac{\partial\psi_{\vec{k}}}{\partial\vec{k}} \tag{4.11}$$

vanishes everywhere outside the Dirac cones where contributions in terms of δ-functions arise. Integrating the Berry connection along closed path in $\vec{k}$-space leads to geometrical quantities often referred to as Berry phases, although no contact to adiabaticity is made here. Moreover, if the Berry curvature has only nonzero contributions in terms of δ-functions (as it is the case here and in the following) these geometrical phases are indeed topological, i.e. they are invariant under continuous variations of the paths as long as the support of the δ-functions is not touched.

As discussed in Refs. [Manes et al., 2007, Mikitik and Sharlai, 2008, Mariani et al., 2012], integrating along a closed path around the central Dirac cones at $K_\pm$ yields a Berry phase of $(\mp\pi)$, while each of the accompanying satellite cones gives a contribution of $(\pm\pi)$. Thus, the total Berry phase arising at and around each K-point is, as in the absence of trigonal warping, $(\pm 2\pi)$, and the integral over the whole Brillouin zone of the Berry connection (i.e. the Chern number) vanishes. Naturally, our present analysis going beyond the Dirac cone approximation confirms these results.

4.2 ENTANGLEMENT SPECTRA

Here we analytically derive the entanglement Hamiltonian of free fermions on bilayer honeycomb lattice in the presence of trigonal warping by using the method described in Chapter 3. In particular, we formulate the entanglement Hamiltonian for systems of free fermions as a single-particle operator [Peschel, 2003, Cheong and Henley, 2004, Schliemann, 2013].

4.2.1 *Tracing out one layer*

We now consider the ground state of the undoped graphene bilayer such that all states with negative energies $(-E_1(\vec{k}))$, $(-E_2(\vec{k}))$ are occupied while all others are empty. Tracing out layer 1 leads to the correlation matrix

$$C(\vec{k}) = \begin{pmatrix} \frac{1}{2} & u(\vec{k}) \\ u^*(\vec{k}) & \frac{1}{2} \end{pmatrix} \tag{4.12}$$

where an explicit expression for $u(\vec{k})$ is given in appendix B. The entanglement levels corresponding to the eigenvalues $\eta_\pm(\vec{k}) = 1/2 \mp |u(\vec{k})|$ are

$$\xi_\pm(\vec{k}) = \pm\, 2\,\mathrm{artanh}\left(2|u(\vec{k})|\right) . \tag{4.13}$$

The modulus $|u|$ can be formulated as

$$|u| = \frac{1/2}{\sqrt{1+(d/(t|\gamma(\vec{k})|))^2}}\sqrt{\frac{1}{2}\left(1-\frac{\epsilon_1\epsilon_2+b^2}{E_1E_2}\right)} \tag{4.14}$$

with (cf. Eqs. (A.14),(A.15))

$$d \;=\; \frac{\left(t_\perp^2 - t_3^2|\gamma(\vec{k})|^2\right)/2}{\sqrt{t_\perp^2 + t_3^2|\gamma(\vec{k})|^2 - 2t_\perp t_3|\gamma(\vec{k})|\cos\left(3\phi_{\vec{k}}\right)}}\,, \tag{4.15}$$

$$b = \frac{t_\perp t_3 |\gamma(\vec{k})| |\sin\left(3\phi_{\vec{k}}\right)|}{\sqrt{t_\perp^2 + t_3^2|\gamma(\vec{k})|^2 - 2t_\perp t_3|\gamma(\vec{k})|\cos\left(3\phi_{\vec{k}}\right)}}, \tag{4.16}$$

and (cf. Eq. (A.21))

$$\begin{aligned}\epsilon_{1,2} &= t|\gamma(\vec{k})| \\ &\pm\sqrt{\left(t_\perp^2 + t_3^2|\gamma(\vec{k})|^2 - 2t_\perp t_3|\gamma(\vec{k})|\cos\left(3\phi_{\vec{k}}\right)\right)^2/4 + d^2}\end{aligned} \tag{4.17}$$

implying

$$E_{1,2} = \sqrt{\epsilon_{1,2}^2 + b^2}\,. \tag{4.18}$$

The r.h.s of Eq. (4.14) becomes zero if the radicand vanishes. According to the discussion in Section 4.3 and Appendix B this is the case when $\cos\left(3\phi_{\vec{k}}\right) = -1$ leading to $b = 0$ and $E_1 = \epsilon_1 \geq 0$, $E_2 = |\epsilon_2|$ such that

$$|u| \propto \sqrt{\frac{1}{2}\left(1 - \frac{\epsilon_2}{|\epsilon_2|}\right)} \tag{4.19}$$

Now equation (4.27) shows that $|u(\vec{k})| = 0$ is equivalent to

$$\cos\left(3\phi_{\vec{k}}\right) = -1 \quad \wedge \quad |\gamma(\vec{k})| \in \left[0, t_\perp t_3/t^2\right], \tag{4.20}$$

where the endpoint of the above interval defines according to condition (4.4) the location of the satellite Dirac cones. As a result, the entanglement levels (4.13) vanish along segments of the faces of the first Brillouin zone bounded by the positions of the central Dirac cones and their satellites. At the satellite Dirac cones the entanglement spectrum is discontinuous as a function of wave vector. In Fig. 4.3 we plotted the entanglement spectrum $\xi_+(\vec{k})$ for the whole Brillouin zone. For a better visualization large hopping parameters have been chosen. The contour of the colored region connects all three satellite Dirac cones. As discussed in chapter 4.3, this discontinuity is inherited from a discontinuity in the eigenvectors of the occupied single-particle states. The entanglement spectrum in the entire Brillouin zone is illustrated in Fig. 4.3, whereas Fig. 4.4 focuses on a given K-point.

Moreover, apart from the eigenvalues of the entanglement Hamiltonian, let us also consider its eigenvector which coincide with the eigenvectors of the correlation matrix (D.8). As discussed in appendix B, the complex function $u(\vec{k})$ entering the correlation matrix becomes singular at the K-points and the positions of the accompanying satellite Dirac cones of the energy spectrum,

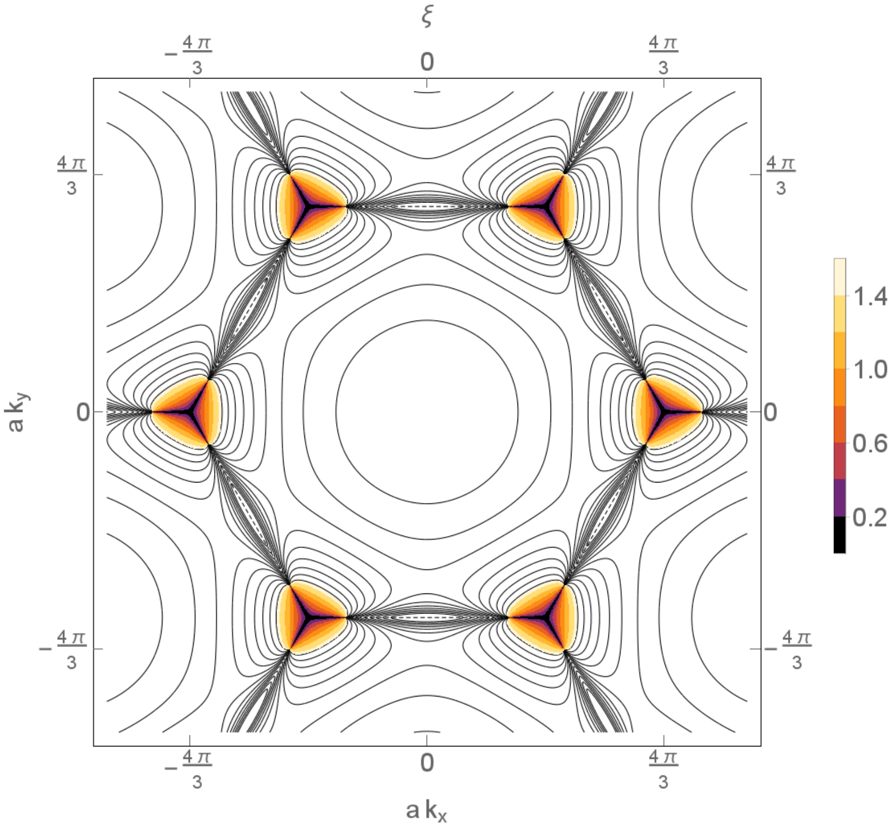

Figure 4.3: Contour plot of the entanglement spectrum $\xi_+(\vec{k})$ plotted for $t_\perp = t$, $t_3 = 0.5t$. The contour of the colored region indicates $\xi = 1.5$. The dashed line delineates the first Brillouin zone.

leading again to δ-function-type contributions to the Berry curvature which vanishes otherwise. Combining symbolic computer algebra techniques and numerical calculations we find here a Berry phase of $(\mp\pi/2)$ around the corners $K_\pm$ of the Brillouin zone, and $(\pm\pi/2)$ for the corresponding satellite positions. For the central positions the above calculations can also be done fully analytically by expanding the eigensystem data around $K_\pm$. For the satellite locations such an expansion is not possible due to the discontinuity of the eigenvectors.

Thus, the total Berry phase contribution from each K-point $K_\pm$ is $(\pm\pi)$ and agrees with the Berry phase around the Dirac cones in monolayer graphene. As a result, although the entanglement spectrum of graphene bilayers generated by tracing out one layer shows obvious differences to the energy spectrum of monolayer graphene regarding qualitative geometrical properties, the topological Berry phases obtained from the corresponding eigenvectors still coincide at each K-point.

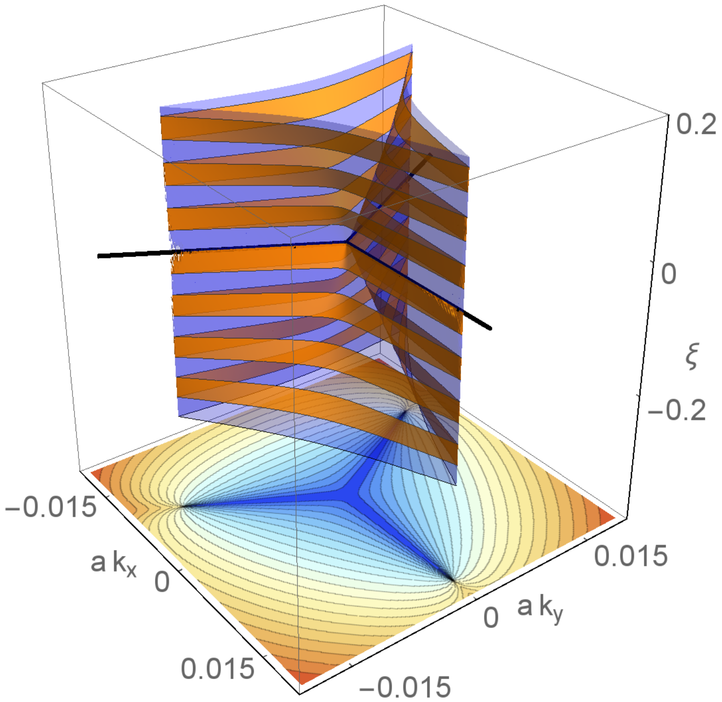

Figure 4.4: The entanglement spectrum (4.13) plotted around a given K-point for the same parameters as in Fig. 4.2. The density plot shows the upper entanglement level. Zero eigenvalues of the entanglement Hamiltonian occur along lines connecting the K-point with the locations of satellite Dirac cones of the energy spectrum (thick black lines). The components of the wave vector are measured relatively to the K-point.

4.2.2 *Tracing out other sublattices*

Now, we will consider the entanglement spectrum obtained by tracing out sublattices A1 and B2 (or A2 and B1) lying in different layers. In the former case one finds

$$C(\vec{k}) = \begin{pmatrix} \frac{1}{2} & v(\vec{k}) \\ v^*(\vec{k}) & \frac{1}{2} \end{pmatrix} \tag{4.21}$$

where an explicit expression for $v(\vec{k})$ is given in appendix B. The above correlation matrix has eigenvalues $\eta_\pm(\vec{k}) = 1/2 \mp |v(\vec{k})|$ leading to the entanglement levels

$$\xi_\pm(\vec{k}) = \pm 2 \operatorname{artanh}\left(2|v(\vec{k})|\right) . \tag{4.22}$$

In Fig. 4.5 we plotted the eigenvalues $\eta_-(\vec{k}) = 1/2 + |v(\vec{k})|$ of the correlation matrix around a given K-point. The modulus $|v(\vec{k})|$ reads more explicitly

$$|v(\vec{k})| = \frac{1}{2}\sqrt{1 - \frac{t^2|\gamma(\vec{k})|^2}{t^2|\gamma(\vec{k})|^2 + d^2}\frac{1}{2}\left(1 - \frac{\epsilon_1\epsilon_2 + b^2}{E_1E_2}\right)} \tag{4.23}$$

$$= \frac{1}{2}\sqrt{1 - 4|u(\vec{k})|^2} \tag{4.24}$$

and has a similar structure as $|u(\vec{k})|$ given in Eq. (4.14). In particular, $|v(\vec{k})| = 1/2 \Leftrightarrow |u(\vec{k})| = 0$ if the conditions (4.20) are fulfilled. In this case $\eta_+ = 0$ and $\eta_- = 1$ indicating that the remaining subsystem is unentangled with the system traced out.

Regarding Berry phases generated from the eigenstates of the correlation matrix (4.21) we note that the off-diagonal element $v(\vec{k})$ nowhere vanishes. As a consequence the Berry curvature is zero throughout the Brillouin zone, which in turn holds for all Berry phases. The nonvanishing of $v(\vec{k})$ follows from the fact that $|v(\vec{k})| = 0$ would require $|u(\vec{k})| = 1/2$ such that the entanglement (4.13) would diverge which is, as seen in section 4.2.1, not the case.

Finally, the correlation matrix obtained by tracing over the sublattices A1, A2 (or B1, B2) is proportional to the unit matrix,

$$C(\vec{k}) = \begin{pmatrix} \frac{1}{2} & 0 \\ 0 & \frac{1}{2} \end{pmatrix}, \tag{4.25}$$

indicating that these sublattices are maximally entangled with the part traced out.

4.3 CONTINUITY PROPERTIES

The eigenvectors corresponding to the energy branches $(\pm E_2(\vec{k}))$ are discontinuous at wave vectors determined by the condition (4.4). This comes about as follows: The matrix elements $U_{2,n}(\vec{k})$, $U_{3,n}(\vec{k})$, $n \in \{1, 2, 3, 4\}$ contain the quantities $\gamma_\pm^{(2)}$ defined in Eqs. (C.25) whereas the $U_{1,n}(\vec{k})$, $U_{4,n}(\vec{k})$ corresponding to $(\pm E_1(\vec{k}))$ involve $\gamma_\pm^{(1)}$. Fixing now $\cos\left(\phi_{\vec{k}}\right) = -1$ we have $b = 0$ such that $E_1 = \epsilon_1 \geq 0$ and $E_2 = |\epsilon_2|$ such that $\gamma_\pm^{(1)}$ remain continuous while $\gamma_\pm^{(2)}$ become

$$\gamma_\pm^{(2)} = \sqrt{\frac{1}{2}\left(1 \pm \frac{\epsilon_2}{|\epsilon_2|}\right)}. \tag{4.26}$$

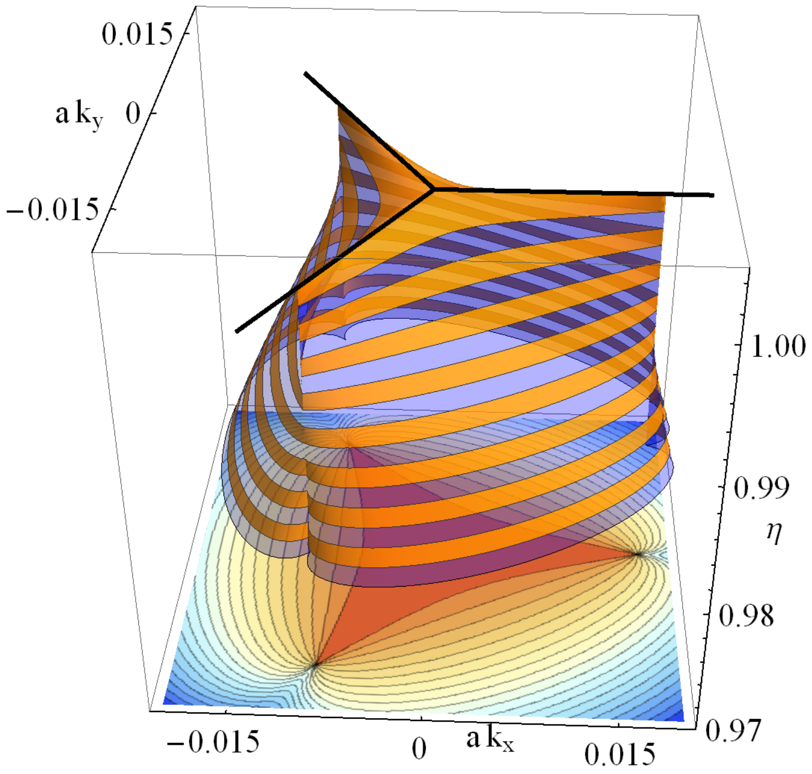

Figure 4.5: Eigenvalues $\eta_-(\vec{k}) = 1/2 + |v(\vec{k})|$ of the correlation matrix plotted around a given K-point for $t_\perp = 0.1t$, $t_3 = 0.15t$. The thick black lines correspond to the one in Fig. 4.4, and the components of the wave vector are again measured relatively to the K-point.

Inspection of Eq. (A.21) now shows that for $\cos\left(\phi_{\vec{k}}\right) = -1$

$$\epsilon_2(\vec{k}) \begin{cases} > 0 & |\gamma(\vec{k})| < t_\perp t_3/t^2 \\ < 0 & |\gamma(\vec{k})| > t_\perp t_3/t^2 \end{cases} \tag{4.27}$$

such that $\epsilon_2(\vec{k})$ changes sign for $|\gamma(\vec{k})| = t_\perp t_3/t^2$, i.e. $\gamma_\pm^{(2)}$ is discontinuous at wave vectors given by the condition (4.4). This discontinuity is inherited by the correlation matrix and, in turn, by the entanglement spectrum.

The technical reason for this discontinuity in the eigenvectors is of course the fact that the dispersions $(\pm E_2(\vec{k}))$ become degenerate at wave vectors fulfilling (4.4). In fact the eigenvectors can also be considered as continuous functions of the wave vector by appropriately relabeling the dispersion branches. In the ground state of the undoped bilayer system, however, only the lower branch $(-E_2(\vec{k}))$ is occupied, which makes the discontinuity unavoidable.

To circumvent this discontinuity one can open an energy gap between the upper and lower central band such that the corresponding eigenstates are necessarily continuous for all wave vectors. Among the various mechanisms producing such a gap only few allow for a still halfway convenient analytical treatment of the Hamiltonian. These include introducing identical mass terms in both layers, i.e. $H \mapsto H + H'$ with

$$H' = \operatorname{diag}\left(m, -m, -m, m\right) \ , \tag{4.28}$$

or applying a bias voltage Λ between the layers,

$$H' = \operatorname{diag}\left(-\Lambda/2, \Lambda/2, -\Lambda/2, \Lambda/2\right) \ . \tag{4.29}$$

In the former case the four dispersion branches $(\pm E_1(\vec{k}))$, $(\pm E_2(\vec{k}))$ are given by

$$\begin{aligned} E_{1/2}(\vec{k}) = &\Bigg[m^2 + \frac{1}{2}\left(t_\perp^2 + t_3^2|\gamma(\vec{k})|^2 + 2t^2|\gamma(\vec{k})|^2\right) \\ &\pm \frac{1}{2}\sqrt{4t^2|\gamma(\vec{k})|^2\left(t_\perp^2 + t_3^2|\gamma(\vec{k})|^2 - 2t_\perp t_3|\gamma(\vec{k})|\cos\left(3\phi_{\vec{k}}\right)\right) + \left(t_\perp^2 - t_3^2|\gamma(\vec{k})|^2\right)^2}\,\Bigg]^{1/2} \end{aligned} \tag{4.30}$$

while for a bias voltage one finds [McCann and Fal'ko, 2006]

$$\begin{aligned} E_{1/2}(\vec{k}) = &\Bigg[\frac{\Lambda^2}{4} + \frac{1}{2}\left(t_\perp^2 + t_3^2|\gamma(\vec{k})|^2 + 2t^2|\gamma(\vec{k})|^2\right) \\ &\pm \frac{1}{2}\sqrt{4t^2|\gamma(\vec{k})|^2\left(t_\perp^2 + t_3^2|\gamma(\vec{k})|^2 - 2t_\perp t_3|\gamma(\vec{k})|\cos\left(3\phi_{\vec{k}}\right) + \Lambda^2\right) + \left(t_\perp^2 - t_3^2|\gamma(\vec{k})|^2\right)^2}\,\Bigg]^{1/2} . \end{aligned} \tag{4.31}$$

In both cases the central energy bands $(\pm E_2(\vec{k}))$ are separated by a gap, and the spectrum can still be given in terms of comparably simple closed expressions since the characteristic polynomial of the 4×4 Hamiltonian matrix is a second-order polynomial in the energy squared leading to a spectrum being symmetric around zero. Also the corresponding eigenvectors can be obtained in closed analytical forms by procedures analogous to (but in detail somewhat more complicated than).

Note that applying a bias voltage as well as introducing a mass term in each layer discriminates the layers against each other. As we have shown in previous Chapter 3, the latter circumstance is due to the fact that $t_\perp$ couples sublattices in different layers for which the mass term has different sign.

4.4 CONCLUSION AND OUTLOOK

We have studied entanglement properties of the ground state of Bernal stacked graphene bilayers in the presence of trigonal warping. Our analysis includes both the eigenvalues of the reduced density matrix (giving rise to the entanglement spectrum) as well as its eigenvectors. When tracing out one layer, the entanglement spectrum shows qualitative geometric differences to the energy spectrum of a graphene monolayer while topological quantities such as Berry phase type contributions to Chern numbers agree. The latter finding is in contrast to the reduced density matrix resulting from tracing out other sublattices of the bilayer system. Here, all corresponding Berry phase integrals yield trivially zero. Thus, our study provides an example for common topological properties of the eigensystem of the energy Hamiltonian of a subsystem (here a graphene monolayer) and the entanglement Hamiltonian, while the geometrical shape of both spectra grossly differs. Our investigations are based on closed analytical expressions for the full eigensystem of bilayer graphene in the entire Brillouin zone with a trigonally warped spectrum.

Future work might address bilayer systems of other geometrical structures such as the Kagome lattice.

Furthermore, the graphene monolayer under a circularly polarized light exhibits ten different topological phases and high-Chern number behaviour is found in Ref. [Wang and Li, 2016]. The understanding of the topological phases of driven graphene bilayers under polarized light, especially in the presence of the trigonal warping in the energy and entanglement spectrum might be an extension of the present study. Moreover, the combination of influences of a static perpendicular magnetic field [Schliemann, 2013, Nemec and Cuniberti, 2007] and a circularly polarized light on the energy and entanglement spectrum of graphene bilayers could be an interesting research task.

5

ENTANGLEMENT SPECTRA OF SUPERCONDUCTIVITY GROUND STATES ON THE HONEYCOMB LATTICE

Most of the work presented in this chapter has been submitted to the European Physical Journal B.
Sonja Predin, and John Schliemann, Entanglement spectra of superconductivity ground states on the honeycomb lattice, preprint (submitted to the European Physical Journal B), arxiv:1611.01039.
[Predin and Schliemann, 2016]

Soon after the birth of graphene has begun the searching for its complex electronic phases and phase transitions, such as superconductivity or exciton condensation [Sorella and Tosatti, 1992, Khveshchenko, 2001, Herbut, 2006, Hou et al., 2007, Honerkamp, 2008, Raghu et al., 2008, Liu et al., 2009, Drut and Lähde, 2009, Herbut et al., 2009, Gamayun et al., 2010, Meng et al., 2010, Sorella and Yunoki, 2012, Ulybyshev et al., 2013]. First searches were done in the vicinity of the Dirac point using the Dirac cone approximations. However, nowadays investigations of possible superconductivity states in graphene are in opposite limit, far away from the Dirac points.

In graphene, the sixfold symmetry of the honeycomb lattice favors the degenerate $d_{x^2-y^2}$- and d_{xy}-wave superconductivity states. Recent theoretical studies have shown that an s-wave superconductivity state [Uchoa and Castro Neto, 2007] and a chiral $d_{x^2-y^2} \pm id_{xy}$ superconducting state emerge from electron-electron interactions in graphene doped to the vicinity of the van-Hove singularity point [Black-Schaffer and Doniach, 2007, Honerkamp, 2008, Pathak et al., 2010, Nandkishore et al., 2011, Kiesel et al., 2012, Wang et al., 2012], and in lower doped bilayer graphene [Milovanović and Predin, 2012, Vučićević et al., 2012] (for a recent review, see Ref. [Black-Schaffer and Honerkamp, 2014]). Below the superconducting transition temperature T_C, this degeneracy yields the time-reversal symmetry-breaking $d_{x^2-y^2} \pm id_{xy}$ state [Platt et al., 2013, Black-Schaffer and Honerkamp, 2014]. In the past two years, considerable experimental progress has been made regarding the observation of superconductivity in graphene. Evidence of superconductivity has been experimentally observed on Ca-intercalated bilayer graphene and graphene laminates at 4 [Ichinokura et al., 2016] and 6.4 K [Chapman et al., 2016], respectively. Furthermore, additional experimental progress has been made regarding evidence of superconductivity in Li-decorated monolayer graphene with a transition temperature of approximately 5.9 K [Ludbrook et al., 2015].

In this Chapter, we present an analytical study of the entanglement spectrum of the fermionic ground state on a graphene honeycomb lattice, in the presence of superconductivity instability and as obtained by tracing out a single spin direction. We investigate the relationship between the entanglement and energy spectra of the remaining noninteracting part, placing a special focus on the correlation between their topologies. We show that the entanglement Hamiltonian obtained by tracing out one of the subsystems and the Hamiltonian of the remaining subsystem can have completely different topologies. This difference is due to the fact that the entanglement Hamiltonian is a ground-state property. That is, the $d_{x^2-y^2} + id_{xy}$ superconductivity state breaks the time-reversal symmetry of the superconductivity Hamiltonian; this behaviour is reflected in the ground state of the composite superconductivity Hamiltonian. Further, the entanglement Hamiltonian is constructed from that ground state.

In the next section, the topological phases of the superconductivity states on the honeycomb lattice are classified based on their different symmetries. In Section 5.2, we introduced the model Hamiltonian and discuss the different superconductivity paired states that can arise from the electron–electron interaction on the honeycomb lattice. The renormalized mean-field treatment of self-consistent order parameter is given in Section 5.3. Then, we discuss classification of topological superconductors on a honeycomb lattice based on symmetry of systems in Section 5.4. The entanglement spectrum obtained from the Bardeen-Cooper-Schrieffer ground state by tracing out a single spin direction is analyzed in Section 5.5. Our primary interest in this section is to explore the relationship between the geometrical and topological properties of the entanglement Hamiltonian and the remaining noninteracting Hamiltonian. We close with a conclusion and an outlook, which are presented in Section 5.6.

C_{6v}	E	C_2	2 C_3	2 C_6	3 σ_v	3 σ_d	form
A_1	+1	+1	+1	+1	+1	+1	s-wave
A_2	+1	+1	+1	+1	-1	-1	
B_1	+1	-1	+1	-1	+1	-1	f-wave
B_2	+1	-1	+1	-1	-1	+1	f-wave
E_1	+2	-2	-1	+1	0	0	p_x, p_y
E_2	+2	+2	-1	-1	0	0	$d_{x^2-y^2}$, d_{xy}

Table 5.1: Character table of C_{6v} point groups. The identity operator is given by E. C_2 is the trace of a 180^0 rotation matrix. C_3 and C_6 are 120^0 and 60^0 rotation, respectively. σ_v and σ_d denote reflections at distinct lattice axis.

5.1 SYMMETRY GROUP REPRESENTATION

An understanding of the symmetry of the hexagonal lattice of graphene is essential for its physical properties. Possible superconductivity states and their symmetries are determined by the symmetry of the lattice and can be characterized by group theory. Furthermore, the form of the superconductivity order parameter is denoted by the symmetry group, as we shall see in 5.2.2. The crystal symmetry group for the hexagonal lattice of graphene is C_{6v} and it is presented in Table 5.1.

The fully isotropic A_1 is the fully gapped s-wave superconductivity state. The superconductivity state that breaks additional symmetries (except global $U(1)$ symmetry) in respect of the normal state is called an unconventional superconductivity state. These additional broken symmetries include time-reversal symmetry, crystal lattice symmetry, and spin-rotation symmetry, among others. In this sense, since the s-wave superconductivity state does not break any additional symmetry, is a conventional superconducting state.

The B_1 and B_2 states are spin-triplet f-wave states.

Any linear combination of the elements of the two-dimensional representations of E_1 and E_2 are possible from symmetry requirements. For the two-dimensional representation, E_2 are $d_{x^2-y^2}$ and d_{xy} superconductivity states and are degenerate at T_C according to group theory. However, below T_C, the complex combination, chiral $d_{x^2-y^2} + id_{xy}$ superconductivity states are a fully gapped for graphene doped at and beyond the van Hove singularity point, and minimize the free energy [Black-Schaffer and Honerkamp, 2014].

Recently, it was predicted that the graphene doped to the van Hove singularity point is a chiral d-wave superconductor [Nandkishore et al., 2011,Kiesel et al., 2012,Wang et al., 2012]. The chiral $d_{x^2-y^2} + id_{xy}$ superconductivity states breaks time-reversal symmetry and in this sense, is an unconventional superconductivity state.

Finally, a chiral $p_x + ip_y$ combination that belongs to the E_1, is characterized for the square lattice.

5.2 MODEL HAMILTONIAN

The tight-binding Hamiltonian for free fermions on a graphene honeycomb lattice with a single $2p_z$ orbital per carbon (C) atom is

$$\begin{aligned} H_0 = & -t \sum_{\langle ij \rangle} \sum_{\sigma=\uparrow,\downarrow} \left(a^{\dagger}_{i,\sigma} b_{j,\sigma} + h.c. \right) \\ & - \mu \sum_{i,\sigma} \left(a^{\dagger}_{i,\sigma} a_{i,\sigma} + b^{\dagger}_{i,\sigma} b_{i,\sigma} \right), \end{aligned} \tag{5.1}$$

where t is the hopping energy between the nearest-neighbor C atoms, μ is the chemical potential and $a_{i,\sigma}$ ($a^{\dagger}_{i,\sigma}$), and $b_{i,\sigma}$ ($b^{\dagger}_{i,\sigma}$) are the on-site annihilation (creation) operators for electrons on sublattices A and B, respectively, with spin $\sigma = \uparrow, \downarrow$. Diagonalization of Eq. (5.1) yields the energy spectrum $\pm E_{\pm}$, with

$$E_{\pm} = \pm t |\gamma(\vec{k})| - \mu, \tag{5.2}$$

where $\gamma(\vec{k}) = \sum_{\vec{\delta}} \exp\left(i\vec{k} \cdot \vec{\delta} \right)$ and $\vec{\delta}$ is a nearest-neighbor vector defined by Eq. (2.5). The energy spectrum of the free fermions over the first Brillouin zone is visualized in Fig. 5.1.

5.2.1 *Effective t-J model*

The interaction effects and the symmetry of the lattice are very important for the physics of superconductivity, and condensed matter physics in general. In the presence of the strong Coulomb repulsion, d-wave superconductivity state is the most favorable superconductivity state of the high-temperature cuprate superconductors. Using quantum Monte Carlo simulations, it is found that undoped graphene in the presence of the Coulomb repulsion $U > 3.9t$ could exhibit the order of the antiferromagnetic ground state [Wehling et al., 2011].

In the following, we will consider a simple effective model that gives superconductivity instabilities.

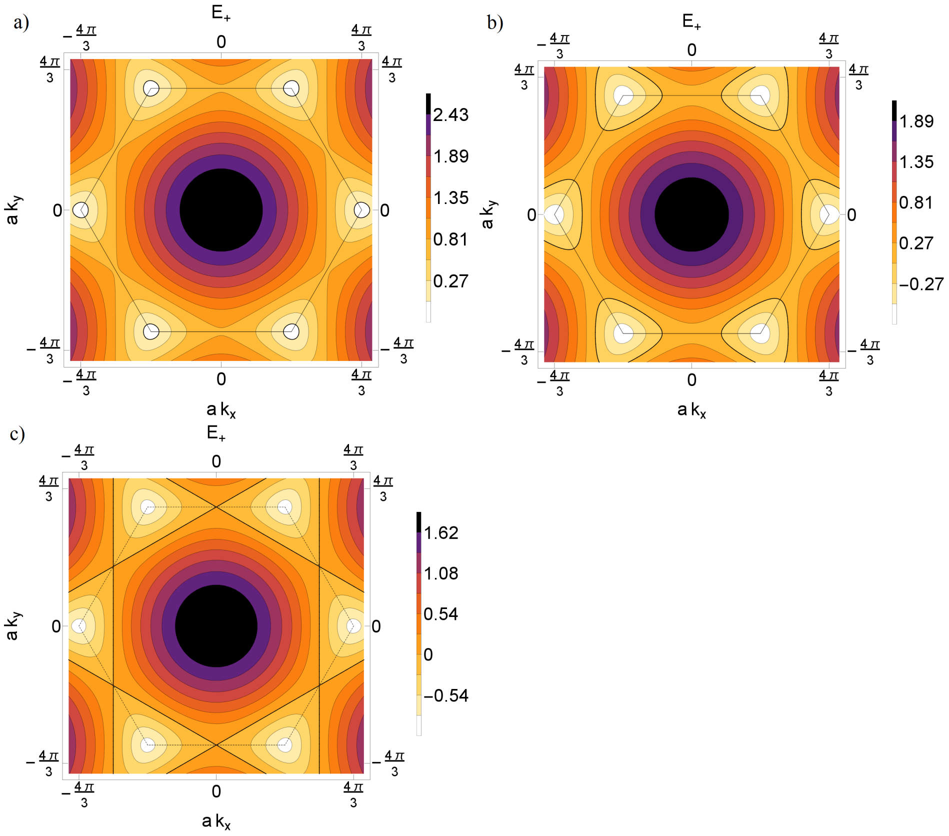

Figure 5.1: Brillouin zone with density plot of $|\gamma(\vec{k})| - \frac{\mu}{t}$ for: (a) $\frac{\mu}{t} = 0.2$; (b) $\frac{\mu}{t} = 0.8$; and (c) $\frac{\mu}{t} = 1$. The edge of the first Brillouin zone is marked by dashed black lines.

The repulsive Hubbard model has the following form in the half-filled case:

$$\mathcal{H}_U = -t \sum_{\langle ij \rangle} \sum_{\sigma} \left(a^{\dagger}_{i,\sigma} b_{j,\sigma} + h.c. \right) + U \sum_{i} n_{i\uparrow} n_{i\downarrow} \tag{5.3}$$

where U is the on-site Coulomb repulsion and n_i is the number operator on the site i. Wehling et al. determined the strength of the on-site Coulomb repulsion to be $U = 3.3t$ by first-principles calculations [Wehling et al., 2011]. The Hubbard Hamiltonian Eq.(5.3) consists of the kinetic part $T = -t \sum_{\langle ij \rangle} \sum_{\sigma} \left(a^{\dagger}_{i,\sigma} b_{j,\sigma} + h.c. \right)$ and the on-site interaction $U = U \sum_{i} n_{i\uparrow} n_{i\downarrow}$. The on-site interaction has a tendency to localize electrons, while the kinetic part resists this localization. We will consider the limit $U >> t$. Hopping of one electron to a neighbor site would cost energy of the order U. While the potential energy is much higher than the kinetic energy, the motion of electrons is frozen.

The Fock space can be divided into two subspaces:

1. subspace spanned by the sites that are maximally occupied by at most one electron per site: $S = \{|n_{1,\uparrow}, n_{1,\downarrow}, n_{2,\uparrow}, n_{2,\downarrow}\rangle : \forall i, n_{i,\uparrow} + n_{i,\downarrow} \leq 1\}$,
2. subspace spanned by at least one site that is double-occupied $D = \{|n_{1,\uparrow}, n_{1,\downarrow}, n_{2,\uparrow}, n_{2,\downarrow}\rangle : \exists i, n_{i,\uparrow} + n_{i,\downarrow} = 2\}$.

Thus, the kinetic part T of the Hubbard Hamiltonian Eq.(5.3) connects subspaces S and D.

We use the projector P, which projects on the subsystem S in order to find the effective Hubbard model Eq.(5.3) in this subspace [Auerbach, 1994]

$$G_{SS}(E) = P\left(E - \mathcal{H}_U\right)^{-1} P = \left(E - \mathcal{H}_{eff}\right)^{-1} \tag{5.4}$$

where we define the effective Hamiltonian $\mathcal{H}_{eff}$. Furthermore, the decomposition of the Hubbard Hamiltonian Eq.(5.3) obtained by the projector P is

$$\mathcal{H}_U = \begin{pmatrix} P\left(U+T\right)P & PT(I-P) \\ (I-P)PT & (I-P)(U+T)(I-P) \end{pmatrix} \tag{5.5}$$

where I is a unitary matrix. Thus, using

$$\begin{pmatrix} A & B \\ C & D \end{pmatrix}^{-1} = \left(A - BD^{-1}C\right)^{-1} \tag{5.6}$$

we obtain the following form of the effective Hamiltonian

$$\begin{aligned} \mathcal{H}_{eff} &= P\left(U+T\right)P \\ &\quad + PT(I-P)\left[(I-P)(E-(U+T))(I+P)\right]^{-1}(I-P)TP. \end{aligned} \tag{5.7}$$

Further approximations $\frac{E}{U} << 1$ and $\frac{I}{U} << 1$ lead to

$$\begin{aligned} \mathcal{H}_{eff} &= PTP - PTU^{-1}TP \\ &= P\left(T - \frac{t^2}{U}\sum_{i,j,k}\sum_{\sigma,\sigma'} c^{\dagger}_{i\sigma}c_{j\sigma}n_{j\uparrow}n_{j\downarrow}c^{\dagger}_{j\sigma'}c_{k\sigma'}\right)P \end{aligned} \tag{5.8}$$

Finally, when $i = k$, we are able to rewrite the effective Hamiltonian in the following form

$$\mathcal{H}_{eff} = -t\sum_{\langle ij\rangle}\sum_{\sigma}\left(a^{\dagger}_{i,\sigma}b_{j,\sigma} + h.c.\right) + J\sum_{\langle ij\rangle}\sum_{\sigma}\left(\vec{S}_i\vec{S}_j - \frac{1}{4}n_in_j\right) \tag{5.9}$$

with an antifferomagnetic exchange constant $J = 2t^2/U$, the spin operator $\vec{S}_i = \frac{1}{2}\sum_{\sigma,\sigma'} c^\dagger_{i\sigma}\vec{\sigma}c_{i\sigma'}$ on the site i. The Heisenberg antiferromagnetism part of the effective Hamiltonian Eq.(5.9) can be seen as a consequence of virtual hopping processes, where an electron with a certain spin direction hops to its neighbor site with opposite spin direction, builds a virtual double occupied site and hops back to the empty site. Thus, the electron reduces its kinetic energy in such a way and electrons are organized in antiferromagnetic order. This process is called a *"super-exchange"* process.

According to the above considerations, in the large-U limit, the Hubbard model can be rewritten as a t-J Hamiltonian:

$$\begin{aligned} H_{t-J} = & -t\sum_{\langle ij\rangle}\sum_{\sigma}\left(a^\dagger_{i,\sigma}b_{j,\sigma} + h.c.\right) + \mu\sum_{i,\sigma}\left(a^\dagger_{i,\sigma}a_{i,\sigma} + b^\dagger_{i,\sigma}b_{i,\sigma}\right) \\ & + J\sum_{\langle ij\rangle}\sum_{\sigma}\left(\vec{S}_i\vec{S}_j - \frac{1}{4}n_i n_j\right). \end{aligned} \tag{5.10}$$

The interaction term can be rewritten as a spin-singlet nearest neighbor attraction

$$J\sum_{\langle ij\rangle}\sum_{\sigma}\left(\vec{S}_i\vec{S}_j - \frac{1}{4}n_i n_j\right) = -J\sum_{\langle i,j\rangle} g^\dagger_{ij}g_{ij} \tag{5.11}$$

with $g^\dagger_{ij} = \frac{1}{\sqrt{2}}\left(a^\dagger_{i\uparrow}b^\dagger_{j\downarrow} - a^\dagger_{i\downarrow}b^\dagger_{j\uparrow}\right)$ when $i \in A$ site and the same with $a \leftrightarrow b$ when $i \in B$. Thus, the interaction term in Eq.(5.11) is an effective resonance valence bond interaction term emphasized by Pauling [Pauling, 1960]. Baskaran estimated the parameter J as $J = \frac{1}{2}\left(\sqrt{U^2 + 16t^2 - U}\right)$ which in graphite with $t \approx 2.5eV$ and $U \approx 6eV$ gives $\frac{J}{t} \sim 1$ [Baskaran and Jafari, 2002]. This model predicts that T_c vanishes for the undoped graphene, while the density of states vanishes at the Dirac points. The doped graphene has a finite density of states and it can be a superconductor.

5.2.2 *Mean-field superconductivity order parameter*

In order to apply the mean-field approximation, we define the superconductivity order parameter as a three-component complex vector

$$\overrightarrow{\Delta} \equiv \left(\Delta_{\vec{\delta}_1}, \Delta_{\vec{\delta}_2}, \Delta_{\vec{\delta}_3}\right), \tag{5.12}$$

where the components are defined by

$$\Delta_{\vec{\delta}} = \left\langle a_{i\uparrow}b_{i+\vec{\delta}\downarrow} - a_{i\downarrow}b_{i+\vec{\delta}\uparrow}\right\rangle. \tag{5.13}$$

We study the superconductivity pairing arising from the nearest-nearest neighbor attractive interaction

$$H_{int} = J \sum_{i,\vec{\delta}} \Delta_{\vec{\delta}} \left(a^{\dagger}_{i\uparrow} b^{\dagger}_{i+\vec{\delta}\downarrow} - a^{\dagger}_{i\downarrow} b^{\dagger}_{i+\vec{\delta}\uparrow} \right). \tag{5.14}$$

The resulting mean-field Hamiltonian can be expressed in momentum space as

$$\begin{aligned} H_{MF} = &- t \sum_{\vec{k}\sigma} \left(\gamma(\vec{k}) a^{\dagger}_{\vec{k}\sigma} b_{\vec{k}\sigma} + h.c. \right) \\ &- \mu \sum_{\vec{k}\sigma} \left(a^{\dagger}_{\vec{k}\sigma} a_{\vec{k}\sigma} + b^{\dagger}_{\vec{k}\sigma} b_{\vec{k}\sigma} \right) \\ &- J \sum_{\vec{k},\vec{\delta}} \left(\Delta_{\vec{\delta}} e^{i\vec{k}\vec{\delta}} \left(a^{\dagger}_{\vec{k}\uparrow} b^{\dagger}_{-\vec{k}\downarrow} - a^{\dagger}_{\vec{k}\downarrow} b^{\dagger}_{-\vec{k}\uparrow} \right) + h.c. \right), \end{aligned} \tag{5.15}$$

where J is the effective pairing potential arising from the electron-electron interaction.

The corresponding span of the superconducting order parameter is

$$\overrightarrow{\Delta} = \begin{cases} \Delta(1,1,1), \\ \Delta(2,-1,-1), \\ \Delta(0,-1,1), \end{cases} \tag{5.16}$$

where Δ is the self-consistent superconductivity order parameter. The first solution corresponds to the s-wave, $\overrightarrow{\Delta} = \Delta(1,1,1)$, belonging to the natural A1 irreducible representation of the C_{6v} group of the honeycomb lattice. The A1 irreducible representation is spanned by the vector $\vec{u}_1 = (1,1,1)$. The final two solutions, $\overrightarrow{\Delta} = \Delta(2,-1,-1)$ and $\overrightarrow{\Delta} = \Delta(0,-1,1)$, belong to the two-dimensional representation E_2, the span of which is $\vec{u}_2 = (2,-1,-1)$ and $\vec{u}_3 = (0,-1,1)$. The second solution corresponds to the $d_{x^2-y^2}$ wave, while the third corresponds to the d_{xy} wave, respectively. From the symmetry perspective, it is noteworthy that every combination of the $d_{x^2-y^2}$ and d_{xy} waves is possible. However, the $d_{x^2-y^2} \pm id_{xy}$-wave superconductivity state with an order parameter

$$\overrightarrow{\Delta}_{d_{x^2-y^2} \pm id_{xy}} = \Delta \begin{pmatrix} 1 \\ e^{\mp\frac{2i\pi}{3}} \\ e^{\pm\frac{2i\pi}{3}} \end{pmatrix} \tag{5.17}$$

is energetically preferred.

The resulting order parameters obtained in correspondence to the symmetry group representation have the following analytical forms

$$\Delta_s(\vec{k}) = \Delta \left(\mathrm{e}^{i\vec{k}\vec{\delta}_1} + \mathrm{e}^{i\vec{k}\vec{\delta}_2} + \mathrm{e}^{i\vec{k}\vec{\delta}_3} \right),$$

$$\Delta_s(\vec{k}) = \Delta\left(\mathrm{e}^{ia\frac{1}{\sqrt{3}}k_y} + 2\cos\left(\frac{a}{2}k_x\right)\mathrm{e}^{-ia\frac{1}{2\sqrt{3}}k_y}\right), \tag{5.18}$$

for the s-wave with $\overrightarrow{\Delta} = \Delta(1,1,1)$,

$$\begin{aligned} \Delta_{d_{x^2-y^2}}(\vec{k}) &= \Delta\left(2\mathrm{e}^{i\vec{k}\vec{\delta}_1} - \mathrm{e}^{i\vec{k}\vec{\delta}_2} - \mathrm{e}^{i\vec{k}\vec{\delta}_3}\right), \\ \Delta_{d_{x^2-y^2}}(\vec{k}) &= 2\Delta\left(e^{i\frac{a}{\sqrt{3}}k_y} - e^{-i\frac{a}{2\sqrt{3}}k_y}\cos(\frac{a}{2}k_x)\right), \end{aligned} \tag{5.19}$$

for the $d_{x^2-y^2}$-wave order parameter with $\overrightarrow{\Delta} = \Delta(2,-1,-1)$, and

$$\begin{aligned} \Delta_{d_{xy}}(\vec{k}) &= \Delta\left(-\mathrm{e}^{i\vec{k}\vec{\delta}_2} + \mathrm{e}^{i\vec{k}\vec{\delta}_3}\right), \\ \Delta_{d_{xy}}(\vec{k}) &= -2i\Delta\sin\left(\frac{a}{2}k_x\right)e^{-i\frac{a}{2\sqrt{3}}k_y}, \end{aligned} \tag{5.20}$$

for the d_{xy}-wave order parameter with $\overrightarrow{\Delta} = \Delta(0,-1,1)$.

Whereas, the $d_{x^2-y^2} + id_{xy}$-wave superconductivity order parameter is

$$\Delta_{d\pm id}(\vec{k}) = \cos\left(\frac{\pi}{3}\right)\Delta_{d_{x^2-y^2}}(\vec{k}) \pm \sin\left(\frac{\pi}{3}\right)\Delta_{d_{xy}}(\vec{k}). \tag{5.21}$$

5.2.3 *Energy band basis*

The kinetic part of the Hamiltonian Eq.(5.15) can be diagonalized by introducing the following transformations

$$\begin{aligned} c_{\vec{k},\sigma} &= \frac{1}{\sqrt{2}}(a_{\vec{k},\sigma} - e^{i\cdot\phi_{\vec{k}}}b_{\vec{k},\sigma}), \\ d_{\vec{k},\sigma} &= \frac{1}{\sqrt{2}}(a_{\vec{k},\sigma} + e^{i\cdot\phi_{\vec{k}}}b_{\vec{k},\sigma}), \end{aligned} \tag{5.22}$$

where the phase $\phi_{\vec{k}}$ is defined as $\phi_{\vec{k}} = \arg(\gamma_{\vec{k}})$. Note that $c^{\dagger}_{\vec{k},\vec{\sigma}}$ and $d^{\dagger}_{\vec{k},\vec{\sigma}}$ create an electron in the upper and lower Bogoliubov bands, respectively. Thus, introducing the energy basis, the Hamiltonian becomes

$$\begin{aligned} H_{MF} &= -t\sum_{\vec{k},\sigma}|\gamma_{\vec{k}}|(d^{\dagger}_{\vec{k},\sigma}d_{\vec{k},\sigma} - c^{\dagger}_{\vec{k},\sigma}c_{\vec{k},\sigma}) \\ &- \mu\sum_{\vec{k},\sigma}(d^{\dagger}_{\vec{k},\sigma}d_{\vec{k},\sigma} + c^{\dagger}_{\vec{k},\sigma}c_{\vec{k},\sigma}) \\ &- J\sum_{\vec{k}}\sum_{\vec{\delta}}\left(\Delta_{\vec{\delta}}\left(\cos(\vec{k}\vec{\delta} - \phi_{\vec{k}})(d^{\dagger}_{\vec{k},\uparrow}d^{\dagger}_{-\vec{k},\downarrow} - c^{\dagger}_{\vec{k},\uparrow}c^{\dagger}_{-\vec{k},\downarrow}) \right.\right. \\ &\left.\left. +\ i\sin(\vec{k}\vec{\delta} - \phi_{\vec{k}})(c^{\dagger}_{\vec{k},\uparrow}d^{\dagger}_{-\vec{k},\downarrow} - d^{\dagger}_{\vec{k},\uparrow}c^{\dagger}_{-\vec{k},\downarrow})\right) + h.c.\right). \end{aligned} \tag{5.23}$$

The third line in this Hamiltonian is the intraband pairing, containing an order parameter that is even in k-space and corresponding to the spin-singlet pairing. The fourth line is the interband pairing, containing an order parameter that is odd in k-space and corresponding to the spin-triplet pairing. We use the definitions

$$C_{\vec{k}} = \sum_{\vec{\delta}} \Delta_{\vec{\delta}} \cos(\vec{k}\vec{\delta} - \phi_{\vec{k}}), \tag{5.24}$$

and

$$S_{\vec{k}} = \sum_{\vec{\delta}} \Delta_{\vec{\delta}} \sin(\vec{k}\vec{\delta} - \phi_{\vec{k}}). \tag{5.25}$$

In a small-momentum expansion $k << a$ around Dirac points $K_\pm$ for the $d_{x^2-y^2}$-wave yields

$$\begin{aligned} C_{K_\pm+\vec{k}}(d_{x^2-y^2}) &\approx \mp 3\Delta \frac{k_x}{\sqrt{k_x^2+k_y^2}}, \\ S_{K_\pm+\vec{k}}(d_{x^2-y^2}) &\approx -3\Delta \frac{k_y}{\sqrt{k_x^2+k_y^2}}. \end{aligned} \tag{5.26}$$

Here, near Dirac points p_x (p_y) symmetries are found for $C_{\vec{k}}$ ($S_{\vec{k}}$), respectively. For the d_{xy}-wave we obtain

$$\begin{aligned} C_{K_\pm+\vec{k}}(d_{xy}) &\approx \pm\sqrt{3}\Delta \frac{k_y}{\sqrt{k_x^2+k_y^2}}, \\ S_{K_\pm+\vec{k}}(d_{xy}) &\approx -\sqrt{3}\Delta \frac{k_x}{\sqrt{k_x^2+k_y^2}}. \end{aligned} \tag{5.27}$$

The combination of $d_{x^2-y^2} + id_{xy}$ in the small-momentum expansion has the following form

$$\begin{aligned} C_{K_\pm+\vec{k}}(d_{x^2-y^2} + id_{xy}) &\approx \mp\frac{3}{2}\Delta \frac{k_x - ik_y}{\sqrt{k_x^2+k_y^2}}, \\ iS_{K_\pm+\vec{k}}(d_{x^2-y^2} + id_{xy}) &\approx \frac{3}{2}\Delta \frac{k_x - ik_y}{\sqrt{k_x^2+k_y^2}}. \end{aligned} \tag{5.28}$$

This is effectively a $p_x - ip_y$ pairing.

Furthermore, for the s-wave we find the following a small-momentum expansion

$$\begin{aligned} C_{K_\pm+\vec{k}} &\approx \mp\frac{a\sqrt{3}}{2}\Delta\sqrt{k_x^2+k_y^2}, \\ S_{K_\pm+\vec{k}} &= 0. \end{aligned} \tag{5.29}$$

$C_{\vec{k}}$ in the first Brillouin zone are plotted in Fig. (5.2).

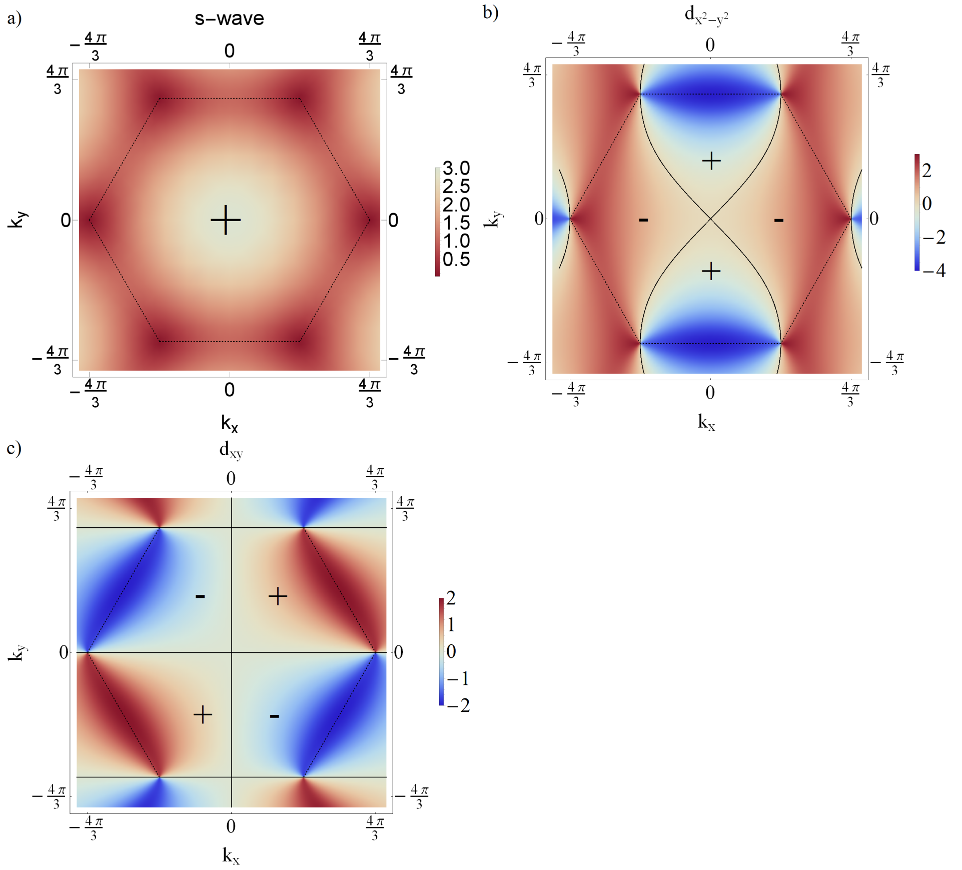

Figure 5.2: The interband order parameter $C_{\vec{k}}$ plotted over Brillouin zone for a) the s-wave with symmetry $\vec{\Delta} = \Delta(1,1,1)$, b) the $d_{x^2-y^2}$-wave with symmetry $\vec{\Delta} = \Delta(2,-1,-1)$, and c) the d_{xy}-wave with symmetry $\vec{\Delta} = \Delta(0,-1,1)$. The thick black line indicates zero values, while plus indicates positive values, and minus indicates negative values. The dashed black line delineates the first Brillouin zone.

5.3 RENORMALIZED MEAN-FIELD THEORY

As we have seen in 5.2.1, the Gutzwiller projector reduced the space of t-J Hamiltonian Eq.(5.10) by excluding double occupied sites. However, within the renormalized mean-field theory the condition of the exclusion of doubly occupied sites is relaxed by replacing the tight-binding parameters by statistical weights $t \rightarrow g_t t$ where $g_t = \frac{2\delta}{1+\delta}$ and $J \rightarrow g_s J$, where $g_s = \frac{4}{(1+\delta^2)}$ with $\delta = 1 - n$ is the doping away from half-filling per site, where $\delta = 0$ corresponds to the undoped graphene [Vollhardt, 1984]. The numerical approach for solving of the self-consistency equations for the superconducting bond order in order to get the superconductivity critical temperature T_c and the order parameter Δ has already been preformed in Refs. [Wu et al., 2013, Black-Schaffer et al., 2014].

5.3.1 *s-wave scenario*

The Hamiltonian Eq.(5.23) for s-wave superconductivity state can be diagonalized by Bogoliubov transformations

$$\begin{aligned}\mathcal{H} =& E_0^{(1)} + \sum_{\vec{k}} E_\alpha (e_{\vec{k}\dagger} e_{\vec{k}} + e^\dagger_{-\vec{k}} e_{-\vec{k}}) \\ &+ E_0^{(2)} + \sum_{\vec{k}} E_\beta (f^\dagger_{\vec{k}} f_{\vec{k}} + f^\dagger_{-\vec{k}} f_{-\vec{k}}) + \frac{N_s |\Delta|^2}{g_s J} \end{aligned} \tag{5.30}$$

where

$$E_0^{(1)} = - \sum_{\vec{k}} \left(t|\gamma(\vec{k})| - \mu \right) - \sum_{\vec{k}} E_\alpha, \tag{5.31}$$

$$E_0^{(2)} = \sum_{\vec{k}} \left(t|\gamma(\vec{k})| + \mu \right) - \sum_{\vec{k}} E_\beta. \tag{5.32}$$

The energies of Bogoliubov quasi-particles are

$$E_\alpha = \sqrt{\left(t\gamma(\vec{k})| - \mu \right)^2 + J^2 |C_{\vec{k}}|^2} \tag{5.33}$$

$$E_\beta = \sqrt{\left(t\gamma(\vec{k})| + \mu \right)^2 + J^2 |C_{\vec{k}}|^2}. \tag{5.34}$$

The Bogoliubov transformations $e_{\vec{k},+}$ and $f_{\vec{k},+}$ are given in Appendix D by Eqs.(D.1, D.2). The total number of unit cells is N_s.

The free energy then becomes

$$\begin{aligned} F =& - \frac{2}{\beta} \sum_{\vec{k}} \ln \left(2\cosh \left(\frac{\beta E_\alpha}{2} \right) \right) \\ & - \frac{2}{\beta} \sum_{\vec{k}} \ln \left(2\cosh \left(\frac{\beta E_\beta}{2} \right) \right) \\ & - N_s \mu + \frac{N_s |\Delta|^2}{g_s J} \end{aligned} \tag{5.35}$$

where $\beta = \frac{1}{k_B T}$ denotes the inverse temperature, with k_B is the Bolztmann constant.

The conditions for the minimum of the free energy are given by

$$\frac{\partial F}{\partial \delta} = 0, \quad \frac{\partial F}{\partial \Delta} = 0. \tag{5.36}$$

The superconductivity critical temperature T_c and the order parameter Δ can be found by solving the self-consistence equations

$$\begin{aligned}\delta =&\frac{1}{N_s}\sum_{\vec{k}}\frac{t|\gamma(\vec{k})|-\mu}{E_\alpha}\tanh\left(\frac{\beta E_\alpha}{2}\right)\\ -&\frac{1}{N_s}\sum_{\vec{k}}\frac{t|\gamma(\vec{k})|+\mu}{E_\beta}\tanh\left(\frac{\beta E_\beta}{2}\right)\end{aligned} \tag{5.37}$$

$$\begin{aligned}\Delta =&\frac{Jg_s}{8N_s}\sum_{\vec{k}}\frac{\Delta|\gamma(\vec{k})|}{E_\alpha}\tanh\left(\frac{\beta E_\alpha}{2}\right)\\ +&\frac{Jg_s}{4N_s}\sum_{\vec{k}}\frac{\Delta|\gamma(\vec{k})|}{E_\beta}\tanh\left(\frac{\beta E_\beta}{2}\right).\end{aligned} \tag{5.38}$$

We solve the self-consistence equations Eq.(5.38) in two opposite limits, close to the T_c when the order parameter Δ is very small and when temperature is $T = 0$. The numerical solutions of these equations will be discussed in 5.3.3.

5.3.2 *d-wave scenario*

To enable further calculations, we diagonalize the Hamiltonian Eq.(5.55) for the chiral d-wave superconductivity state

$$\begin{aligned}H_{MF} =&\sum_{\vec{k}}E_\alpha(o^\dagger_{\vec{k},+}o_{\vec{k},+}+o^\dagger_{-\vec{k},-}o_{-\vec{k},-})\\ +&\sum_{\vec{k}}E_\beta(p^\dagger_{\vec{k},+}p_{\vec{k},+}+p^\dagger_{-\vec{k},-}p_{-\vec{k},-})\end{aligned} \tag{5.39}$$

by the Bogoliubov quasiparticles $o_{\vec{k},+}, o_{-\vec{k},-}, p_{\vec{k},+}$ and $p_{-\vec{k},-}$ given in Appendix (C) with Eqs.(C.30)-Eq.(C.31). The energies of the Bogoliubov quasiparticles are $\pm E_\alpha$ and $\pm E_\beta$, where

$$E_\alpha = \sqrt{t^2|\gamma(\vec{k})|^2+\mu^2+\left(|S_{\vec{k}}|^2+|C_{\vec{k}}|^2\right)+2\sqrt{u+v}}, \tag{5.40}$$

and

$$E_\beta = \sqrt{t^2|\gamma(\vec{k})|^2+\mu^2+\left(|S_{\vec{k}}|^2+|C_{\vec{k}}|^2\right)-2\sqrt{u+v}} \tag{5.41}$$

with

$$u = \left(\mu^2+|S_{\vec{k}}|^2\right)t^2|\gamma(\vec{k})|^2, \tag{5.42}$$

and

$$v = \left(\mathrm{R}e(C_{\vec{k}})\mathrm{I}m(S_{\vec{k}})-\mathrm{R}e(S_{\vec{k}})\mathrm{I}m(C_{\vec{k}})\right)^2. \tag{5.43}$$

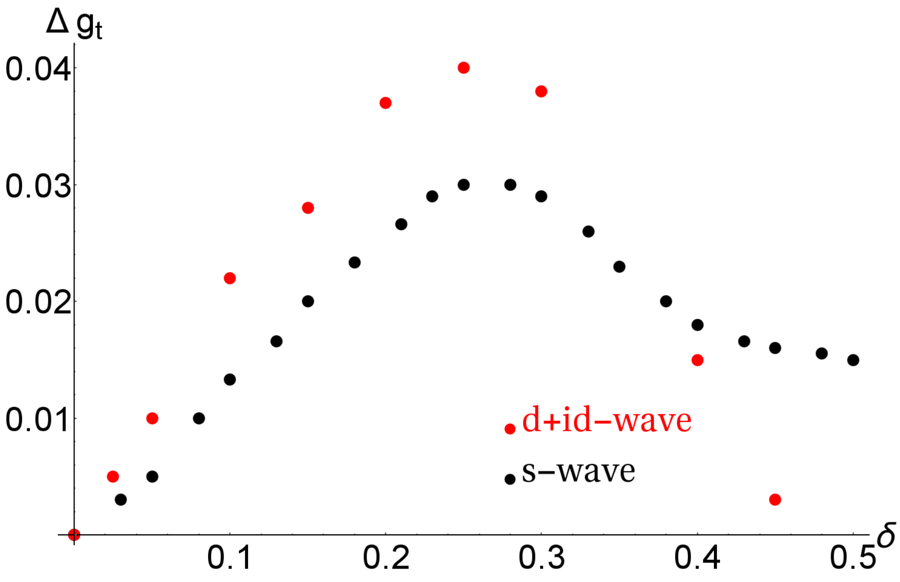

Figure 5.3: The superconductivity transition temperature T_C ($T_C \sim g_t\Delta$) for the s-wave and the $d_{x^2-y^2} + id_{xy}$-wave as a function of doping δ and for $J/t = 0.8$. The superconductivity order parameter Δ is given units $\frac{3}{4}g_s J$.

When the superconductivity order parameters $\Delta_{\vec{\delta}}$ are purely real, i.e., when no time-reversal symmetry breaking occurs, v vanishes.

We obtain the following self-consistence equations

$$\frac{\partial E_\alpha}{\partial \Delta} = \frac{|C_{\vec{k}}|^2}{\Delta E_\alpha} + \frac{|S_{\vec{k}}|^2}{\Delta E_\alpha} + \frac{1}{2\Delta E_\alpha}\frac{|S_{\vec{k}}|^2 t^2 |\gamma(\vec{k})|^2 + 2v^2}{\sqrt{u^2+v^2}} \tag{5.44}$$

$$\frac{\partial E_\beta}{\partial \Delta} = \frac{|C_{\vec{k}}|^2}{\Delta E_\beta} + \frac{|S_{\vec{k}}|^2}{\Delta E_\beta} - \frac{1}{\Delta E_\beta}\frac{|S_{\vec{k}}|^2 t^2 |\gamma(\vec{k})|^2 + 2v^2}{\sqrt{u^2+v^2}} \tag{5.45}$$

$$\frac{\partial E_\alpha}{\partial \mu} = \frac{\mu}{E_\alpha} + \frac{1}{2\Delta E_\alpha}\frac{\mu t^2 |\gamma(\vec{k})|^2}{\sqrt{u^2+v^2}} \tag{5.46}$$

$$\frac{\partial E_\beta}{\partial \mu} = \frac{\mu}{E_\beta} - \frac{1}{2\Delta E_\beta}\frac{\mu t^2 |\gamma(\vec{k})|^2}{\sqrt{u^2+v^2}}. \tag{5.47}$$

5.3.3 *Numerical results*

The value of T_C and the superconductivity order parameter Δ are obtained as solutions of the self-consistence equations to fix the values of t, J, and the finite electron doping or hole doping, δ (chemical potential is a function of the doping). In Fig.(5.3), we plot Δg_t for the s-wave and chiral $d_{x^2-y^2} + id_{xy}$-wave superconductivity state for a fixed value $J/t = 0.8$ as a function of doping δ. Δg_t is an approximation for T_C within renormalized mean-field theory.

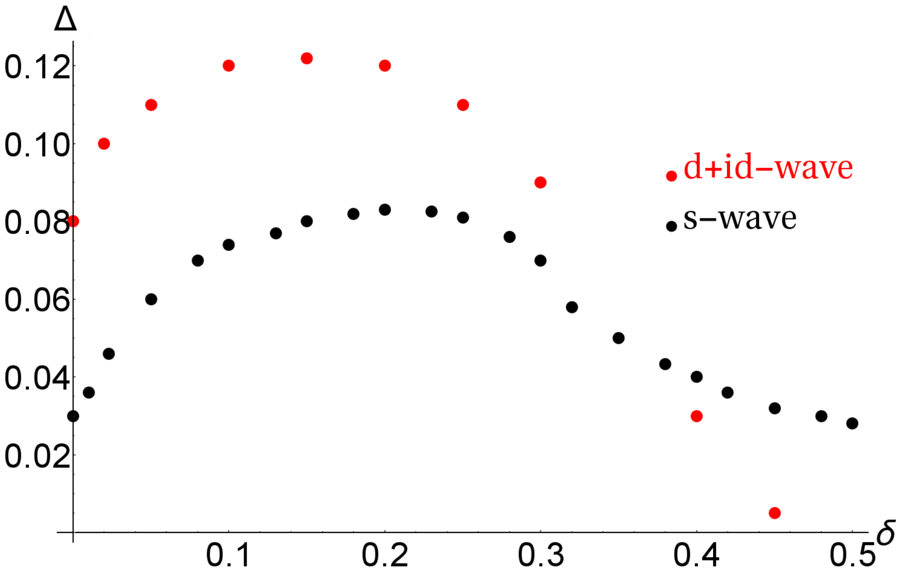

Figure 5.4: The-self consistent superconductivity order parameter Δ for the s-wave and the $d_{x^2-y^2} + id_{xy}$ as a function of doping δ and for $J/t = 0.8$ in units $\frac{3}{4}g_s J$.

In this work, we will consider graphene doped below and around the van-Hove singularity point, which corresponds to $\delta = 1/4$. For this doping, T_C for the chiral $d_{x^2-y^2} + id_{xy}$-wave is much higher than for the s-wave and is preferred. As we have pointed out in 5.1, any combination of the $d_{x^2-y^2}$- and d_{xy}-wave is allowed from a symmetry point of view. Black-Schaffer and Doniach numerically solved the self-consistence equations to obtain that the chiral $d_{x^2-y^2} + id_{xy}$-wave with $\vec{\Delta} = \Delta(1, e^{\mp\frac{2i\pi}{3}}, e^{\pm\frac{2i\pi}{3}})$ is energetically favored. We present our numerical results for the superconductivity order parameter Δ for s-wave and chiral $d_{x^2-y^2} + id_{xy}$- wave at $T = 0$ in Fig. (5.4).

5.4 SYMMETRY ANALYSIS

Introducing the spinor

$$\varphi^{\dagger}_{\vec{k}} = \left(a^{\dagger}_{\vec{k}\uparrow}, b^{\dagger}_{\vec{k}\uparrow}, a^{\dagger}_{\vec{k}\downarrow}, b^{\dagger}_{\vec{k}\downarrow}, a_{-\vec{k}\uparrow}, b_{-\vec{k}\uparrow}, a_{-\vec{k}\downarrow}, b_{-\vec{k}\downarrow}\right), \tag{5.48}$$

the Hamiltonian of Eq. (5.15) can be expressed as

$$H_{MF} = \frac{1}{2}\sum_{\vec{k}} \varphi^{\dagger}_{\vec{k}} \mathcal{M}_{\vec{k}} \varphi_{\vec{k}}, \tag{5.49}$$

where

$$\mathcal{M}_{\vec{k}} = \begin{pmatrix} \zeta(\vec{k}) & 0 & 0 & -\overline{\Delta}(\vec{k}) \\ 0 & \zeta(\vec{k}) & \overline{\Delta}(\vec{k}) & 0 \\ 0 & \overline{\Delta}^*(-\vec{k}) & -\zeta^*(-\vec{k}) & 0 \\ -\overline{\Delta}^*(-\vec{k}) & 0 & 0 & -\zeta^*(-\vec{k}) \end{pmatrix}, \quad (5.50)$$

with

$$\zeta(\vec{k}) = \begin{pmatrix} -\mu & -t\gamma(\vec{k}) \\ -t\gamma^*(\vec{k}) & -\mu \end{pmatrix}, \quad (5.51)$$

$$\overline{\Delta}(\vec{k}) = \begin{pmatrix} 0 & \Delta(\vec{k}) \\ \Delta(-\vec{k}) & 0 \end{pmatrix}. \quad (5.52)$$

The resultant Hamiltonian indicates that the spin-singlet superconductivity state without spin-orbit coupling is invariant under the spin SU(2) rotation. Hence, we obtain the condition

$$\left[J_i, \mathcal{M}(\vec{k})\right] = 0, \qquad J_i = \begin{pmatrix} s_i & 0 \\ 0 & -s_i^* \end{pmatrix}, \qquad (i = x, y, z). \quad (5.53)$$

As a result of the spin SU(2) rotation, it is sufficient to use the spinor $\mathbf{\Psi}^\dagger_{\vec{k}} = (a^\dagger_{\vec{k}\uparrow}, b^\dagger_{\vec{k}\uparrow}, a_{-\vec{k}\downarrow}, b_{-\vec{k}\downarrow})$ in order to express the Hamiltonian of the superconductivity state on the honeycomb lattice in the form

$$H_{MF} = \sum_{\vec{k}} \mathbf{\Psi}^\dagger_{\vec{k}} h(\vec{k}) \mathbf{\Psi}_{\vec{k}}, \quad (5.54)$$

where

$$h(\vec{k}) = \begin{pmatrix} -\mu & -t\gamma(\vec{k}) & 0 & -\Delta(\vec{k}) \\ -t\gamma^*(\vec{k}) & -\mu & -\Delta(-\vec{k}) & 0 \\ 0 & -\Delta^*(-\vec{k}) & \mu & t\gamma^*(-\vec{k}) \\ -\Delta^*(\vec{k}) & 0 & t\gamma(-\vec{k}) & \mu \end{pmatrix}. \quad (5.55)$$

When the superconductivity order parameter is purely real, the Hamiltonian $h(\vec{k})$ satisfies

$$Th(\vec{k})T^{-1} = h(-\vec{k}), \quad (5.56)$$

where $T = K$ mimics time-reversal symmetry. The condition given in Eq. (5.56) can satisfy a real superconductivity order parameter only. The $d_{x^2-y^2} + id_{xy}$-wave superconductivity order parameter given in Eq. (5.21) breaks the time-reversal symmetry. It appertains to the CI-class in the Altland-Zirnbauer classification of topological insulators and superconductors [Sato and Fujimoto, 2016, Altland and Zirnbauer, 1997, Schnyder et al., 2008]. Furthermore, it is possible to classify two-dimensional C-class superconductors using the Chern number C. Note that the nontrivial topology of the $d_{x^2-y^2}+id_{xy}$-wave superconductivity state is denoted by the Chern number $C=2$.

5.5 ENTANGLEMENT SPECTRA

A method for analytically calculating the entanglement spectrum of a free-fermion system is given in Refs. [Peschel, 2003, Cheong and Henley, 2004, Schliemann, 2013]. Here, we generalize this method to superconductivity systems, using an approach similar to that described in Refs. [Borchmann et al., 2014, Kim, 2014].

The entanglement Hamiltonian can be constructed as a single-particle operator in a quadratic matrix [Peschel, 2003, Cheong and Henley, 2004, Schliemann, 2013], as it is completely determined by any correlation matrix of operators acting on the remaining part after the subsystem has been traced out. Our system consists of two subsystems, A and B. The reduced density matrix for subsystem A, defined as $\rho_A = \mathrm{tr}_B\,\rho$, can be formulated as in the free fermion case, such that $\rho_A = \frac{1}{Z}e^{-H_{ent}}$, using the entanglement spectrum H_{ent} and the partition function $Z = \mathrm{t}r\left(e^{-H_{\mathrm{ent}}}\right)$. Furthermore, the average $\langle\mathcal{O}\rangle$ of a local operator in subsystem A can be calculated as $\langle\mathcal{O}\rangle = \mathrm{tr}(\rho_A\mathcal{O}_A)$.

By tracing out a single spin direction, e.g., the negative spin $\downarrow$, from the ground state on the honeycomb lattice in the presence of the s-wave and chiral $d+id$-wave superconductivity, the correlation matrix can be formulated as

$$C(\vec{k}) = \begin{pmatrix} \langle a^{\dagger}_{\vec{k}\uparrow}a_{\vec{k}\uparrow}\rangle & \langle a^{\dagger}_{\vec{k}\uparrow}b_{\vec{k}\uparrow}\rangle \\ \langle b^{\dagger}_{\vec{k}\uparrow}a_{\vec{k}\uparrow}\rangle & \langle b^{\dagger}_{\vec{k}\uparrow}b_{\vec{k}\uparrow}\rangle \end{pmatrix}. \tag{5.57}$$

For more technical details of the analytical calculations of the correlation matrix, we refer the reader to Appendix (D). Here, one can show that the eigenvalues of the correlation matrix η_l are related to the entanglement spectrum ξ_l, such that

$$\xi_l = \ln\left(\frac{1-\eta_l}{\eta_l}\right). \tag{5.58}$$

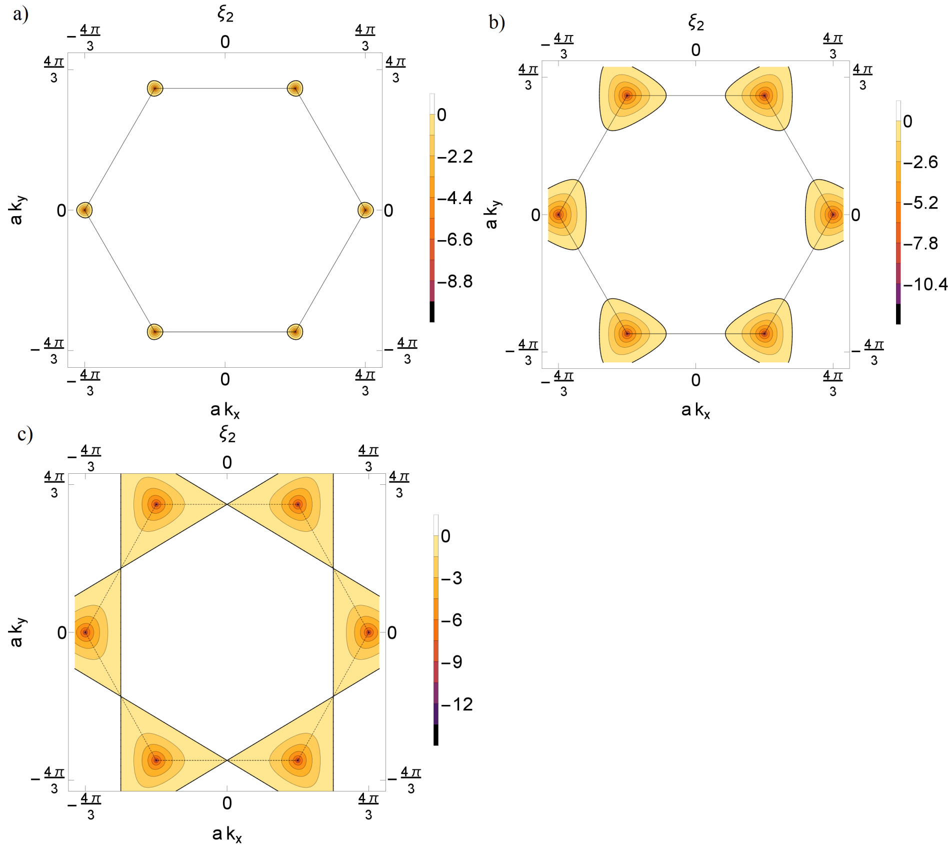

Figure 5.5: Contour plot of entanglement level $\xi_1(\vec{k})$ of s-wave superconductivity state on honeycomb lattice plotted for $\frac{J}{t} = 3$ and: (a) $\frac{\mu}{t} = 0.2$; (b) $\frac{\mu}{t} = 0.8$; and (c) $\frac{\mu}{t} = 1$. The thin dashed and thick black lines represent the first Brillouin zone and connect the zero energy states, respectively.

5.5.1 *s-wave scenario*

The s-wave superconductivity order parameter corresponds to the bond-independent superconductivity state; thus, $S_{\vec{k}}$ is identically zero.

We analytically obtain the entanglement levels (Eq. (5.58))

$$\xi_1(\vec{k}) = -2\,\mathrm{arsinh}\left(\frac{t|\gamma(\vec{k})| + \mu}{|C_{\vec{k}}|}\right) \tag{5.59}$$

and

$$\xi_2(\vec{k}) = 2\,\mathrm{arsinh}\left(\frac{t|\gamma(\vec{k})| - \mu}{|C_{\vec{k}}|}\right). \tag{5.60}$$

The entanglement Hamiltonian has the form

$$\mathcal{H}_{ent} = \sum_{\vec{k}} \left(\xi_1 e^{\dagger}_{\vec{k},+} e_{\vec{k},+} + \xi_2 f^{\dagger}_{\vec{k},+} f_{\vec{k},+}\right), \tag{5.61}$$

where $e_{\vec{k},+}$ and $f_{\vec{k},+}$ are Bogoliubov transformations given in Appendix D by Eqs.(D.1)- (D.2). The entanglement levels for different values of μ, with $t = 2.5eV$, and $\Delta = 3eV$, are shown in Fig. 5.5.

In general, there is no proportionality between the entanglement Hamiltonian and the energy Hamiltonian of free fermions, because the coupling between subsystems $C_{\vec{k}}$ is $\vec{k}$-dependent in the Brillouin zone. When $C_{\vec{k}} = 0$, at the Dirac points, the entanglement levels are not entangled. However, at finite doping, the maximally entangled states, when the entanglement levels are zero, correspond to the zero energy state of the noninteracting fermions. To provide a superior visualization, a thick black line is used to connect the zero-energy states in Fig. 5.1 and the maximally entangled states in Fig. 5.5.

Entanglement thermodynamic

The undoped graphene is a gapless semi-metal and is not a superconductor at low temperatures. However, when the system is at half-filling (with $\mu = 0$), the entanglement levels are

$$\xi_{1,2}(\vec{k}) = \pm 2\,\mathrm{arsinh}\left(\frac{t}{\Delta}\right), \tag{5.62}$$

being constant over the entire Brillouin zone. In the strong coupling regime between subsystems, when $\Delta \gg t$, one finds

$$\xi_{1,2}(\vec{k}) \approx \pm 2\frac{t}{\Delta}. \tag{5.63}$$

In what follows we will use the redefinition $\lambda \equiv \frac{1}{\Delta}$ for the phenomenological scale.

The concept of the entanglement thermodynamics given in Ref. [Schliemann, 2011, Schliemann, 2013, Schliemann, 2014] have been already discussed in Chapter 3.

Here, the entanglement entropy and energy are

$$\begin{aligned} S =& 2\ln\left(1+\mathrm{e}^{2t\lambda}\right) - 2t\lambda\left(1+\tanh\left(t\lambda\right)\right) \\ \overline{E} =& -2t\lambda\tanh\left(t\lambda\right), \end{aligned} \tag{5.64}$$

respectively. This leads

$$\frac{\partial\left(\overline{E}-S\right)}{\partial\lambda} = -2t\tanh\left(t\lambda\right) \tag{5.65}$$

and further to

$$\frac{\partial\beta(\lambda)}{\partial\lambda} = \frac{1}{\lambda}. \tag{5.66}$$

The inverse thermodynamic temperature is proportional the phenomenological inverse temperature

$$\beta(\lambda) = k_E \lambda \tag{5.67}$$

where k_E is a constant. Finally, the canonical entanglement Hamiltonian at half-filling is independent of the inverse temperature $\beta = k_E/\Delta$, such that

$$\mathcal{H}_{can} = \frac{1}{k_E}\left(e^{\dagger}_{\vec{k},+}e_{\vec{k},+} - f^{\dagger}_{\vec{k},+}f_{\vec{k},+}\right) \tag{5.68}$$

where operators $e_{\vec{k},+}$ and $f_{\vec{k},+}$ are given in the Appendix D with Eqs.(D.1)-(D.2), respectively.

5.5.2 *chiral d-wave scenario*

From analytical calculations, one obtains the correlation matrix at $T = 0$

$$C(\vec{k}) = \begin{pmatrix} C_{11}(\vec{k}) & C_{12}(\vec{k}) \\ C^{*}_{12}(\vec{k}) & C_{22}(\vec{k}) \end{pmatrix}, \tag{5.69}$$

where

$$\begin{aligned} C_{11} &= \langle a^{\dagger}_{\vec{k}\uparrow} a_{\vec{k}\uparrow}\rangle \\ &= \frac{1}{2} + \frac{1}{4}\frac{\mu}{\sqrt{\mu^2+|S_{\vec{k}}|^2}}(\epsilon_1 + m)\frac{1}{E_\alpha}\left(1 - \frac{m}{\sqrt{t^2|\gamma(\vec{k})|^2+m^2}}\right) \\ &+ \frac{1}{4}\frac{\mu}{\sqrt{\mu^2+|S_{\vec{k}}|^2}}(\epsilon_2 + m)\frac{1}{E_\beta}\left(1 + \frac{m}{\sqrt{t^2|\gamma(\vec{k})|^2+m^2}}\right), \end{aligned} \tag{5.70}$$

$$\begin{aligned} C_{22} &= \langle b^{\dagger}_{\vec{k}\uparrow} b_{\vec{k}\uparrow}\rangle \\ &= \frac{1}{2} + \frac{1}{4}\frac{\mu}{\sqrt{\mu^2+|S_{\vec{k}}|^2}}(\epsilon_1 - m)\frac{1}{E_\alpha}\left(1 + \frac{m}{\sqrt{t^2|\gamma(\vec{k})|^2+m^2}}\right) \\ &+ \frac{1}{4}\frac{\mu}{\sqrt{\mu^2+|S_{\vec{k}}|^2}}(\epsilon_2 - m)\frac{1}{E_\beta}\left(1 - \frac{m}{\sqrt{t^2|\gamma(\vec{k})|^2+m^2}}\right), \end{aligned} \tag{5.71}$$

$$\begin{aligned} C_{12} &= \langle a^{\dagger}_{\vec{k}\uparrow} b_{\vec{k}\uparrow}\rangle \\ &= \frac{1}{4}e^{-i\phi_{\vec{k}}}\left(\left(\frac{\epsilon_1}{E_\alpha} - \frac{\epsilon_2}{E_\beta}\right) - in\left(\frac{1}{E_\alpha} - \frac{1}{E_\beta}\right)\right)\frac{t|\gamma(\vec{k})|}{\sqrt{t^2|\gamma(\vec{k})|^2+m^2}} \end{aligned} \tag{5.72}$$

with

$$\epsilon_{1,2} = \sqrt{\mu^2+|S_{\vec{k}}|^2} \pm \sqrt{t^2|\gamma(\vec{k})|^2+m^2}, \tag{5.73}$$

while

$$m = \frac{\mathrm{Re}(C_{\vec{k}}) \cdot Im(S_{\vec{k}}) - \mathrm{Im}(C_{\vec{k}}) \cdot \mathrm{Re}(S_{\vec{k}})}{\sqrt{\mu^2 + |S_{\vec{k}}|^2}}, \tag{5.74}$$

and

$$n = \frac{\mathrm{R}e(C_{\vec{k}})\mathrm{R}e(S_{\vec{k}}) + \mathrm{I}m(C_{\vec{k}})\mathrm{I}m(S_{\vec{k}})}{\sqrt{\mu^2 + |S_{\vec{k}}|^2}}. \tag{5.75}$$

Thus, the entanglement spectrum obtained from the eigenvalues of the correlation matrix given in Eq. (5.58) consists of entanglement levels ξ_1 and ξ_2 where

$$\xi_{1,2} = -2\,\mathrm{artanh}(C_{11} + C_{22} - 1 \pm \sqrt{(C_{11} - C_{22})^2 + 4|C_{12}|^2}). \tag{5.76}$$

As the d-wave spin-singlet superconductivity order parameter involves both $C_{\vec{k}}$ and $S_{\vec{k}}$, there is no relationship between states with the zero-value states of the entanglement spectrum and the zero-energy states of the free fermions. At the van-Hove singularity point, i.e., when $\mu = t$, both the entanglement spectrum and the energy spectrum of the free fermions are zero at the M point. The results of our analytical calculations of the entanglement spectrum of the $d_{x^2-y^2} + id_{xy}$-wave superconductivity on the honeycomb lattice are presented in Fig. 5.6.

As we have discussed above, the $d_{x^2-y^2}$- and d_{xy}-wave superconductivity order parameters preserve the time-reversal symmetry (Eq. (5.56)). Based on the time-reversal symmetry and provided $\mathbf{\Psi}_{\vec{k}}$ are the eigenstates of the Hamiltonian given in Eq.(5.55), we can state that

$$\mathbf{\Psi}^*_{\vec{k}} = \mathbf{\Psi}_{-\vec{k}}, \tag{5.77}$$

where the $\mathbf{\Psi}^*_{-\vec{k}}$ are also eigenstates of the Hamiltonian of Eq. (5.55). This yields

$$\mathbf{\Phi}^*_{\vec{k}} = \mathbf{\Phi}_{-\vec{k}}. \tag{5.78}$$

Hence, the real d-wave superconductivity order parameter preserves the time-reversal symmetry in the correlation matrix, which is constructed from the $\mathbf{\Phi}_{\vec{k}}$ as $C(\vec{k}) = \langle \mathbf{\Phi}^\dagger_{\vec{k}} \mathbf{\Phi}_{\vec{k}} \rangle$. The entanglement Hamiltonian satisfies:

$$T_E \mathcal{H}_{ent}(\vec{k}) T_E^{-1} = \mathcal{H}_{ent}(-\vec{k}), \tag{5.79}$$

with $T_E = K$.

When the $d_{x^2-y^2} + id_{xy}$-wave superconductivity order parameter is considered, $C_{\vec{k}}$ and $S_{\vec{k}}$ are complex functions. Then, the m and n terms are non-zero. Hence, the average occupancy number at site A, $C_{11}(\vec{k})$, and the average occupancy number at site B,

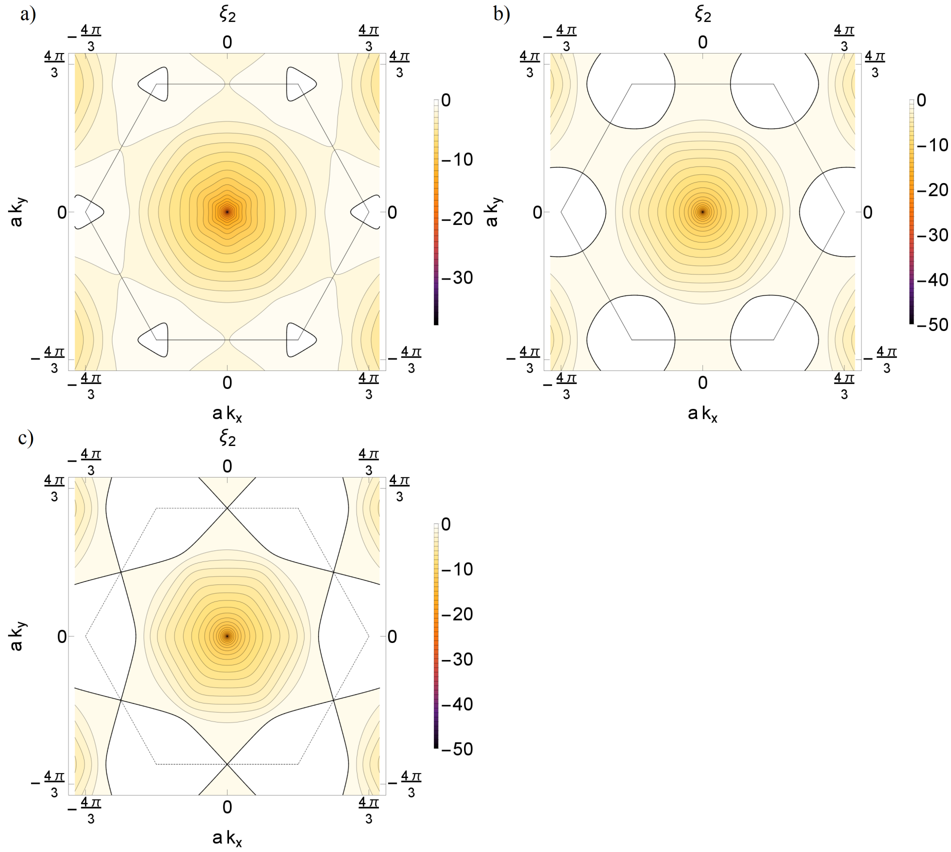

Figure 5.6: Contour plot of entanglement level $\xi_1(\vec{k})$ of $d_{x^2-y^2}+id_{xy}$ -wave superconductivity state on honeycomb lattice plotted for $\frac{J}{t}=3$, and a) $\frac{\mu}{t}=0.2$, b) $\frac{\mu}{t}=0.8$ and c) $\frac{\mu}{t}=1$. The dashed black line delineates the first Brillouin zone, while the thick black line shows maximally entangled states.

$C_{22}(\vec{k})$, are inequivalent and the off-diagonal element of the correlation matrix $C_{12}(\vec{k})$ is complex. Because $S_{\vec{k}}$ is an odd function in the momentum space, while $C_{\vec{k}}$ is a even function, it can be shown that elements of the correlation matrix $C_{11}(\vec{k})$, $C_{22}(\vec{k})$, and $C_{12}(\vec{k})$ are constrained as $C_{11}(-\vec{k}) = C_{22}(\vec{k})$ and $C_{12}^{*}(-\vec{k}) = C_{12}(\vec{k})$. Therefore, it follows that the complex $d_{x^2-y^2} + id_{xy}$-wave superconductivity order parameter breaks the time-reversal symmetry in the entanglement Hamiltonian. The topology of the entanglement Hamiltonian in two-dimension with broken time-reversal symmetry is characterized by the entanglement Chern number.

For further analysis of the topological properties of the entanglement Hamiltonian, we require not only its eigenvalues, but also its eigenstates. The eigenstates of the correlation matrix are identical to the eigenstates of the entanglement Hamiltonian and can be expressed as

$$q_{\vec{k}\uparrow} = \delta_{+}(\vec{k}) a_{\vec{k}\uparrow} + \delta_{-}(\vec{k}) b_{\vec{k}\uparrow} \tag{5.80}$$

$$r_{\vec{k}\uparrow} = \delta_{+}(-\vec{k}) a_{\vec{k}\uparrow} - \delta_{-}^{*}(-\vec{k}) b_{\vec{k}\uparrow} \tag{5.81}$$

where explicit expressions for $\delta_{+}(\vec{k})$ and $\delta_{-}(\vec{k})$ are given in Appendix (D) by Eq.(D.21). Using these eigenstates, we can calculate the Berry curvature

$$F(\vec{k}) = \frac{\partial A_y}{\partial k_x} - \frac{\partial A_x}{\partial k_y}, \tag{5.82}$$

and the Berry connection

$$\vec{A}(\vec{k}) = i \langle r(\vec{k}) | \frac{\partial}{\partial \vec{k}} | r(\vec{k}) \rangle. \tag{5.83}$$

Through numerical integrations of the Berry curvature along the Brillouin zone, we find that the entanglement Chern number is $C = 1$, in the case of the chiral $d_{x^2-y^2} + id_{xy}$-wave superconductivity state. In the presence of $SU(2)$ rotation and broken time-reversal symmetry, as in the case of an energetic Hamiltonian, the Chern number C can have even values only. For the entanglement Hamiltonian, it is possible to obtain an odd value for the Chern number, as it is not invariant to the $SU(2)$ rotation. As a result, the topology of the entanglement Hamiltonian, which is obtained by tracing out the spin-down subsystem of the ground state of the chiral $d_{x^2-y^2} + id_{xy}$-wave superconductivity state on the honeycomb lattice, clearly differs from the topology of the energetic Hamiltonian of free fermions without the superconductivity instabilities.

5.6 CONCLUSION AND OUTLOOK

We analytically evaluated the entanglement spectra of the superconductivity states on the graphene honeycomb lattice, primarily focusing on the s-wave and chiral $d_{x^2-y^2} + id_{xy}$ superconductivity states. When one spin direction was traced out, exact correspondence between the maximally entangled states of the s-wave superconductor and the zero energies of the noninteracting fermionic honeycomb lattice at finite doping was observed. The relationship between the topologies of the entanglement and subsystem Hamiltonians was found to depend on the coupling between the subsystems. Further, the chiral $d_{x^2-y^2} + id_{xy}$ superconductivity order parameter breaks the time-reversal symmetry in the entanglement Hamiltonian. The topological properties of the entanglement Hamiltonian, characterized by the topological nontrivial entanglement Chern number $C = 1$, clearly differ from those of the time-reversal invariant Hamiltonian of the noninteracting fermions on the honeycomb lattice.

The investigations presented herein are based on closed analytical expressions for the full eigensystems of the s- and d-wave superconductivity states on the honeycomb lattice over the entire Brillouin zone. The method used to examine these eigensystems may constitute a useful tool for new studies of superconductivity in graphene.

Future work may investigate the relationship between the topologies of the entanglement and subsystem Hamiltonians through the topological phase transition; for example, in the coexistence region between antiferromagnetism and $d_{x^2-y^2} + id_{xy}$ superconducting correlations in graphene [Black-Schaffer and Hur, 2015] and graphene bilayers [Milovanović and Predin, 2012].

Superconducting states possess particle-hole symmetry for fermionic excitations. A particle can become a hole by creating a Cooper pair. Hence, the fermionic excitations are expressed by $c_\sigma(\epsilon)$ ($c^\dagger_\sigma(\epsilon)$) being the annihilation (creation) operator of a quasiparticle with energy ϵ and the spin σ. From particle-hole symmetry, we obtain

$$c_\sigma(\epsilon) = c^\dagger_\sigma(-\epsilon) \tag{5.84}$$

$$\lim_{\epsilon\to 0}\left(c_\sigma(\epsilon)\right) = \lim_{\epsilon\to 0}\left(c^\dagger_\sigma(-\epsilon)\right) \tag{5.85}$$

$$c_\sigma(0) = c^\dagger_\sigma(0) \tag{5.86}$$

$$\gamma = \gamma^\dagger. \tag{5.87}$$

Thus, because of the particle-hole symmetry of the superconductivity state, the quasi-particle and its antiparticle are equal at zero energy. This self-conjugate condition is called the Majorana condition, which is satisfied by a class of fermions called Majorana fermions [Sato and Ando, 2017]. A fascinating feature of the Majorana fermions is that they obey non-Abelian statistics, which differs from Abelian statistics. Particles that obey Abelian statistics satisfy the anticommutation relation $\langle \Psi_1 \Psi_2 \rangle = \langle \Psi_2 \Psi_1 \rangle e^{i\phi}$, where $\phi = 0$ denotes bosons and $\phi = \pi$ denotes fermions. Let us now consider N Majorana zero energy modes given by $\gamma_1, \gamma_2, \gamma_3, ..., \gamma_N$. Then, all Majorana fields satisfy

$$\gamma_i^2 = 1, \tag{5.88}$$

$$\gamma_i \gamma_j = -\gamma_j \gamma_i \quad \text{for} \quad i \neq j. \tag{5.89}$$

The non-Abelian statistics is reflected by branding of any pair of Majorana fields.

$$\gamma_i \to \gamma_j, \qquad \gamma_j \to -\gamma_i. \tag{5.90}$$

As we have already seen in this Chapter, the doped graphene can be a chiral $d_{x^2-y^2} + id_{xy}$ superconductor. Graphene, in the presence of the spin-singlet $d_{x^2-y^2} + id_{xy}$ state, could exhibit incredibly rich physics. Because graphene is a two-dimensional material, the possibility of tuning of the Rashba spin-orbit coupling is remarkable and its manipulation could be easier than that in other materials [Min et al., 2006]. For realistic values of the Rashba spin-orbit, in the possible $d_{x^2-y^2} + id_{xy}$ state in doped graphene to the van-Hove singularity point, Majorana fermions could appear at edges by tuning a Zeeman field [Black-Schaffer, 2012]. Furthermore, by increasing the spin-orbit coupling, the $d_{x^2-y^2} + d_{xy}$ superconductor undergoes a topological phase transition from a chiral superconductor to a helical superconductor. In the region where the energy gap is closed, the low energy excitations are Majorana fermions [Sun et al., 2016, Huang et al., 2016]. The Majorana fermion of this system obeys non-Abelian statistics, which is at the heart of the idea of the quantum computer [Nayak et al., 2008]. The Majorana fermions reduce the probability of a random change of the ground state, and this state is very stable to thermal fluctuations. The state obtained by the exchange of two Majorana fermions does not take a simple phase due to the non-Abelian statistics. This corresponds to the manipulations of qubits, which are superposition of $|0\rangle$ and $|1\rangle$. The superposition and entanglement can make a quantum computer operate much faster than a classical one.

The above makes further research on the spin-singlet $d_{x^2-y^2} + id_{xy}$ state, particularly with the Rashba spin-orbit coupling and entanglement, quite interesting.

A

DIAGONALIZATION OF THE BILAYER HAMILTONIAN

Putting $t_4 = 0$ and fixing a wave vector $\vec{k}$ the Hamiltonian (4.1) reads with respect to the basis $\left(a^\dagger_{2\vec{k}}, b^\dagger_{1\vec{k}}, b^\dagger_{2\vec{k}}, a^\dagger_{1\vec{k}}\right)|0\rangle$

$$H = \begin{pmatrix} 0 & t_\perp & -t\gamma(\vec{k}) & 0 \\ t_\perp & 0 & 0 & -t\gamma^*(\vec{k}) \\ -t\gamma^*(\vec{k}) & 0 & 0 & -t_3\gamma(\vec{k}) \\ 0 & -t\gamma(\vec{k}) & -t_3\gamma^*(\vec{k}) & 0 \end{pmatrix}. \tag{A.1}$$

Using $\gamma(\vec{k}) = |\gamma(\vec{k})|e^{i\phi_{\vec{k}}}$ we apply the transformation

$$U_1 = \frac{1}{\sqrt{2}} \begin{pmatrix} 1 & 1 & 0 & 0 \\ 0 & 0 & e^{i\phi_{\vec{k}}} & e^{-i\phi_{\vec{k}}} \\ 0 & 0 & e^{i\phi_{\vec{k}}} & -e^{-i\phi_{\vec{k}}} \\ 1 & -1 & 0 & 0 \end{pmatrix} \tag{A.2}$$

such that in

$$\begin{aligned} H_1 =& U_1 H U_1^\dagger \\ =& \begin{pmatrix} t_\perp & -t|\gamma(\vec{k})| & 0 & 0 \\ -t|\gamma(\vec{k})| & -t_3|\gamma(\vec{k})|\cos\left(3\phi_{\vec{k}}\right) & it_3|\gamma(\vec{k})|\sin\left(3\phi_{\vec{k}}\right) & 0 \\ 0 & -it_3|\gamma(\vec{k})|\sin\left(3\phi_{\vec{k}}\right) & t_3|\gamma(\vec{k})|\cos\left(3\phi_{\vec{k}}\right) & -t|\gamma(\vec{k})| \\ 0 & 0 & -t|\gamma(\vec{k})| & -t_\perp \end{pmatrix} \end{aligned} \tag{A.3}$$

all information on the phase $\phi_{\vec{k}}$ is contained in the matrix elements being proportional to the skew parameter t_3. Proceeding now with the transformation

$$U_2 = \frac{1}{\sqrt{2}} \begin{pmatrix} 1 & -1 & 0 & 0 \\ 1 & 1 & 0 & 0 \\ 0 & 0 & 1 & -1 \\ 0 & 0 & 1 & 1 \end{pmatrix} \tag{A.4}$$

we find

$$H_2 = U_2 H_1 U_2^\dagger = \frac{1}{2} \begin{pmatrix} e_1 & c & -is & -is \\ c & e_2 & is & is \\ is & -is & -e_2 & c \\ is & -is & c & -e_1 \end{pmatrix} \tag{A.5}$$

with

$$e_1 = 2t|\gamma(\vec{k})| + t_\perp - t_3|\gamma(\vec{k})|\cos\left(3\phi_{\vec{k}}\right) , \quad (A.6)$$

$$e_2 = -2t|\gamma(\vec{k})| + t_\perp - t_3|\gamma(\vec{k})|\cos\left(3\phi_{\vec{k}}\right) , \quad (A.7)$$

$$c = t_\perp + t_3|\gamma(\vec{k})|\cos\left(3\phi_{\vec{k}}\right) , \quad (A.8)$$

$$s = t_3|\gamma(\vec{k})|\sin\left(3\phi_{\vec{k}}\right) . \quad (A.9)$$

Here it is useful to split the above matrix as $H_2 = H_2^{'} + H_2^{''}$ where

$$H_2^{'} = \frac{1}{2}\begin{pmatrix} e_1 & 0 & -is & 0 \\ 0 & e_2 & 0 & is \\ is & 0 & -e_2 & 0 \\ 0 & -is & 0 & -e_1 \end{pmatrix}$$

$$H_2^{''} = \frac{1}{2}\begin{pmatrix} 0 & c & 0 & -is \\ c & 0 & is & 0 \\ 0 & -is & 0 & c \\ is & 0 & c & 0 \end{pmatrix} . \quad (A.10)$$

$H_2^{'}$ is diagonalized by

$$U_3 = \begin{pmatrix} \alpha_+ & 0 & -i\sigma\alpha_- & 0 \\ 0 & -i\sigma\alpha_+ & 0 & \alpha_- \\ -i\sigma\alpha_- & 0 & \alpha_+ & 0 \\ 0 & \alpha_- & 0 & -i\sigma\alpha_+ \end{pmatrix} \quad (A.11)$$

with $\sigma = \operatorname{sign}\left(\sin(3\phi(\vec{k}))\right)$ and

$$\alpha_\pm = \sqrt{\frac{1}{2}\left(1 \pm \frac{t_\perp - t_3|\gamma(\vec{k})|\cos\left(3\phi_{\vec{k}}\right)}{\sqrt{t_\perp^2 + t_3^2|\gamma(\vec{k})|^2 - 2t_\perp t_3|\gamma(\vec{k})|\cos\left(3\phi_{\vec{k}}\right)}}\right)} \quad (A.12)$$

such that

$$H_3 = U_3 H_2 U_3^\dagger = \begin{pmatrix} \zeta_1 & id\sigma & 0 & b \\ -id\sigma & \zeta_2 & b & 0 \\ 0 & b & -\zeta_2 & id\sigma \\ b & 0 & -id\sigma & -\zeta_1 \end{pmatrix} \quad (A.13)$$

where

$$d = \frac{\left(t_\perp^2 - t_3^2|\gamma(\vec{k})|^2\right)/2}{\sqrt{t_\perp^2 + t_3^2|\gamma(\vec{k})|^2 - 2t_\perp t_3|\gamma(\vec{k})|\cos\left(3\phi_{\vec{k}}\right)}} , \quad (A.14)$$

$$b = \frac{t_\perp t_3|\gamma(\vec{k})||\sin\left(3\phi_{\vec{k}}\right)|}{\sqrt{t_\perp^2 + t_3^2|\gamma(\vec{k})|^2 - 2t_\perp t_3|\gamma(\vec{k})|\cos\left(3\phi_{\vec{k}}\right)}}\,, \quad \text{(A.15)}$$

and $\pm\zeta_1$ and $\pm\zeta_2$ are eigenvalues of $H_2^{'}$ given by

$$\zeta_{1/2} = \frac{1}{2}\left(\pm 2t|\gamma(\vec{k})| + \sqrt{t_\perp^2 + t_3^2|\gamma(\vec{k})|^2 - 2t_\perp t_3|\gamma(\vec{k})|\cos\left(3\phi_{\vec{k}}\right)}\right)\,. \quad \text{(A.16)}$$

Splitting now H_3 in the form

$$H_3 = \begin{pmatrix} \zeta_1 & id & 0 & 0 \\ -id & \zeta_2 & 0 & 0 \\ 0 & 0 & -\zeta_2 & id \\ 0 & 0 & -id & -\zeta_1 \end{pmatrix} + \begin{pmatrix} 0 & 0 & 0 & b \\ 0 & 0 & b & 0 \\ 0 & b & 0 & 0 \\ b & 0 & 0 & 0 \end{pmatrix} \quad \text{(A.17)}$$

the first part is diagonalized by

$$U_4 = \begin{pmatrix} -i\sigma\tau\beta_+ & \beta_- & 0 & 0 \\ \beta_- & -i\sigma\tau\beta_+ & 0 & 0 \\ 0 & 0 & -i\sigma\tau\beta_+ & \beta_- \\ 0 & 0 & \beta_- & -i\sigma\tau\beta_+ \end{pmatrix} \quad \text{(A.18)}$$

with $\tau = \mathrm{sign}(d)$ and

$$\beta_\pm = \sqrt{\frac{1}{2}\left(1 \pm \frac{\zeta_1 - \zeta_2}{\sqrt{(\zeta_1-\zeta_2)^2 + 4d^2}}\right)} \quad \text{(A.19)}$$

while the second part is left unchanged by U_4 resulting in

$$H_4 = U_4 H_3 U_4^\dagger = \begin{pmatrix} \epsilon_1 & 0 & 0 & b \\ 0 & \epsilon_2 & b & 0 \\ 0 & b & -\epsilon_2 & 0 \\ b & 0 & 0 & -\epsilon_1 \end{pmatrix} \quad \text{(A.20)}$$

with the diagonal elements are given in terms of

$$\epsilon_{1/2} = \frac{1}{2}\left(\zeta_1 + \zeta_2 \pm \sqrt{\left(\zeta_1 - \zeta_2\right)^2 + 4d^2}\right)\,. \quad \text{(A.21)}$$

Finally, H_4 is brought into diagonal form via

$$U_5 = \begin{pmatrix} \gamma_+^{(1)} & 0 & 0 & \gamma_-^{(1)} \\ 0 & \gamma_+^{(2)} & \gamma_-^{(2)} & 0 \\ 0 & \gamma_-^{(2)} & -\gamma_+^{(2)} & 0 \\ \gamma_-^{(1)} & 0 & 0 & -\gamma_+^{(1)} \end{pmatrix} \quad \text{(A.22)}$$

with

$$\gamma_{\pm}^{(1)} = \sqrt{\frac{1}{2}\left(1 \pm \frac{\epsilon_1}{E_2}\right)} \quad , \quad \gamma_{\pm}^{(2)} = \sqrt{\frac{1}{2}\left(1 \pm \frac{\epsilon_2}{E_2}\right)} \tag{A.23}$$

and

$$E_{1/2} = \sqrt{\epsilon_{1,2}^2 + b^2} \tag{A.24}$$

$$= \frac{1}{2}\Bigg[t_{\perp}^2 + t_3^2|\gamma(\vec{k})|^2 + 2t^2|\gamma(\vec{k})|^2$$

$$\pm \sqrt{4t^2|\gamma(\vec{k})|^2\left(t_{\perp}^2 + t_3^2|\gamma(\vec{k})|^2 - 2t_{\perp}t_3|\gamma(\vec{k})|\cos\left(3\phi_{\vec{k}}\right)\right) + \left(t_{\perp}^2 - t_3^2|\gamma(\vec{k})|^2\right)^2}\,\Bigg]. \tag{A.25}$$

Thus,

$$U_5 H_4 U_5^{\dagger} = \operatorname{diag}\left(E_1, E_2, -E_2, -E_1\right) , \tag{A.26}$$

and the matrix elements of the corresponding total transformation $U = U_5U_4U_3U_2U_1$ can be expressed as

$$U_{11} = \frac{1}{2}\left(\alpha_- - i\sigma\alpha_+\right)\left(\tau\beta_+ + \beta_-\right)\left(\gamma_+^{(1)} - i\sigma\gamma_-^{(1)}\right) \tag{A.27}$$

$$U_{12} = \frac{1}{2}\left(\alpha_+ - i\sigma\alpha_-\right)\left(\tau\beta_+ + \beta_-\right)\left(\gamma_-^{(1)} - i\sigma\gamma_+^{(1)}\right) \tag{A.28}$$

$$U_{13} = -\frac{e^{i\phi_{\vec{k}}}}{2}\left(\alpha_- - i\sigma\alpha_+\right)\left(\tau\beta_+ - \beta_-\right)\left(\gamma_+^{(1)} + i\sigma\gamma_-^{(1)}\right) \tag{A.29}$$

$$U_{14} = \frac{e^{-i\phi_{\vec{k}}}}{2}\left(\alpha_- + i\sigma\alpha_+\right)\left(\tau\beta_+ - \beta_-\right)\left(\gamma_+^{(1)} - i\sigma\gamma_-^{(1)}\right) \tag{A.30}$$

and

$$U_{21} = -\frac{1}{2}\left(\alpha_+ + i\sigma\alpha_-\right)\left(\tau\beta_+ - \beta_-\right)\left(\gamma_+^{(2)} - i\sigma\gamma_-^{(2)}\right) \tag{A.31}$$

$$U_{22} = -\frac{1}{2}\left(\alpha_+ - i\sigma\alpha_-\right)\left(\tau\beta_+ - \beta_-\right)\left(\gamma_+^{(2)} + i\sigma\gamma_-^{(2)}\right) \tag{A.32}$$

$$U_{23} = -\frac{e^{i\phi_{\vec{k}}}}{2}\left(\alpha_+ + i\sigma\alpha_-\right)\left(\tau\beta_+ + \beta_-\right)\left(\gamma_+^{(2)} + i\sigma\gamma_-^{(2)}\right) \tag{A.33}$$

$$U_{24} = -\frac{e^{-i\phi_{\vec{k}}}}{2}\left(\alpha_+ - i\sigma\alpha_-\right)\left(\tau\beta_+ + \beta_-\right)\left(\gamma_+^{(2)} - i\sigma\gamma_-^{(2)}\right) \tag{A.34}$$

which are the complex conjugates of the components of the eigenvectors of the conduction-band states with positive energies $E_1(\vec{k})$, $E_2(\vec{k})$, while

$$U_{31} = \frac{1}{2}\left(\alpha_- - i\sigma\alpha_+\right)\left(\tau\beta_+ - \beta_-\right)\left(\gamma_+^{(2)} - i\sigma\gamma_-^{(2)}\right) \tag{A.35}$$

$$U_{32} = \frac{1}{2}\left(\alpha_- + i\sigma\alpha_+\right)\left(\tau\beta_+ - \beta_-\right)\left(\gamma_+^{(2)} + i\sigma\gamma_-^{(2)}\right) \tag{A.36}$$

$$U_{33} = -\frac{e^{i\phi_{\vec{k}}}}{2}\left(\alpha_+ + i\sigma\alpha_-\right)\left(\tau\beta_+ + \beta_-\right)\left(\gamma_-^{(2)} - i\sigma\gamma_+^{(2)}\right) \tag{A.37}$$

$$U_{34} = -\frac{e^{-i\phi_{\vec{k}}}}{2}\left(\alpha_+ - i\sigma\alpha_-\right)\left(\tau\beta_+ + \beta_-\right)\left(\gamma_-^{(2)} + i\sigma\gamma_+^{(2)}\right) \tag{A.38}$$

and

$$U_{41} = \frac{1}{2}\left(\alpha_+ + i\sigma\alpha_-\right)\left(\tau\beta_+ + \beta_-\right)\left(\gamma_+^{(1)} - i\sigma\gamma_-^{(1)}\right) \tag{A.39}$$

$$U_{42} = -\frac{1}{2}\left(\alpha_- + i\sigma\alpha_+\right)\left(\tau\beta_+ + \beta_-\right)\left(\gamma_-^{(1)} - i\sigma\gamma_+^{(1)}\right) \tag{A.40}$$

$$U_{43} = \frac{e^{i\phi_{\vec{k}}}}{2}\left(\alpha_+ + i\sigma\alpha_-\right)\left(\tau\beta_+ - \beta_-\right)\left(\gamma_+^{(1)} + i\sigma\gamma_-^{(1)}\right) \tag{A.41}$$

$$U_{44} = \frac{e^{-i\phi_{\vec{k}}}}{2}\left(\alpha_- + i\sigma\alpha_+\right)\left(\tau\beta_+ - \beta_-\right)\left(\gamma_-^{(1)} + i\sigma\gamma_+^{(1)}\right) \tag{A.42}$$

correspond to the valence-band states with negative energies $(-E_2(\vec{k}))$, $(-E_1(\vec{k}))$. Note that all factors involving $\alpha_\pm$, $\gamma_\pm^{(1)}$, $\gamma_\pm^{(2)}$ in the above expressions have modulus one, i.e. they are phase factors.

B

CORRELATION MATRICES

Upon tracing out layer 1 from the ground state of the undoped bilayer system the correlation matrix reads in the basis $\left(a^\dagger_{2\vec{k}}, b^\dagger_{2\vec{k}}\right)|0\rangle$

$$\begin{aligned} C(\vec{k}) &= \begin{pmatrix} U_{31}U^*_{31} + U_{41}U^*_{41} & U_{31}U^*_{33} + U_{41}U^*_{43} \\ U_{33}U^*_{31} + U_{43}U^*_{41} & U_{33}U^*_{33} + U_{43}U^*_{43} \end{pmatrix} \\ &= \begin{pmatrix} \frac{1}{2} & u(\vec{k}) \\ u^*(\vec{k}) & \frac{1}{2} \end{pmatrix} \end{aligned} \tag{B.1}$$

with

$$u(\vec{k}) = \frac{e^{-i\phi_{\vec{k}}}}{4}\left(\beta_+^2 - \beta_-^2\right)\left(\left(\gamma_+^{(1)} - i\sigma\gamma_-^{(1)}\right)^2 - \left(\gamma_+^{(2)} - i\sigma\gamma_-^{(2)}\right)^2\right). \tag{B.2}$$

This quantity becomes singular at the corners of the Brillouin zone where $\gamma(\vec{k})$ is zero such that its phase is ill-defined, and at the positions of the satellite Dirac cones of the energy spectrum where, as discussed in appendix 4.3, $\gamma_\pm^{(2)}$ is discontinuous.

Tracing out the sublattices A1 and B2 one finds in the basis $\left(a^\dagger_{2\vec{k}}, b^\dagger_{1\vec{k}}\right)|0\rangle$

$$\begin{aligned} C(\vec{k}) &= \begin{pmatrix} U_{31}U^*_{31} + U_{41}U^*_{41} & U_{31}U^*_{32} + U_{41}U^*_{42} \\ U_{32}U^*_{31} + U_{42}U^*_{41} & U_{32}U^*_{32} + U_{42}U^*_{42} \end{pmatrix} \\ &= \begin{pmatrix} \frac{1}{2} & v(\vec{k}) \\ v^*(\vec{k}) & \frac{1}{2} \end{pmatrix} \end{aligned} \tag{B.3}$$

with

$$\begin{aligned} v(\vec{k}) = &\frac{\left(\alpha_- - i\sigma\alpha_+\right)^2}{4}\left(\left(\tau\beta_+ - \beta_-\right)^2\left(\gamma_+^{(2)} - i\sigma\gamma_-^{(2)}\right)^2\right. \\ &\left. + \left(\tau\beta_+ + \beta_-\right)^2\left(\gamma_+^{(1)} - i\sigma\gamma_-^{(1)}\right)^2\right). \end{aligned} \tag{B.4}$$

Note that the expressions (B.2),(B.4) obey the interesting sum rule

$$|u(\vec{k})|^2 + |v(\vec{k})|^2 = \frac{1}{4} \tag{B.5}$$

which s fulfilled whenever the coefficients involved satisfy

$$\alpha_+^2 + \alpha_-^2 = \beta_+^2 + \beta_-^2 = \left(\gamma_+^{(1/2)}\right)^2 + \left(\gamma_-^{(1/2)}\right)^2 = 1\,, \tag{B.6}$$

which is the case here by construction.

Finally, the correlation matrix obtained by tracing out the sublattices A1, A2 is proportional to the unit matrix,

$$\begin{aligned} C(\vec{k}) &= \begin{pmatrix} U_{32}U_{32}^* + U_{42}U_{42}^* & U_{32}U_{33}^* + U_{42}U_{43}^* \\ U_{33}U_{32}^* + U_{43}U_{42}^* & U_{33}U_{33}^* + U_{43}U_{43}^* \end{pmatrix} \\ &= \begin{pmatrix} \frac{1}{2} & 0 \\ 0 & \frac{1}{2} \end{pmatrix} \end{aligned} \tag{B.7}$$

implying that the remaining subsystem is maximally entangled with the subsystem traced out.

C

DIAGONALIZATION OF THE $d+id$-WAVE SUPERCONDUCTIVITY STATE ON THE HONEYCOMB LATTICE

In this Appendix we present analytical diagolazation of the Hamiltonian of the chiral $d+id$-wave superconductivity state on the honeycomb lattice. Complexity of the order parameter makes the analytical approach more difficult. The starting point of our analysis is the Bardeen-Cooper-Schrieffer mean-field Hamiltonian in momentum space is

$$\begin{aligned} H_{MF}(\vec{k}) = & -t\sum_{\vec{k}}\left(\gamma(\vec{k})a^{\dagger}_{\vec{k}\sigma}b_{\vec{k}\sigma}+h.c.\right) \\ & -\mu\sum_{\vec{k}}\left(a^{\dagger}_{\vec{k}\sigma}a_{\vec{k}\sigma}+b^{\dagger}_{\vec{k}\sigma}b_{\vec{k}\sigma}\right) \\ & -J\sum_{\vec{k},\vec{\delta}}\left(\Delta_{\vec{\delta}}e^{i\vec{k}\vec{\delta}}\left(a^{\dagger}_{\vec{k}\uparrow}b^{\dagger}_{-\vec{k}\downarrow}-a^{\dagger}_{\vec{k}\downarrow}b^{\dagger}_{-\vec{k}\uparrow}\right)+h.c.\right) \end{aligned} \tag{C.1}$$

where we define the superconductivity order parameter

$$\Delta(\vec{k}) = \sum_{\vec{\delta}}\Delta_{\vec{\delta}}e^{i\vec{k}\vec{\delta}} \tag{C.2}$$

as a combination of the $d_{x^2-y^2}$ and d_{xy}-wave superconductivity state $\Delta_{d\pm id}(\vec{k}) = \cos\left(\frac{\pi}{3}\right)\Delta_{d^2_x-y^2}(\vec{k}) \pm \sin\left(\frac{\pi}{3}\right)\Delta_{d_{xy}}(\vec{k})$ which minimalizes a free energy.

We apply the transformations

$$\begin{aligned} c_{\vec{k},\sigma} &= \frac{1}{\sqrt{2}}(a_{\vec{k},\sigma} - e^{i\cdot\phi_{\vec{k}}}b_{\vec{k},\sigma}), \\ d_{\vec{k},\sigma} &= \frac{1}{\sqrt{2}}(a_{\vec{k},\sigma} + e^{i\cdot\phi_{\vec{k}}}b_{\vec{k},\sigma}) \end{aligned} \tag{C.3}$$

such that in

$$H_1(\vec{k}) = \begin{pmatrix} t|\gamma(\vec{k})|-\mu & 0 & C_{\vec{k}} & -iS_{\vec{k}} \\ 0 & -t|\gamma(\vec{k})|-\mu & iS_{\vec{k}} & -C_{\vec{k}} \\ C^{*}_{\vec{k}} & -iS^{*}_{\vec{k}} & -t|\gamma(\vec{k})|+\mu & 0 \\ iS^{*}_{\vec{k}} & -C^{*}_{\vec{k}} & 0 & t|\gamma(\vec{k})|+\mu \end{pmatrix}. \tag{C.4}$$

diagonalize the kinetic part of the Hamiltonian. $C_{\vec{k}} = J\sum_{\vec{\delta}}\vec{\Delta}_{\vec{\delta}}\cos(\vec{k}\vec{\delta}-\phi_{\vec{k}})$ and $S_{\vec{k}} = J\sum_{\vec{\delta}}\vec{\Delta}_{\vec{\delta}}\sin(\vec{k}\vec{\delta}-\phi_{\vec{k}})$ are complex functions.

Here it is useful to split this Hamiltonian as $H_1 = H_1^{'} + H_1^{''}$ where

$$H_1^{'}(\vec{k}) = \begin{pmatrix} t|\gamma(\vec{k})| - \mu & 0 & 0 & -iS_{\vec{k}} \\ 0 & -t|\gamma(\vec{k})| - \mu & iS_{\vec{k}} & 0 \\ 0 & -iS^*_{\vec{k}} & -t|\gamma(\vec{k})| + \mu & 0 \\ iS^*_{\vec{k}} & 0 & 0 & t|\gamma(\vec{k})| + \mu \end{pmatrix}. \tag{C.5}$$

and

$$H_1^{''}(\vec{k}) = \begin{pmatrix} 0 & 0 & C_{\vec{k}} & 0 \\ 0 & 0 & 0 & -C_{\vec{k}} \\ C^*_{\vec{k}} & 0 & 0 & 0 \\ 0 & -C^*_{\vec{k}} & 0 & 0 \end{pmatrix}. \tag{C.6}$$

$H_1^{'}$ is diagonalized by

$$e_{\vec{k}+} = i\alpha^*_- c_{\vec{k}\uparrow} + \alpha_+ d^\dagger_{-\vec{k}\downarrow} \tag{C.7}$$

$$f_{\vec{k}+} = -i\alpha^*_- d_{\vec{k}\uparrow} + \alpha_+ c^\dagger_{-\vec{k}\downarrow} \tag{C.8}$$

with

$$\alpha_+ = \sqrt{\frac{1}{2}\left(1 + \frac{\mu}{\sqrt{\mu^2 + |S_{\vec{k}}|^2}}\right)}$$

$$\alpha_- = \frac{S_{\vec{k}}}{\sqrt{2\sqrt{\mu^2 + |S_{\vec{k}}|^2}\left(\mu + \sqrt{\mu^2 + |S_{\vec{k}}|^2}\right)}}. \tag{C.9}$$

This leads to

$$H_2 = U_2 H_1 U_2^\dagger = \begin{pmatrix} e_1 & m & -l & 0 \\ m & e_2 & 0 & l \\ -l^* & 0 & -e_1 & m \\ 0 & l^* & m & -e_2 \end{pmatrix} \tag{C.10}$$

with

$$m = \frac{\mathrm{Re}(C_{\vec{k}}) \cdot \mathrm{Im}(S_{\vec{k}}) - \mathrm{Im}(C_{\vec{k}}) \cdot \mathrm{Re}(S_{\vec{k}})}{\sqrt{\mu^2 + |S_{\vec{k}}|^2}} \tag{C.11}$$

and

$$l = \alpha_+^2 C^*_{\vec{k}} + (\alpha^*_-)^2 C_{\vec{k}} \tag{C.12}$$

and $\pm e_1$ and $\pm e_2$ are eigenenergies of the Hamiltonian $H_1^{'}$ given by

$$e_1 = t|\gamma(\vec{k})| + \sqrt{\mu^2 + |S_{\vec{k}}|^2} \tag{C.13}$$

and

$$e_2 = -t|\gamma(\vec{k})| + \sqrt{\mu^2 + |S_{\vec{k}}|^2}. \tag{C.14}$$

We can now split this Hamiltonian as $H_2 = H_2^{'} + H_2^{''}$ where

$$H_2^{'} = \begin{pmatrix} e_1 & m & 0 & 0 \\ m & e_2 & 0 & 0 \\ 0 & 0 & -e_1 & m \\ 0 & 0 & m & -e_2 \end{pmatrix} \quad , \quad H_2^{''} = \begin{pmatrix} 0 & 0 & -l & 0 \\ 0 & 0 & 0 & l \\ -l^* & 0 & 0 & 0 \\ 0 & l^* & 0 & 0 \end{pmatrix}. \tag{C.15}$$

Proceeding now with the transformations

$$g_{\vec{k}+} = \beta_+ e_{\vec{k}+} + \sigma\beta_- f_{\vec{k}+} \tag{C.16}$$

$$h_{\vec{k}+} = \sigma\beta_- e_{\vec{k}+} - \beta_+ f_{\vec{k}+} \tag{C.17}$$

where $\sigma = \operatorname{sign}(m)$ and

$$\beta_\pm = \sqrt{\frac{1}{2}\left(1 \pm \frac{t|\gamma(\vec{k})|}{\sqrt{t^2|\gamma(\vec{k})|^2 + m^2}}\right)} \tag{C.18}$$

we diagonalize first part of the Hamiltonian $H_2^{'}$ and we get

$$H_3 = U_3 H_2 U_3^\dagger = \begin{pmatrix} \epsilon_1 & 0 & 0 & -l \\ 0 & \epsilon_2 & -l & 0 \\ 0 & -l^* & -\epsilon_2 & 0 \\ -l^* & 0 & 0 & -\epsilon_1 \end{pmatrix} \tag{C.19}$$

where $\pm\epsilon_1$ and $\pm\epsilon_2$ are eigenenergies of the Hamiltonian $H_2^{'}$

$$\epsilon_1 = \sqrt{\mu^2 + |S_{\vec{k}}|^2} + \sqrt{t^2|\gamma(\vec{k})|^2 + m^2} \tag{C.20}$$

and

$$\epsilon_2 = \sqrt{\mu^2 + |S_{\vec{k}}|^2} - \sqrt{t^2|\gamma(\vec{k})|^2 + m^2}. \tag{C.21}$$

Finally, this Hamiltonian is brought to the diagonalized form with transformations

$$o_{\vec{k}+} = \gamma_+^{(1)} g_{\vec{k}+} - \gamma_-^{(1)} g_{\vec{k}-}^\dagger \tag{C.22}$$

$$p_{\vec{k}+} = \gamma_+^{(2)} h_{\vec{k}+} - \gamma_-^{(2)} h_{\vec{k}-}^\dagger \tag{C.23}$$

with

$$\gamma_+^{(1)} = \sqrt{\frac{1}{2}\left(1 + \frac{\epsilon_1}{E_\alpha}\right)} \quad , \quad \gamma_-^{(1)} = \frac{l}{\sqrt{2E_\alpha\left(E_\alpha + \epsilon_1\right)}} \tag{C.24}$$

and

$$\gamma_+^{(2)} = \sqrt{\frac{1}{2}\left(1 + \frac{\epsilon_2}{E_\beta}\right)} \quad , \quad \gamma_-^{(2)} = \frac{l}{\sqrt{2E_\beta\left(E_\beta + \epsilon_2\right)}} \tag{C.25}$$

and

$$E_\alpha = \sqrt{t^2|\gamma(\vec{k})|^2 + \mu^2 + |S_{\vec{k}}|^2 + |C_{\vec{k}}|^2 + 2\sqrt{u+v}} \tag{C.26}$$

and

$$E_\beta = \sqrt{t^2|\gamma(\vec{k})|^2 + \mu^2 + |S_{\vec{k}}|^2 + |C_{\vec{k}}|^2 - 2\sqrt{u+v}}. \tag{C.27}$$

where

$$u = \left(\mu^2 + |S_{\vec{k}}|^2\right) t^2|\gamma(\vec{k})|^2 \tag{C.28}$$

and

$$v = \left(\mathrm{R}e C_{\vec{k}}\mathrm{Im}S_{\vec{k}} - \mathrm{Re}S_{\vec{k}}\mathrm{I}mC_{\vec{k}}\right)^2. \tag{C.29}$$

Bogoliubov transformations $o_{\vec{k}+}$ and $p_{\vec{k}+}$ in the basis $a_{\vec{k}\uparrow}, b_{\vec{k},\uparrow}$

$$\begin{aligned}
o_{\vec{k}+} =& -\frac{1}{\sqrt{2}}\left(\alpha_+\gamma_-^{(1)} - i\alpha_-^*\gamma_+^{(1)}\right)\left(\beta_+ - \sigma\beta_-\right)a_{\vec{k}\uparrow} \\
& - \frac{1}{\sqrt{2}}e^{i\phi_{\vec{k}}}\left(\alpha_+\gamma_-^{(1)} + i\alpha_-^*\gamma_+^{(1)}\right)\left(\beta_+ + \sigma\beta_-\right)b_{\vec{k}\uparrow} \\
& + \frac{1}{\sqrt{2}}\left(\alpha_+\gamma_+^{(1)} + i\alpha_-\gamma_-^{(1)}\right)\left(\beta_+ + \sigma\beta_-\right)a^\dagger_{-\vec{k}\downarrow} \\
& + \frac{1}{\sqrt{2}}e^{i\phi_{\vec{k}}}\left(\alpha_+\gamma_+^{(1)} - i\alpha_-\gamma_-^{(1)}\right)\left(\beta_+ - \sigma\beta_-\right)b^\dagger_{-\vec{k}\downarrow} \qquad \text{(C.30)} \\
p_{\vec{k}+} =& -\frac{1}{\sqrt{2}}\left(\alpha_+\gamma_-^{(2)} + i\alpha_-^*\gamma_+^{(2)}\right)\left(\beta_+ + \sigma\beta_-\right)a_{\vec{k}\uparrow} \\
& + \frac{1}{\sqrt{2}}e^{i\phi_{\vec{k}}}\left(\alpha_+\gamma_-^{(2)} - i\alpha_-^*\gamma_+^{(2)}\right)\left(\beta_+ - \sigma\beta_-\right)b_{\vec{k}\uparrow} \\
& \frac{1}{\sqrt{2}}\left(\alpha_+\gamma_+^{(2)} - i\alpha_-\gamma_-^{(2)}\right)\left(\beta_+ - \sigma\beta_-\right)a^\dagger_{-\vec{k}\downarrow} \\
& - \frac{1}{\sqrt{2}}e^{i\phi_{\vec{k}}}\left(\alpha_+\gamma_+^{(2)} + i\alpha_-\gamma_-^{(2)}\right)\left(\beta_+ + \sigma\beta_-\right)a^\dagger_{-\vec{k}\downarrow} \qquad \text{(C.31)}
\end{aligned}$$

D

CORRELATION MARTIX

D.1 S-WAVE SCENARIO

The Hamiltonian Eq.(5.55) for s-wave superconductivity state in graphene can be diagonalized by using Bogoluibov transformations

$$e_{\vec{k}+} = \alpha_{+}\frac{1}{\sqrt{2}}(a_{\vec{k},\uparrow} - e^{i\cdot\phi_{\vec{k}}}b_{\vec{k},\uparrow}) + \alpha_{-}\frac{1}{\sqrt{2}}(a^{\dagger}_{-\vec{k},\downarrow} - e^{i\cdot\phi_{\vec{k}}}b^{\dagger}_{-\vec{k},\downarrow}) \tag{D.1}$$

$$f_{\vec{k}+} = \beta_{-}\frac{1}{\sqrt{2}}(a_{\vec{k},\uparrow} + e^{i\cdot\phi_{\vec{k}}}b_{\vec{k},\uparrow}) - \beta_{+}\frac{1}{\sqrt{2}}(a^{\dagger}_{-\vec{k},\downarrow} + e^{i\cdot\phi_{\vec{k}}}b^{\dagger}_{-\vec{k},\downarrow}) \tag{D.2}$$

where $\alpha_{+} = \sqrt{\frac{1}{2}\left(1 + \frac{t|\gamma(\vec{k})|-\mu}{\sqrt{\left(t|\gamma(\vec{k})|-\mu\right)^{2}+|C_{\vec{k}}|^{2}}}\right)}$, $\alpha_{-} = \frac{C_{\vec{k}}}{\sqrt{2E_{\alpha}\left(E_{\alpha}+t|\gamma(\vec{k})|-\mu\right)}}$, $\beta_{+} = \sqrt{\frac{1}{2}\left(1 + \frac{t|\gamma(\vec{k})|+\mu}{\sqrt{\left(t|\gamma(\vec{k})|+\mu\right)^{2}+|C_{\vec{k}}|^{2}}}\right)}$, and $\beta_{-} = \frac{C_{\vec{k}}}{\sqrt{2E_{\beta}\left(E_{\beta}+t|\gamma(\vec{k})|+\mu\right)}}$ with E_{α} and E_{β} are energies of Bogoliubov quasi-particles

$$E_{\alpha} = \sqrt{\left(t|\gamma(\vec{k})| - \mu\right)^{2} + |C_{\vec{k}}|^{2}} \tag{D.3}$$

and

$$E_{\beta} = \sqrt{\left(t|\gamma(\vec{k})| + \mu\right)^{2} + |C_{\vec{k}}|^{2}}. \tag{D.4}$$

The e (f) sections are determined by Eq. (D.1) (Eq. (D.2)), respectively. These sections are decoupled in Bogoliubov description and we are allowed than to obtain their contributions to the ground state separative. We can demand $e_{\vec{k}+}|G\rangle = 0$ and $e^{\dagger}_{\vec{k}-}|G\rangle = 0$ where $|G\rangle$ is the ground state. The e section contributes to the ground state as:

$$\prod_{\vec{k}\in IBZ}\left(\alpha_{+}(\vec{k}) - \alpha_{-}(\vec{k})c^{\dagger}_{\vec{k}\uparrow}c^{\dagger}_{-\vec{k}\downarrow}\right)|0\rangle \tag{D.5}$$

where $|0\rangle$ is the vacuum state. Similar, the contribution of the f section to the ground state:

$$\prod_{\vec{k}\in IBZ}\left(\beta_{-}(\vec{k}) + \beta_{+}(\vec{k})d^{\dagger}_{\vec{k}\uparrow}d^{\dagger}_{-\vec{k}\downarrow}\right)|0\rangle \tag{D.6}$$

the ground state $|G\rangle$ is determined by conditions: $f_{\vec{k}+}|G\rangle = 0$ and $f^{\dagger}_{\vec{k}-}|G\rangle = 0$. This leads to the complete ground state vector:

$$\prod_{\vec{k}\in IBZ}\left(\alpha_+(\vec{k}) - \alpha_-(\vec{k})c^{\dagger}_{\vec{k}\uparrow}c^{\dagger}_{-\vec{k}\downarrow}\right) \prod_{\vec{q}\in IBZ}\left(\beta_-(\vec{q}) + \beta_+(\vec{q})d^{\dagger}_{\vec{q}\uparrow}d^{\dagger}_{-\vec{q}\downarrow}\right)|0\rangle. \tag{D.7}$$

Similar findings are obtained for the ground state of the p-wave superconductivity state in graphene.

This ground state leads to the correlation matrix when spin ↓ is traced out:

$$C(\vec{k}) = \begin{pmatrix} \frac{1}{2}\left(|\alpha_-|^2 + |\beta_+|^2\right) & \frac{1}{2}e^{-i\phi_{\vec{k}}}\left(|\beta_+|^2 - |\alpha_-|^2\right) \\ \frac{1}{2}e^{i\phi_{\vec{k}}}\left(|\beta_+|^2 - |\alpha_-|^2\right) & \frac{1}{2}\left(|\alpha_-|^2 + |\beta_+|^2\right) \end{pmatrix}. \tag{D.8}$$

D.2 CHIRAL D-WAVE SCENARIO

Here, o section is defined by Eq. (C.30), while p section is defined by Eq. (C.31). We can consider o and p sections separative. Thus, the o section contributes to the ground state as

$$\prod_{\vec{k}\in IBZ}\left(\gamma^{(1)}_+(\vec{k}) + \gamma^{(1)}_-(\vec{k})g^{\dagger}_{\vec{k}+}g^{\dagger}_{-\vec{k}-}\right)|0\rangle \tag{D.9}$$

where $|0\rangle$ is the vacuum state. While, the p section contributes to the ground state

$$\prod_{\vec{k}\in IBZ}\left(\gamma^{(2)}_+(\vec{k}) + \gamma^{(2)}_-(\vec{k})h^{\dagger}_{\vec{k}+}h^{\dagger}_{-\vec{k}-}\right)|0\rangle. \tag{D.10}$$

The complete ground state vector $|G\rangle$ can be determined by conditions $g_{\vec{k}+}|G\rangle = 0$ and $g^{\dagger}_{\vec{k}-}|G\rangle = 0$ and $h_{\vec{k}+}|G\rangle = 0$ and $h^{\dagger}_{\vec{k}-}|G\rangle = 0$, which leads to the following form

$$\prod_{\vec{k}\in IBZ}\left(\gamma^{(1)}_+(\vec{k}) + \gamma^{(1)}_-(\vec{k})g^{\dagger}_{\vec{k}+}g^{\dagger}_{-\vec{k}-}\right)\prod_{\vec{q}\in IBZ}\left(\gamma^{(2)}_+(\vec{q}) + \gamma^{(2)}_-(\vec{q})h^{\dagger}_{\vec{q}+}h^{\dagger}_{-\vec{q}-}\right)|0\rangle. \tag{D.11}$$

Using

$$a_{\vec{k}\uparrow} = -\frac{1}{\sqrt{2}}\left(\alpha_+\left(\gamma^{(1)}_-\right)^* + i\alpha_-\gamma^{(1)}_+\right)\left(\beta_+ - \sigma\beta_-\right)o_{\vec{k},+}$$

$$\begin{aligned}
&-\frac{1}{\sqrt{2}}\left(\alpha_+\left(\gamma_-^{(2)}\right)^* + i\alpha_-\gamma_+^{(2)}\right)\left(\beta_+ + \sigma\beta_-\right) p_{\vec{k},+} \\
&+\frac{1}{\sqrt{2}}\left(\alpha_+\gamma_+^{(2)} - i\alpha_-\gamma_-^{(2)}\right)\left(\beta_+ + \sigma\beta_-\right) p^\dagger_{-\vec{k},-} \\
&+\frac{1}{\sqrt{2}}\left(\alpha_+\gamma_+^{(1)} - i\alpha_-\gamma_-^{(1)}\right)\left(\beta_+ - \sigma\beta_-\right) o^\dagger_{-\vec{k},-} \qquad \text{(D.12)}
\end{aligned}$$

we can calculate the mean occupancy at cite A:

$$\begin{aligned}
\langle a^\dagger_{\vec{k}\uparrow} a_{\vec{k}\uparrow}\rangle = {} & \\
&\frac{1}{2}\left(\alpha_+^2|\gamma_-^{(1)}|^2 + |\alpha_-|^2\left(\gamma_+^{(1)}\right)^2 + i\alpha_+\gamma_+^{(1)}\left(\alpha_-\gamma_-^{(1)} - \alpha_-^*\left(\gamma_-^{(1)}\right)^*\right)\right) \\
&\left(\beta_+ - \sigma\beta_-\right)^2 n^{(0)}_{\vec{k}} \\
&+\frac{1}{2}\left(\alpha_+^2|\gamma_-^{(2)}|^2 + |\alpha_-|^2\left(\gamma_+^{(2)}\right)^2 + i\alpha_+\gamma_+^{(2)}\left(\alpha_-\gamma_-^{(2)} - \alpha_-^*\left(\gamma_-^{(2)}\right)^*\right)\right) \\
&\left(\beta_+ + \sigma\beta_-\right)^2 n^{(0)}_{\vec{k}} \\
&+\frac{1}{2}\left(\alpha_+^2(\gamma_+^{(1)})^2 + |\alpha_-|^2|\gamma_-^{(1)}|^2 - i\alpha_+\gamma_+^{(1)}\left(\alpha_-\gamma_-^{(1)} - \alpha_-^*\left(\gamma_-^{(1)}\right)^*\right)\right) \\
&\left(\beta_+ - \sigma\beta_-\right)^2 (1 - n^{(0)}_{\vec{k}}) \\
&+\frac{1}{2}\left(\alpha_+^2(\gamma_+^{(2)})^2 + |\alpha_-|^2|\gamma_-^{(2)}|^2 - i\alpha_+\gamma_+^{(2)}\left(\alpha_-\gamma_-^{(2)} - \alpha_-^*\left(\gamma_-^{(2)}\right)^*\right)\right) \\
&\left(\beta_+ + \sigma\beta_-\right)^2 (1 - n^{(0)}_{\vec{k}}). \qquad \text{(D.13)}
\end{aligned}$$

The average number $n^{(0)}_{\vec{k}}$ of fermions with momentum k at temperature $T = 0$ is $n^{(0)}_{\vec{k}} = 0$.

Further, we get the mean occupancy at the cite A

$$\begin{aligned}
\langle a^\dagger_{\vec{k}\uparrow} a_{\vec{k}\uparrow}\rangle = {} & \frac{1}{2}\left(\alpha_+^2(\gamma_+^{(1)})^2 + |\alpha_-|^2|\gamma_-^{(1)}|^2 - i\alpha_+\gamma_+^{(1)}\left(\alpha_-\gamma_-^{(1)} - \alpha_-^*\left(\gamma_-^{(1)}\right)^*\right)\right) \\
&\left(\beta_+ - \sigma\beta_-\right)^2 \\
&+\frac{1}{2}\left(\alpha_+^2(\gamma_+^{(2)})^2 + |\alpha_-|^2|\gamma_-^{(2)}|^2 - i\alpha_+\gamma_+^{(2)}\left(\alpha_-\gamma_-^{(2)} - \alpha_-^*\left(\gamma_-^{(2)}\right)^*\right)\right) \\
&\left(\beta_+ + \sigma\beta_-\right)^2. \qquad \text{(D.14)}
\end{aligned}$$

After basic algebra we find that the correlation matrix obtained by tracing out spin ↓ at $T = 0$ reads

$$C(\vec{k}) = \begin{pmatrix} C_{11}(\vec{k}) & C_{12}(\vec{k}) \\ C_{12}^*(\vec{k}) & C_{22}(\vec{k}) \end{pmatrix} \qquad \text{(D.15)}$$

with

$$\begin{aligned}
&C_{11}(\vec{k}) = \frac{1}{2}\left(\alpha_+^2(\gamma_+^{(1)})^2 + |\alpha_-|^2|\gamma_-^{(1)}|^2 - i\alpha_+\gamma_+^{(1)}\left(\alpha_-\gamma_-^{(1)} - \alpha_-^*\left(\gamma_-^{(1)}\right)^*\right)\right)\\
&(\beta_+ - \sigma\beta_-)^2\\
&+\frac{1}{2}\left(\alpha_+^2(\gamma_+^{(2)})^2 + |\alpha_-|^2|\gamma_-^{(2)}|^2 - i\alpha_+\gamma_+^{(2)}\left(\alpha_-\gamma_-^{(2)} - \alpha_-^*\left(\gamma_-^{(2)}\right)^*\right)\right)\\
&(\beta_+ + \sigma\beta_-)^2\\
&= \frac{1}{2} + \frac{1}{4}\frac{\mu}{\sqrt{\mu^2+|S_{\vec{k}}|^2}}(\epsilon_1+m)\frac{1}{E_\alpha}\left(1 - \frac{m}{\sqrt{t^2|\gamma(\vec{k})|^2+m^2}}\right)\\
&+\frac{1}{4}\frac{\mu}{\sqrt{\mu^2+|S_{\vec{k}}|^2}}(\epsilon_2+m)\frac{1}{E_\beta}\left(1 + \frac{m}{\sqrt{t^2|\gamma(\vec{k})|^2+m^2}}\right),
\end{aligned}\tag{D.16}$$

$$\begin{aligned}
&C_{22}(\vec{k}) = \frac{1}{2}\left(\alpha_+^2(\gamma_+^{(1)})^2 + |\alpha_-|^2|\gamma_-^{(1)}|^2 + i\alpha_+\gamma_+^{(1)}\left(\alpha_-\gamma_-^{(1)} - \alpha_-^*\left(\gamma_-^{(1)}\right)^*\right)\right)\\
&(\beta_+ + \sigma\beta_-)^2\\
&+\frac{1}{2}\left(\alpha_+^2(\gamma_+^{(2)})^2 + |\alpha_-|^2|\gamma_-^{(2)}|^2 + i\alpha_+\gamma_+^{(2)}\left(\alpha_-\gamma_-^{(2)} - \alpha_-^*\left(\gamma_-^{(2)}\right)^*\right)\right)\\
&(\beta_+ - \sigma\beta_-)^2\\
&= \frac{1}{2} + \frac{1}{4}\frac{\mu}{\sqrt{\mu^2+|S_{\vec{k}}|^2}}(\epsilon_1-m)\frac{1}{E_\alpha}\left(1 + \frac{m}{\sqrt{t^2|\gamma(\vec{k})|^2+m^2}}\right)\\
&+\frac{1}{4}\frac{\mu}{\sqrt{\mu^2+|S_{\vec{k}}|^2}}(\epsilon_2-m)\frac{1}{E_\beta}\left(1 - \frac{m}{\sqrt{t^2|\gamma(\vec{k})|^2+m^2}}\right),
\end{aligned}\tag{D.17}$$

and

$$\begin{aligned}
&C_{12}(\vec{k}) =\\
&\frac{1}{2}e^{-i\phi_{\vec{k}}}\left(\alpha_+^2(\gamma_+^{(1)})^2 - |\alpha_-|^2|\gamma_-^{(1)}|^2 - i\alpha_+\gamma_+^{(1)}\left(\alpha_-^{(1)}\gamma_-^{(1)} + \left(\alpha_-^{(1)}\right)^*\left(\gamma_-^{(1)}\right)^*\right)\right)\\
&\left(\beta_+^2 - \beta_-^2\right)\\
&-\frac{1}{2}e^{-i\phi_{\vec{k}}}\left(\alpha_+^2(\gamma_+^{(2)})^2 - |\alpha_-|^2|\gamma_+^{(2)}|^2 - i\alpha_+\gamma_+^{(2)}\left(\alpha_-^{(1)}\gamma_-^{(2)} + \left(\alpha_-^{(1)}\right)^*\left(\gamma_-^{(2)}\right)^*\right)\right)\\
&\left(\beta_+^2 - \beta_-^2\right)\\
&= \frac{1}{4}e^{-i\phi_{\vec{k}}}\left(\left(\frac{\epsilon_1}{E_\alpha} - \frac{\epsilon_2}{E_\beta}\right) - i\frac{\mathrm{Re}(C_{\vec{k}})\mathrm{Re}(S_{\vec{k}}) + \mathrm{Im}(C_{\vec{k}})\mathrm{Im}(S_{\vec{k}})}{\sqrt{\mu^2+\ |S_{\vec{k}}|^2}}\left(\frac{1}{E_\alpha} - \frac{1}{E_\beta}\right)\right)\\
&\frac{t|\gamma(\vec{k})|}{\sqrt{t^2|\gamma(\vec{k})|^2+m^2}}.
\end{aligned}\tag{D.18}$$

Here, one should notice that $C_{11}(-\vec{k}) = C_{22}(\vec{k})$ and $C_{12}(\vec{k}) = \left(C_{12}(-\vec{k})\right)^*$.

Eigenvectors of the correlation matrix

$$\begin{aligned} q_{\vec{k}\uparrow} =& \delta_+(\vec{k}) a_{\vec{k}\uparrow} + \delta_-(\vec{k}) b_{\vec{k}\uparrow} && \text{(D.19)} \\ r_{\vec{k}\uparrow} =& \delta_+(-\vec{k}) a_{\vec{k}\uparrow} - \delta_-^*(-\vec{k}) b_{\vec{k}\uparrow} && \text{(D.20)} \end{aligned}$$

where:

$$\begin{aligned} \delta_+(\vec{k}) =& \sqrt{\frac{1}{2}\left(1 + \frac{C_{11} - C_{22}}{\sqrt{\left(C_{11} - C_{22}\right)^2 + 4|C_{12}|^2}}\right)} \\ \delta_-(\vec{k}) =& \frac{2C_{12}}{\sqrt{2\sqrt{\left(C_{11} - C_{22}\right)^2 + 4|C_{12}|^2}(C_{11} - C_{22} + \sqrt{d})}}. \end{aligned} \quad \text{(D.21)}$$

BIBLIOGRAPHY

[Alba et al., 2012] Alba, V., Haque, M., and Läuchli, A. M. (2012). Boundary-locality and perturbative structure of entanglement spectra in gapped systems. *Phys. Rev. Lett.*, 108:227201. (Cited on page 3.)

[Altland and Zirnbauer, 1997] Altland, A. and Zirnbauer, M. R. (1997). Nonstandard symmetry classes in mesoscopic normal-superconducting hybrid structures. *Phys. Rev. B*, 55:1142–1161. (Cited on page 69.)

[Amico et al., 2008] Amico, L., Fazio, R., Osterloh, A., and Vedral, V. (2008). Entanglement in many-body systems. *Rev. Mod. Phys.*, 80:517–576. (Cited on page 19.)

[Ansmann et al., 2009] Ansmann, M., Wang, H., Bialczak, R. C., Hofheinz, M., Lucero, E., Neeley, M., O'Connell, A. D., Sank, D., Weides, M., Wenner, J., Cleland, A. N., and Martinis, J. M. (2009). Violation of bell's inequality in josephson phase qubits. *Nature*, 461:504. (Cited on page 2.)

[Ardonne and Regnault, 2011] Ardonne, E. and Regnault, N. (2011). Structure of spinful quantum hall states: A squeezing perspective. *Phys. Rev. B*, 84:205134. (Cited on page 3.)

[Ashcroft and Mermin, 1976] Ashcroft, N. and Mermin, D. (1976). *Solid State Physics.* Harcourt College Publishers. (Cited on page 12.)

[Aspect et al., 1982] Aspect, A., Dalibard, J., and Roger, G. (1982). Experimental test of bell's inequalities using time-varying analyzers. *Phys. Rev. Lett.*, 49:1804. (Cited on page 2.)

[Auerbach, 1994] Auerbach, A. (1994). *Interacting Electrons and Quantum Magnetism.* Springer. (Cited on page 58.)

[Barrett et al., 2002] Barrett, J., Collins, D., Hardy, L., Kent, A., and Popescu, S. (2002). Quantum nonlocality, bell inequalities, and the memory loophole. *Phys. Rev. A*, 66:042111. (Cited on page 2.)

[Baskaran and Jafari, 2002] Baskaran, G. and Jafari, S. A. (2002). Gapless spin-1 neutral collective mode branch for graphite. *Phys. Rev. Lett.*, 89:016402. (Cited on page 59.)

[Bell, 2004] Bell, J. S. (2004). *Speakable and Unspeakable in Quantum Mechanics: Collected Papers on Quantum Philosophy.* Cambridge University Press. (Cited on pages 1 and 2.)

[Bena and Kivelson, 2005] Bena, C. and Kivelson, S. A. (2005). Quasiparticle scattering and local density of states in graphite. *Phys. Rev. B*, 72:125432. (Cited on page 16.)

[Black-Schaffer, 2012] Black-Schaffer, A. M. (2012). Edge properties and majorana fermions in the proposed chiral *d*-wave superconducting state of doped graphene. *Phys. Rev. Lett.*, 109:197001. (Cited on page 77.)

[Black-Schaffer and Doniach, 2007] Black-Schaffer, A. M. and Doniach, S. (2007). Resonating valence bonds and mean-field *d*-wave superconductivity in graphite. *Phys. Rev. B*, 75:134512. (Cited on pages 5 and 53.)

[Black-Schaffer and Honerkamp, 2014] Black-Schaffer, A. M. and Honerkamp, C. (2014). Chiral d -wave superconductivity in doped graphene. *Journal of Physics: Condensed Matter*, 26:423201. (Cited on pages 53, 54, and 55.)

[Black-Schaffer and Hur, 2015] Black-Schaffer, A. M. and Hur, K. L. (2015). Topological superconductivity in two dimensions with mixed chirality. *Phys. Rev. B*, 32:140503(R). (Cited on page 76.)

[Black-Schaffer et al., 2014] Black-Schaffer, A. M., Wu, W., and Le Hur, K. (2014). Chiral *d*-wave superconductivity on the honeycomb lattice close to the mott state. *Phys. Rev. B*, 90:054521. (Cited on page 64.)

[Bombelli et al., 1986] Bombelli, L., Koul, R. K., Lee, J., and Sorkin, R. D. (1986). Quantum source of entropy for black holes. *Phys. Rev. D*, 34:373–383. (Cited on page 2.)

[Borchmann et al., 2014] Borchmann, J., Farrell, A., Matsuura, S., and Pereg-Barnea, T. (2014). Entanglement spectrum as a probe for the topology of a spin-orbit-coupled superconductor. *Phys. Rev. B*, 90:235150. (Cited on pages 3 and 69.)

[Bray-Ali et al., 2009] Bray-Ali, N., Ding, L., and Haas, S. (2009). Topological order in paired states of fermions in two-dimensions with breaking of parity and time-reversal symmetries. *Phys. Rev. B*, 80:180504. (Cited on page 3.)

[Castro Neto et al., 2009] Castro Neto, A. H., Guinea, F., Peres, N. M. R., Novoselov, K. S., and Geim, A. K. (2009). The electronic properties of graphene. *Rev. Mod. Phys.*, 81:109–162. (Cited on page 10.)

[Chandran et al., 2011] Chandran, A., Hermanns, M., Regnault, N., and Bernevig, B. A. (2011). Bulk-edge correspondence in entanglement spectra. *Phys. Rev. B*, 84:205136. (Cited on page 3.)

[Chandran et al., 2014] Chandran, A., Khemani, V., and Sondhi, S. L. (2014). How universal is the entanglement spectrum? *Phys. Rev. Lett.*, 113:060501. (Cited on page 4.)

[Chapman et al., 2016] Chapman, J., Su, Y., Howard, C. A., Kundys, D., Grigorenko, A. N., Guinea, F., Geim, A. K., Grigorieva, I. V., and Nair, R. R. (2016). Superconductivity in ca-doped graphene laminates. *Scientific Reports*, 6:23254. (Cited on page 54.)

[Chen and Fradkin, 2013] Chen, X. and Fradkin, E. (2013). Quantum entanglement and thermal reduced density matrices in fermion and spin systems on ladders. *Journal of Statistical Mechanics: Theory and Experiment*, 2013(08):P08013. (Cited on page 4.)

[Cheong and Henley, 2004] Cheong, S.-A. and Henley, C. L. (2004). Many-body density matrices for free fermions. *Phys. Rev. B*, 69:075111. (Cited on pages 6, 20, 24, 45, and 69.)

[Cirac et al., 2011] Cirac, J. I., Poilblanc, D., Schuch, N., and Verstraete, F. (2011). Entanglement spectrum and boundary theories with projected entangled-pair states. *Phys. Rev. B*, 83:245134. (Cited on pages 4 and 19.)

[Cosma and Fal'ko, 2015] Cosma, D. A. and Fal'ko, V. I. (2015). Trigonal warping effect on velocity and transverse confinement length of topologically confined states in bilayer graphene. *Phys. Rev. B*, 92:165412. (Cited on page 40.)

[Cserti et al., 2007] Cserti, J., Csordás, A., and Dávid, G. (2007). Role of the trigonal warping on the minimal conductivity of bilayer graphene. *Phys. Rev. Lett.*, 99:066802. (Cited on page 40.)

[De Chiara et al., 2012] De Chiara, G., Lepori, L., Lewenstein, M., and Sanpera, A. (2012). Entanglement spectrum, critical exponents, and order parameters in quantum spin chains. *Phys. Rev. Lett.*, 109:237208. (Cited on page 4.)

[Drut and Lähde, 2009] Drut, J. E. and Lähde, T. A. (2009). Is graphene in vacuum an insulator? *Phys. Rev. Lett.*, 102:026802. (Cited on page 53.)

[Dubail and Read, 2011] Dubail, J. and Read, N. (2011). Entanglement spectra of complex paired superfluids. *Phys. Rev. Lett.*, 107:157001. (Cited on page 4.)

[Dubail et al., 2012] Dubail, J., Read, N., and Rezayi, E. H. (2012). Real-space entanglement spectrum of quantum hall systems. *Phys. Rev. B*, 85:115321. (Cited on page 3.)

[Eberhard, 1993] Eberhard, P. (1993). Background level and counter efficiencies required for a loophole-free einstein-podolsky-rosen experiment. *Phys. Rev. A*, 47:747. (Cited on page 2.)

[Einstein et al., 1935] Einstein, A., Podolsky, B., and N.Rosen (1935). Can quantum-mechanical description of physical reality be considered complete? *Phys. Rev.*, 47:777. (Cited on page 1.)

[Eisert et al., 2010] Eisert, J., Cramer, M., and Plenio, M. B. (2010). *Colloquium* : Area laws for the entanglement entropy. *Rev. Mod. Phys.*, 82:277. (Cited on page 3.)

[Feynman, 1982] Feynman, R. (1982). Simulating physics with computers. *International Journal of Theoretical Physics*, 21:467–488. (Cited on page 2.)

[Fidkowski, 2010] Fidkowski, L. (2010). Entanglement spectrum of topological insulators and superconductors. *Phys. Rev. Lett.*, 104:130502. (Cited on page 3.)

[Freedman and Clauser, 1972] Freedman, S. J. and Clauser, J. F. (1972). Experimental test of local hidden-variable theories. *Phys. Rev. Lett.*, 28:938. (Cited on page 2.)

[Fukui and Hatsugai, 2014] Fukui, T. and Hatsugai, Y. (2014). Entanglement chern number for an extensive partition of a topological ground state. *Journal of the Physical Society of Japan*, 83:113705. (Cited on page 39.)

[Gamayun et al., 2010] Gamayun, O. V., Gorbar, E. V., and Gusynin, V. P. (2010). Gap generation and semimetal-insulator phase transition in graphene. *Phys. Rev. B*, 81:075429. (Cited on page 53.)

[Garg and Mermin, 1987] Garg, A. and Mermin, N. D. (1987). Detector inefficiencies in the einstein-podolsky-rosen experiment. *Phys. Rev. D*, 35:3831. (Cited on page 2.)

[Goerbig, 2011] Goerbig, M. O. (2011). Electronic properties of graphene in a strong magnetic field. *Rev. Mod. Phys.*, 83:1193–1243. (Cited on page 13.)

[Hensen et al., 2015] Hensen, B., Bernien, H., Dreau, A. E., Reiserer, A., Kalb, N., Blok, M. S., Ruitenberg, J., Vermeulen, R. F. L., Schouten, R. N., Abellan, C., Amaya, W., Pruneri, V., Mitchell, M. W., Markham, M., Twitchen, D. J., Elkouss, D., Wehner, S., Taminiau, T. H., and Hanson, R. (2015). Loophole-free bell inequality violation using electron spins separated by 1.3 kilometres. *Nature*, 526:682. (Cited on page 2.)

[Herbut, 2006] Herbut, I. F. (2006). Interactions and phase transitions on graphene's honeycomb lattice. *Phys. Rev. Lett.*, 97:146401. (Cited on page 53.)

[Herbut et al., 2009] Herbut, I. F., Juričić, V., and Roy, B. (2009). Theory of interacting electrons on the honeycomb lattice. *Phys. Rev. B*, 79:085116. (Cited on page 53.)

[Hermanns et al., 2011] Hermanns, M., Chandran, A., Regnault, N., and Bernevig, B. A. (2011). Haldane statistics in the finite-size entanglement spectra of 1/m fractional quantum hall states. *Phys. Rev. B*, 84:121309. (Cited on page 3.)

[Honerkamp, 2008] Honerkamp, C. (2008). Density waves and cooper pairing on the honeycomb lattice. *Phys. Rev. Lett.*, 100:146404. (Cited on page 53.)

[Hou et al., 2007] Hou, C.-Y., Chamon, C., and Mudry, C. (2007). Electron fractionalization in two-dimensional graphene-like structures. *Phys. Rev. Lett.*, 98:186809. (Cited on page 53.)

[Huang and Lin, 2011] Huang, C.-Y. and Lin, F.-L. (2011). Topological order and degenerate singular value spectrum in two-dimensional dimerized quantum heisenberg model. *Phys. Rev. B*, 84:125110. (Cited on page 4.)

[Huang et al., 2016] Huang, S.-M., Tsai, W.-F., Chung, C.-H., and Mou, C.-Y. (2016). Duality in topological superconductors and topological ferromagnetic insulators in a honeycomb lattice. *Phys. Rev. B*, 93:054518. (Cited on page 77.)

[Ichinokura et al., 2016] Ichinokura, S., Sugawara, K., Takayama, A., Takahashi, T., and Hasegawa, S. (2016). Superconducting calcium-intercalated bilayer graphene. *ACS Nano*, 10:2761–2765. (Cited on page 54.)

[Katsnelson et al., 2006] Katsnelson, M. I., Novoselov, K. S., and Geim, A. K. (2006). Chiral tunnelling and the klein paradox in graphene. *Nature Physics*, 2:620–625. (Cited on page 10.)

[Kechedzhi et al., 2007] Kechedzhi, K., Fal'ko, V. I., McCann, E., and Altshuler, B. L. (2007). Influence of trigonal warping on interference effects in bilayer graphene. *Phys. Rev. Lett.*, 98:176806. (Cited on page 40.)

[Khveshchenko, 2001] Khveshchenko, D. V. (2001). Ghost excitonic insulator transition in layered graphite. *Phys. Rev. Lett.*, 87:246802. (Cited on page 53.)

[Kiesel et al., 2012] Kiesel, M., Platt, C., Hanke, W., Abanin, D. A., and Thomale, R. (2012). Competing many-body instabilities and unconventional superconductivity in graphene. *Phys. Rev. B*, 86:020507(R). (Cited on pages 53 and 56.)

[Kim, 2014] Kim, E. H. (2014). Characterizing topological order in superconductors via entanglement. *Journal of Physics: Condensed Matter*, 26:205602. (Cited on pages 3 and 69.)

[Koshino and Ando, 2006] Koshino, M. and Ando, T. (2006). Transport in bilayer graphene: Calculations within a self-consistent born approximation. *Phys. Rev. B*, 73:245403. (Cited on page 40.)

[Kuzmenko et al., 2009] Kuzmenko, A. B., Crassee, I., van der Marel, D., Blake, P., and Novoselov, K. S. (2009). Determination of the gate-tunable band gap and tight-binding parameters in bilayer graphene using infrared spectroscopy. *Phys. Rev. B*, 80:165406. (Cited on page 21.)

[Laflorencie, 2016] Laflorencie, N. (2016). Quantum entanglement in condensed matter systems. *Physics Reports*, 646:1 – 59. (Cited on page 4.)

[Landau and Lifshitz, 1980] Landau, L. D. and Lifshitz, E. M. (1980). *Statistical Physics*. Pergamon, Oxford. (Cited on page 9.)

[Läuchli et al., 2010] Läuchli, A. M., Bergholtz, E. J., Suorsa, J., and Haque, M. (2010). Disentangling entanglement spectra of fractional quantum hall states on torus geometries. *Phys. Rev. Lett.*, 104:156404. (Cited on page 3.)

[Läuchli and Schliemann, 2012] Läuchli, A. M. and Schliemann, J. (2012). Entanglement spectra of coupled $s = \frac{1}{2}$ spin chains in a ladder geometry. *Phys. Rev. B*, 85:054403. (Cited on pages 4 and 19.)

[Li and Haldane, 2008] Li, H. and Haldane, F. D. M. (2008). Entanglement spectrum as a generalization of entanglement entropy: Identification of topological order in non-abelian fractional quantum hall effect states. *Phys. Rev. Lett.*, 101:010504. (Cited on page 3.)

[Liu et al., 2009] Liu, G.-Z., Li, W., and Cheng, G. (2009). Interaction and excitonic insulating transition in graphene. *Phys. Rev. B*, 79:205429. (Cited on page 53.)

[Liu et al., 2012] Liu, Z., Bergholtz, E. J., Fan, H., and Läuchli, A. M. (2012). Edge-mode combinations in the entanglement spectra of non-abelian fractional quantum hall states on the torus. *Phys. Rev. B*, 85:045119. (Cited on page 3.)

[Lou et al., 2011] Lou, J., Tanaka, S., Katsura, H., and Kawashima, N. (2011). Entanglement spectra of the two-dimensional affleck-kennedy-lieb-tasaki model: Correspondence between the valence-bond-solid state and conformal field theory. *Phys. Rev. B*, 84:245128. (Cited on page 4.)

[Ludbrook et al., 2015] Ludbrook, B. M., Levy, G., Nigge, P., Zonno, M., Schneider, M., Dvorak, D. J., Veenstra, C. N., Zhdanovich, S., Wong, D., Dosanjh, P., Straßer, C., Stöhr, A., Forti, S., Ast, C. R., Starke, U., and Damascelli, A. (2015). Evidence for superconductivity in li-decorated monolayer graphene. *Proceedings of the National Academy of Sciences*, 112:11795–11799. (Cited on page 54.)

[Lundgren, 2016] Lundgren, R. (2016). Momentum-space entanglement in heisenberg spin-half ladders. *Phys. Rev. B*, 93:125107. (Cited on page 4.)

[Lundgren et al., 2014] Lundgren, R., Blair, J., Greiter, M., Läuchli, A., Fiete, G. A., and Thomale, R. (2014). Momentum-space entanglement spectrum of bosons and fermions with interactions. *Phys. Rev. Lett.*, 113:256404. (Cited on page 4.)

[Lundgren et al., 2012] Lundgren, R., Chua, V., and Fiete, G. A. (2012). Entanglement entropy and spectra of the one-dimensional kugel-khomskii model. *Phys. Rev. B*, 86:224422. (Cited on pages 4, 5, and 39.)

[Lundgren et al., 2013] Lundgren, R., Fuji, Y., Furukawa, S., and Oshikawa, M. (2013). Entanglement spectra between coupled tomonaga-luttinger liquids: Applications to ladder systems and topological phases. *Phys. Rev. B*, 88:245137. (Cited on page 4.)

[Manes et al., 2007] Manes, J. L., Guinea, F., and Vozmediano, M. A. H. (2007). Existence and topological stability of fermi points in multilayered graphene. *Phys. Rev. B*, 75:155424. (Cited on pages 40 and 45.)

[Mariani et al., 2012] Mariani, E., Pearce, A. J., and von Oppen, F. (2012). Fictitious gauge fields in bilayer graphene. *Phys. Rev. B*, 86:165448. (Cited on pages 40, 43, and 45.)

[Matsukevich et al., 2008] Matsukevich, N. D., Maunz, P., Moehring, D. L., Olmschenk, S., and Monroe, C. (2008). Bell inequality violation with two remote atomic qubits. *Phys. Rev. Lett.*, 100:150404. (Cited on page 2.)

[McCann and Fal'ko, 2006] McCann, E. and Fal'ko, V. I. (2006). Landau-level degeneracy and quantum hall effect in a graphite bilayer. *Phys. Rev. Lett.*, 96:086805. (Cited on pages 23, 40, 42, 44, and 51.)

[McCann and Koshino, 2013] McCann, E. and Koshino, M. (2013). The electronic properties of bilayer graphene. *Reports on Progress in Physics*, 76:056503. (Cited on pages 5, 13, 19, 20, 39, 40, and 43.)

[Meng et al., 2010] Meng, Z. Y., Lang, T. C., Wessel, S., Assaad, F. F., and Muramatsu, A. (2010). Quantum spin liquid emerging in two-dimensional correlated dirac fermion. *Nature*, 464:847. (Cited on page 53.)

[Mermin, 1968] Mermin, N. D. (1968). Crystalline order in two dimensions. *Phys. Rev.*, 176:250. (Cited on page 9.)

[Mermin and Wagner, 1966] Mermin, N. D. and Wagner, H. (1966). Absence of ferromagnetism or antiferromagnetism in one - or two dimensional isotropic heisenberg model. *Phys. Rev. Lett.*, 17:1133. (Cited on page 9.)

[Mikitik and Sharlai, 2008] Mikitik, G. P. and Sharlai, Y. V. (2008). Electron energy spectrum and the berry phase in a graphite bilayer. *Phys. Rev. B*, 77:113407. (Cited on pages 40 and 45.)

[Milovanović and Predin, 2012] Milovanović, M. V. and Predin, S. (2012). On the coexistence of antiferromagnetism and d + i d superconducting correlations in the graphene bilayer. *Phys. Rev. B*, 86:195113. (Cited on pages 53 and 76.)

[Min et al., 2006] Min, H., Hill, J. E., Sinitsyn, N. A., Sahu, B. R., Kleinman, L., and MacDonald, A. H. (2006). Intrinsic and rashba spin-orbit interactions in graphene sheets. *Phys. Rev. B*, 74:165310. (Cited on page 77.)

[Nandkishore et al., 2011] Nandkishore, R., Levitov, L. S., and Chubukov, A. V. (2011). Chiral superconductivity from repulsive interactions in doped graphene. *Nature Physics*, 8:158. (Cited on pages 53 and 56.)

[Nayak et al., 2008] Nayak, C., Simon, S. H., Stern, A., Freedman, M., and Das Sarma, S. (2008). Non-abelian anyons and topological quantum computation. *Rev. Mod. Phys.*, 80:1083–1159. (Cited on page 77.)

[Nemec and Cuniberti, 2007] Nemec, N. and Cuniberti, G. (2007). Hofstadter butterflies of bilayer graphene. *Phys. Rev. B*, 75:201404. (Cited on page 52.)

[Nienhuis et al., 2009] Nienhuis, B., Campostrini, M., and Calabrese, P. (2009). Entanglement, combinatorics and finite-size effects in spin chains. *Journal of Statistical Mechanics: Theory and Experiment*, 2009(02):P02063. (Cited on page 4.)

[Nilsson et al., 2006] Nilsson, J., Castro Neto, A. H., Peres, N. M. R., and Guinea, F. (2006). Electron-electron interactions and the phase diagram of a graphene bilayer. *Phys. Rev. B*, 73:214418. (Cited on page 40.)

[Novoselov et al., 2004] Novoselov, K. S., Geim, A. K., Morozov, S. V., Jiang, D., Zhang, Y., Dubonos, S. V., Grigorieva, I. V., and Firsov, A. A. (2004). Electric field effect in atomically thin carbon films. *Science*, 306:666. (Cited on page 9.)

[Novoselov et al., 2006] Novoselov, K. S., McCann, E., Morozov, S. V., Fal'ko, V. I., Katsnelson, M. I., Zeitler, U., Jiang, D., Schedin, F., and Geim, A. K. (2006). Unconventional quantum hall effect and berry's phase of 2π in bilayer graphene. *Nature Physics*, 2:177. (Cited on page 19.)

[Pathak et al., 2010] Pathak, S., Shenoy, V. B., and Baskaran, G. (2010). Possible high-temperature superconducting state with a $d + id$ pairing symmetry in doped graphene. *Phys. Rev. B*, 81:085431. (Cited on page 53.)

[Pauling, 1960] Pauling, L. (1960). Nature of the chemical bond. *NY:Cornell University Press*. (Cited on page 59.)

[Peirls, 1934] Peirls, R. E. (1934). Bemerkungen uber umwandlungs temperature. *Helv. Phys. Acta*, 7:81. (Cited on page 9.)

[Peschel, 2003] Peschel, I. (2003). Calculation of reduced density matrices from correlation functions. *Journal of Physics A: Mathematical and General*, 36(14):L205. (Cited on pages 6, 20, 24, 45, and 69.)

[Peschel and Chung, 2011] Peschel, I. and Chung, M.-C. (2011). On the relation between entanglement and subsystem hamiltonians. *EPL (Europhysics Letters)*, 96:50006. (Cited on pages 4 and 19.)

[Platt et al., 2013] Platt, C., Hanke, W., and Thomale, R. (2013). Functional renormalization group for multi-orbital fermi surface instabilities. *Advances in Physics*, 62(4-6):453–562. (Cited on page 54.)

[Poilblanc, 2010] Poilblanc, D. (2010). Entanglement spectra of quantum heisenberg ladders. *Phys. Rev. Lett.*, 105:077202. (Cited on pages 4 and 19.)

[Pollmann and Moore, 2010] Pollmann, F. and Moore, J. E. (2010). Entanglement spectra of critical and near-critical systems in one dimension. *New Journal of Physics*, 12:025006. (Cited on page 4.)

[Pollmann et al., 2010] Pollmann, F., Turner, A. M., Berg, E., and Oshikawa, M. (2010). Entanglement spectrum of a topological phase in one dimension. *Phys. Rev. B*, 81:064439. (Cited on page 4.)

[Predin, 2017] Predin, S. (2017). Entanglement spectrum of heisenberg ladders in a time-dependent magnetic field. *arxiv:1705.08675*. (Cited on pages 4 and 19.)

[Predin and Schliemann, 2016] Predin, S. and Schliemann, J. (2016). Entanglement spectra of superconductivity ground states on the honeycomb lattice. *arxiv:1611.01039*. (Cited on page 53.)

[Predin et al., 2016] Predin, S., Wenk, P., and Schliemann, J. (2016). Trigonal warping in bilayer graphene: Energy versus entanglement spectrum. *Phys. Rev. B*, 93:115106. (Cited on pages 28 and 39.)

[Prodan et al., 2010] Prodan, N., Hughes, T. L., and Bernevig, B. A. (2010). Entanglement spectrum of a disordered topological chern insulator. *Phys. Rev. Lett.*, 105:115501. (Cited on page 3.)

[Raghu et al., 2008] Raghu, S., Qi, X.-L., Honerkamp, C., and Zhang, S.-C. (2008). Topological mott insulators. *Phys. Rev. Lett.*, 100:156401. (Cited on page 53.)

[Regnault, 2015] Regnault, N. (2015). Entanglement spectroscopy and its application to the quantum hall effects. *arxiv:1510.07670*. (Cited on page 4.)

[Regnault and Bernevig, 2011] Regnault, N. and Bernevig, B. A. (2011). Fractional chern insulator. *Phys. Rev. X*, 1:021014. (Cited on page 4.)

[Regnault et al., 2009] Regnault, N., Bernevig, B. A., and Haldane, F. D. M. (2009). Topological entanglement and clustering of jain hierarchy states. *Phys. Rev. Lett.*, 103:016801. (Cited on page 3.)

[Rodriguez et al., 2012] Rodriguez, I. D., Simon, S. H., and Slingerland, J. K. (2012). Evaluation of ranks of real space and particle entanglement spectra for large systems. *Phys. Rev. Lett.*, 108:256806. (Cited on page 3.)

[Rowe et al., 2001] Rowe, M. A., Kielpinski, D., Meyer, V., Sackett, C. A., Itano, W. M., Monroe, C., and Wineland, D. J. (2001). Experimental violation of a bell's inequality with efficient detection. *Nature*, 409:791. (Cited on page 2.)

[Rozhkov et al., 2016] Rozhkov, A., Sboychakov, A., Rakhmanov, A., and Nori, F. (2016). Electronic properties of graphene-based bilayer systems. *Physics Reports*, 648:1. (Cited on pages 5, 19, 20, 39, and 40.)

[Rusin and Zawadzki, 2008] Rusin, T. M. and Zawadzki, W. (2008). Zitterbewegung of electrons in graphene in a magnetic field. *Phys. Rev. B*, 78:125419. (Cited on page 10.)

[Saito et al., 1998] Saito, R., Dresselhaus, M. S., and Dresselhaus, G. (1998). *Physical Properties of Carbon Nanotubes*. Imperial College Press, UK. (Cited on page 13.)

[Sato and Ando, 2017] Sato, M. and Ando, Y. (2017). Topological superconductors: a review. *Reports on Progress in Physics*, 80(7):076501. (Cited on page 77.)

[Sato and Fujimoto, 2016] Sato, M. and Fujimoto, S. (2016). Majorana fermions and topology in superconductors. *Journal of the Physical Society of Japan*, 85:072001. (Cited on page 69.)

[Scheidl et al., 2010] Scheidl, T., Ursin, R., Kofler, J., Ramelow, S., Ma, X.-S., Herbst, T., Ratschbacher, L., Fedrizzi, A., Langford, N. K., Jennewein, T., and Zeilinger, A. (2010). Violation of local realism with freedom of choice. *Proc. Natl. Acad. Sci.*, 107:19708. (Cited on page 2.)

[Schliemann, 2011] Schliemann, J. (2011). Entanglement spectrum and entanglement thermodynamics of quantum hall bilayers at $\nu = 1$. *Phys. Rev. B*, 83:115322. (Cited on pages 3, 4, 5, 19, 28, 29, and 71.)

[Schliemann, 2013] Schliemann, J. (2013). Entanglement spectra and entanglement thermodynamics of hofstadter bilayers. *New Journal of Physics*, 15:053017. (Cited on pages 4, 5, 6, 19, 20, 24, 28, 29, 38, 45, 52, 69, and 71.)

[Schliemann, 2014] Schliemann, J. (2014). Entanglement thermodynamics. *Journal of Statistical Mechanics: Theory and Experiment*, 2014:P09011. (Cited on pages 4, 5, 28, 29, and 71.)

[Schliemann and Läuchli, 2012] Schliemann, J. and Läuchli, A. M. (2012). Entanglement spectra of heisenberg ladders of higher spin. *Journal of Statistical Mechanics: Theory and Experiment*, 2012:P11021. (Cited on pages 4, 19, and 39.)

[Schnyder et al., 2008] Schnyder, A. P., Ryu, S., Furusaki, A., and Ludwig, A. W. W. (2008). Classification of topological insulators and superconductors in three spatial dimensions. *Phys. Rev. B*, 78:195125. (Cited on page 69.)

[Schrödinger, 1935] Schrödinger, E. (1935). Discussion of probability relations between separated systems. *Mathematical Proceedings of the Cambridge Philosophical Society*, 31:555. (Cited on page 1.)

[Sorella and Yunoki, 2012] Sorella, Sandro, a. O. Y. and Yunoki, S. (2012). Absence of a spin liquid phase in the hubbard model on the honeycomb lattice. *Scientific Reports*, 2:992. (Cited on page 53.)

[Sorella and Tosatti, 1992] Sorella, S. and Tosatti, E. (1992). Semi-metal-insulator transition of the hubbard model in the honeycomb lattice. *EPL (Europhysics Letters)*, 19:699. (Cited on page 53.)

[Sterdyniak et al., 2011] Sterdyniak, A., Bernevig, B. A., Regnault, N., and Haldane, F. D. M. (2011). The hierarchical structure in the orbital entanglement spectrum of fractional quantum hall systems. *New Journal of Physics*, 13:105001. (Cited on page 3.)

[Sterdyniak et al., 2012] Sterdyniak, A., Chandran, A., Regnault, N., Bernevig, B. A., and Bonderson, P. (2012). Real-space entanglement spectrum of quantum hall states. *Phys. Rev. B*, 85:125308. (Cited on page 3.)

[Sun et al., 2016] Sun, S.-J., Chung, C.-H., Chang, Y.-Y., Tsai, W.-F., and Zhang, F.-C. (2016). Helical majorana fermions in $d_{x^2-y^2} + id_{xy}$-wave topological superconductivity of doped correlated quantum spin hall insulators. *Nature Scientific Reports*, 6:24102. (Cited on page 77.)

[Tanaka et al., 2012] Tanaka, S., Tamura, R., and Katsura, H. (2012). Entanglement spectra of the quantum hard-square model: Holographic minimal models. *Phys. Rev. A*, 86:032326. (Cited on page 4.)

[Thomale et al., 2010a] Thomale, R., Arovas, D. P., and Bernevig, B. A. (2010a). Nonlocal order in gapless systems: Entanglement spectrum in spin chains. *Phys. Rev. Lett.*, 105:116805. (Cited on page 4.)

[Thomale et al., 2011] Thomale, R., Estienne, B., Regnault, N., and Bernevig, B. A. (2011). Decomposition of fractional quantum hall model states: Product rule symmetries and approximations. *Phys. Rev. B*, 84:045127. (Cited on page 3.)

[Thomale et al., 2010b] Thomale, R., Sterdyniak, A., Regnault, N., and Bernevig, B. A. (2010b). Entanglement gap and a new principle of adiabatic continuity. *Phys. Rev. Lett.*, 104:180502. (Cited on page 3.)

[Turner et al., 2010] Turner, A. M., Zhang, Y., and Vishwanath, A. (2010). Entanglement and inversion symmetry in topological insulators. *Phys. Rev. Lett.*, 82:241102(R). (Cited on page 3.)

[Uchoa and Castro Neto, 2007] Uchoa, B. and Castro Neto, A. H. (2007). Superconducting states of pure and doped graphene. *Phys. Rev. Lett.*, 98:146801. (Cited on page 53.)

[Ulybyshev et al., 2013] Ulybyshev, M. V., Buividovich, P. V., Katsnelson, M. I., and Polikarpov, M. I. (2013). Monte carlo study of the semimetal-insulator phase transition in monolayer graphene with a realistic interelectron interaction potential. *Phys. Rev. Lett.*, 111:056801. (Cited on page 53.)

[Vollhardt, 1984] Vollhardt, D. (1984). Normal ^{3}He: an almost localized fermi liquid. *Rev. Mod. Phys.*, 56:99–120. (Cited on page 63.)

[Vučićević et al., 2012] Vučićević, J., Goerbig, M. O., and Milovanović, M. V. (2012). *d*-wave superconductivity on the honeycomb bilayer. *Phys. Rev. B*, 86:214505. (Cited on page 53.)

[Wallace, 1947] Wallace, P. R. (1947). The band theory of graphite. *Phys. Rev.*, 71:622–634. (Cited on pages 9 and 10.)

[Wang et al., 2012] Wang, W. S., Xiang, Y. Y., Wang, Q.-H., Wang, F., Yang, F., and Lee, D.-H. (2012). Functional renormalization group and variational monte carlo studies of the electronic instabilities in graphene near $\frac{1}{4}$ doping. *Phys. Rev. B*, 85:035414. (Cited on pages 53 and 56.)

[Wang and Li, 2016] Wang, Y.-X. and Li, F. (2016). Edge states and phase diagram for graphene under polarized light. *Physica B: Condensed Matter*, 492:1 – 6. (Cited on page 52.)

[Wehling et al., 2011] Wehling, T. O., Sasioglu, E., Friedrich, C., Lichtenstein, A. I., Katsnelson, M. I., and Blügel, S. (2011). Strength of effective coulomb interactions in graphene and graphite. *Phys. Rev. Lett.*, 106:236805. (Cited on pages 56 and 57.)

[Weihs et al., 1998] Weihs, G., Jennewein, T., Simon, C., Weinfurter, H., and Zeilinger, A. (1998). Violation of bell's inequality under strict einstein locality conditions. *Phys. Rev. Lett.*, 81:5039. (Cited on page 2.)

[Wen, 1990] Wen, X. G. (1990). Topological orders in rigid states. *International Journal of Modern Physics B*, 04(02):239–271. (Cited on page 3.)

[Wen, 1991] Wen, X. G. (1991). Mean-field theory of spin-liquid states with finite energy gap and topological orders. *Phys. Rev. B*, 44:2664–2672. (Cited on page 3.)

[Wu et al., 2013] Wu, W., Scherer, M. M., Honerkamp, C., and Le Hur, K. (2013). Correlated dirac particles and superconductivity on the honeycomb lattice. *Phys. Rev. B*, 87:094521. (Cited on page 64.)

[Xiao et al., 2010] Xiao, D., Chang, M.-C., and Niu, Q. (2010). Berry phase effects on electronic properties. *Rev. Mod. Phys.*, 82:1959–2007. (Cited on page 16.)

[Yao and Qi, 2010] Yao, H. and Qi, X.-L. (2010). Entanglement entropy and entanglement spectrum of the kitaev model. *Phys. Rev. Lett.*, 105:080501. (Cited on page 4.)

[Zhang et al., 2005] Zhang, Y., Tan, Y.-W., Stormer, H. L., and Kim, P. (2005). Experimental observation of the quantum hall effect and berry's phase in graphene. *Nature*, 438:201. (Cited on page 10.)

[Zozulya et al., 2009] Zozulya, O. S., Haque, M., and Regnault, N. (2009). Entanglement signatures of quantum hall phase transitions. *Phys. Rev. B*, 79:045409. (Cited on page 3.)

COLOPHON

This document was typeset using the typographical look-and-feel `classicthesis` developed by André Miede. The style was inspired by Robert Bringhurst's seminal book on typography "*The Elements of Typographic Style*". `classicthesis` is available for both LaTeX and LyX:

`http://code.google.com/p/classicthesis/`

Happy users of `classicthesis` usually send a real postcard to the author, a collection of postcards received so far is featured here:

`http://postcards.miede.de/`

Final Version as of August 25, 2017 (`classicthesis` version 1.0).